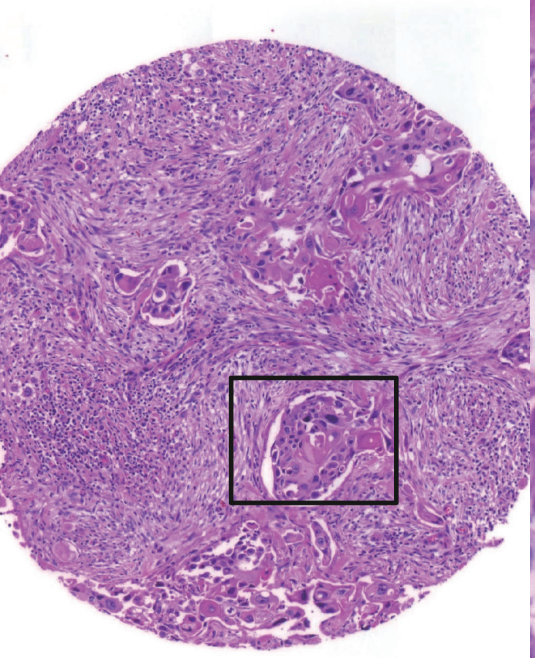
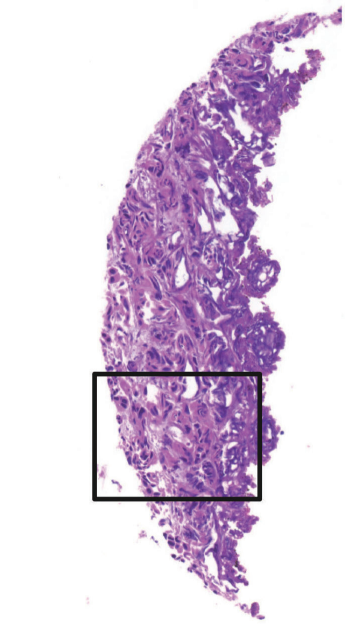
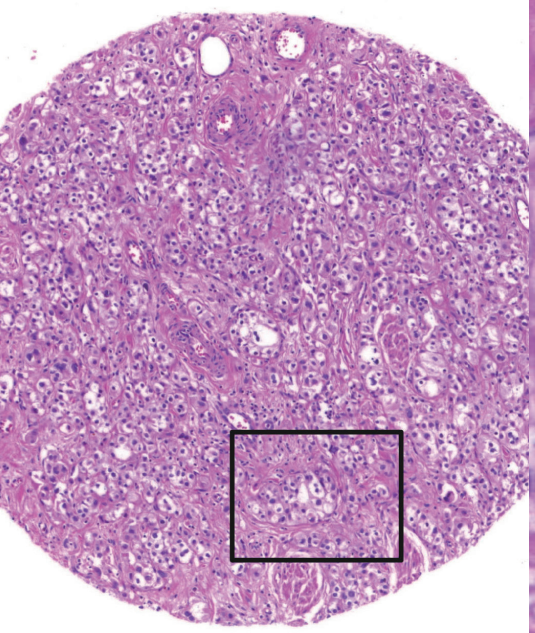
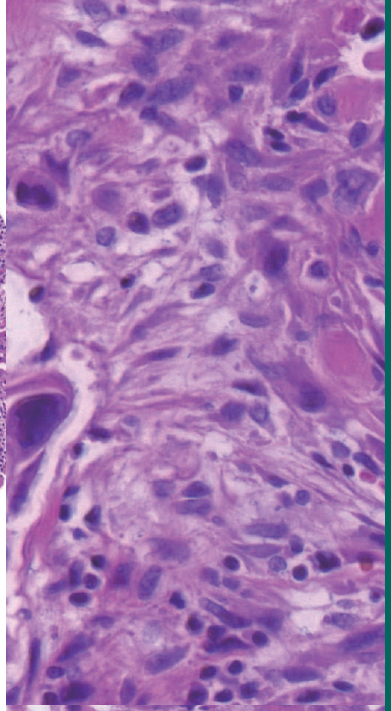
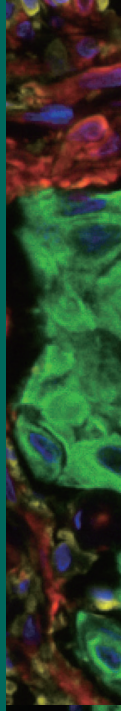
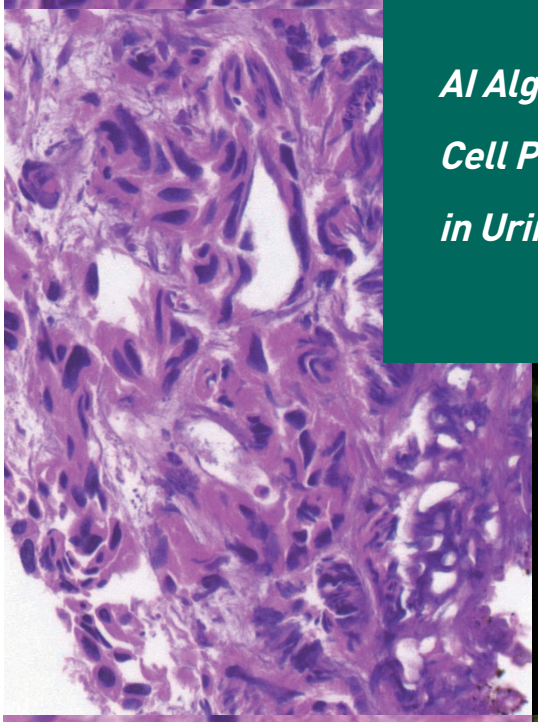
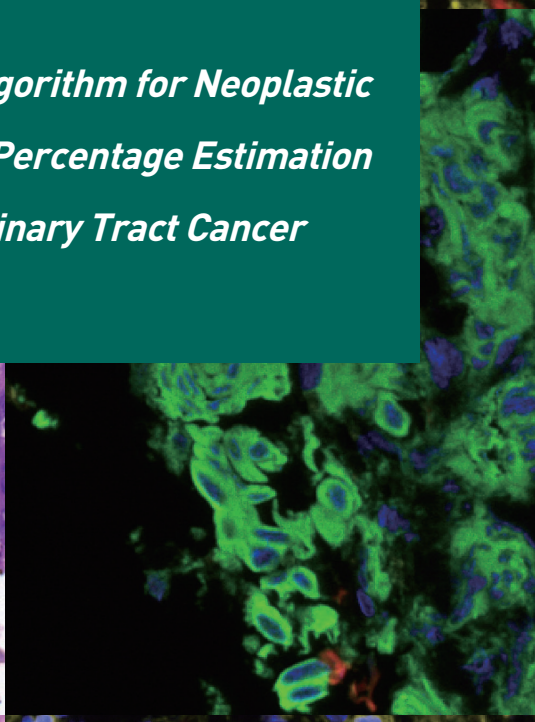
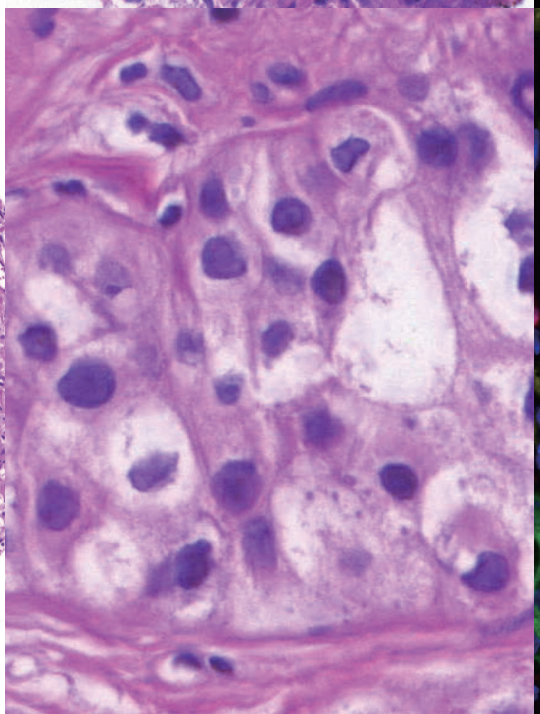
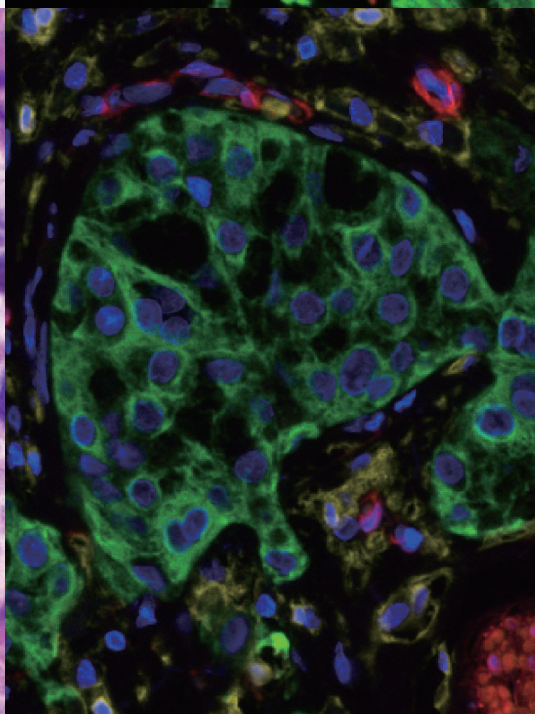

JPTM

Journal of Pathology and Translational Medicine

September 2024
Vol. 58 / No.5
jpatholtm.org
pISSN: 2383-7837
eISSN: 2383-7845

AI Algorithm for Neoplastic Cell Percentage Estimation in Urinary Tract Cancer

Journal of Pathology and Translational Medicine

J Pathol Transl Med
pISSN: 2383-7837
eISSN: 2383-7845

Volume 58, Number 5, September 2024

CONTENTS

ORIGINAL ARTICLES

CASE REPORTS

JPTM
Journal of Pathology and Translational Medicine 2024; 58: 205-213
https://doi.org/10.4132/jptm.2024.06.24

ORIGINAL ARTICLE

Educational exchange in thyroid core needle biopsy diagnosis: enhancing pathological interpretation through guideline integration and peer learning

Agnes Stephanie Harahap[1], Chan Kwon Jung[2,3]

[1]Department of Anatomical Pathology, Faculty of Medicine Universitas Indonesia - Dr. Cipto Mangunkusumo Hospital, Jakarta, Indonesia;
[2]Department of Hospital Pathology, College of Medicine, The Catholic University of Korea, Seoul;
[3]Cancer Research Institute, College of Medicine, The Catholic University of Korea, Seoul, Korea

Background: While fine needle aspiration cytology (FNAC) plays an essential role in the screening of thyroid nodules, core needle biopsy (CNB) acts as an alternative method to address FNAC limitations. However, diagnosing thyroid CNB samples can be challenging due to variations in background and levels of experience. Effective training is indispensable to mitigate this challenge. We aim to evaluate the impact of an educational program on improving the accuracy of CNB diagnostics. **Methods:** The 2-week observational program included a host mentor pathologist with extensive experience and a visiting pathologist. The CNB classification by The Practice Guidelines Committee of the Korean Thyroid Association was used for the report. Two rounds of reviewing the case were carried out, and the level of agreement between the reviewers was analyzed. **Results:** The first-round assessment showed a concordance between two pathologists for 247 thyroid CNB specimens by 84.2%, with a kappa coefficient of 0.74 (indicating substantial agreement). This finding was attributed to the discordance in the use of categories III and V. After peer learning, the two pathologists evaluated 30 new cases, which showed an overall improvement in the level of agreement. The percentage of agreement between pathologists on thyroid CNB diagnosis was 86.7%, as measured by kappa coefficient of 0.80. **Conclusions:** This educational program, consisting of guided mentorship and peer learning, can substantially enhance the diagnostic accuracy of thyroid CNB. It is useful in promoting consistent diagnostic standards and contributes to the ongoing development of global pathology practices.

Key Words: Thyroid neoplasms; Large-core needle biopsy; Practice guideline; Education

Received: May 2, 2024 **Revised:** June 22, 2024 **Accepted:** June 24, 2024
Corresponding Author: Chan Kwon Jung, MD, PhD, Department of Pathology, Seoul St. Mary's Hospital, College of Medicine, The Catholic University of Korea, 222 Banpo-daero, Seocho-gu, Seoul 06591, Korea
Tel: +82-2-2258-1622, Fax: +82-2-2258-1627, E-mail: ckjung@catholic.ac.kr

Thyroid cancer represents the most prevalent endocrine malignancy, exhibiting a consistent increase in incidence over the preceding years [1]. Each subtype of thyroid neoplasia is characterized by distinct biological behavior and necessitates a tailored management approach. The management of thyroid nodules relies on a diagnostic approach encompassing clinical evaluation, radiological imaging, and pathological assessment, which are standardized according to periodically updated clinical recommendations [2]. In the field of pathology, the evaluation of thyroid nodules plays an important role as it can give important information regarding the nature of tumors based on cellular morphology and architecture. The goal is to limit the frequency of unnecessary surgical intervention, minimize complications, and reduce the rates of underdiagnosis [3].

Fine needle aspiration cytology (FNAC) plays a pivotal role in the screening of thyroid nodules and is reported according to the Bethesda System for Reporting Thyroid Cytopathology (TBSRTC) as six diagnostic categories [4]. Nonetheless, there are limitations associated with FNAC results, yielding nondiagnostic and nonconclusive diagnoses for follicular lesions [5]. In recent years, there has been exploration into the potential role of core needle biopsy (CNB) as an alternative and complementary method for evaluating thyroid nodules [6-9]. Ultrasound-guided thyroid CNB is regarded as a safe procedure with minimal com-

pISSN 2383-7837
eISSN 2383-7845

plications and is recognized for providing a more accurate diagnosis in the evaluation of thyroid nodules [8]. The pathology findings derived from thyroid CNB should be interpreted in conjunction with clinical assessment and ultrasound findings [10]. The Practice Guidelines Committee of the Korean Thyroid Association provides a detailed approach encompassing indications, patient preparations, biopsy techniques, possible complications, and pathology reporting protocols. Similar to the well-known TBSRTC, the CNB pathology report consisted of six diagnosis categories: category I (nondiagnostic), category II (benign), category III (indeterminate), category IV (follicular neoplasm), category V (suspicious for malignancy), and category IV (malignant). This category system ensures effective communication between pathologists and clinicians. Each category is further subdivided into meticulous subcategories that provide informative details, particularly for categories III and IV [9].

FNAC is a more commonly used and safer technique compared to CNB, which is less frequently utilized. The reason behind this is that CNB requires more advanced technical skills and carries a higher potential risk of complications, making it a specialized technique used only in certain institutions [11]. As a result, some pathologists are highly experienced in CNB, while others have little to no exposure to this technique. Even though CNB uses a similar six-category diagnostic framework as FNAC [4,11], pathologists with less experience find it challenging to interpret.

Proper training is crucial for pathologists who diagnose CNB. Short-term visits to well-established institutions that specialize in CNB pathology can be an effective training method. During these visits, pathologists review cases intensively to enhance their diagnostic skills in CNB specimens. This approach not only helps bridge the experience gap but also promotes consistency in diagnostic standards across different healthcare settings. The purpose of this study is to evaluate how comprehensive mentorship can enhance diagnostic skills in thyroid CNB and promote standardized practices across diverse settings.

MATERIALS AND METHODS

Participants

Two pathologists with varying backgrounds participated in an educational program. The program included a senior pathologist from The Catholic University of Korea, Seoul St. Mary's Hospital, in Seoul (pathologist 1), and a visiting pathologist from Universitas Indonesia - Dr. Cipto Mangunkusumo Hospital in Jakarta (pathologist 2). Pathologist 1 had extensive expertise in thyroid pathology and cytopathology with 20 years of clinical practice. Pathologist 2 had 6 years of expertise in endocrine pathology from Jakarta, Indonesia. She possesses two years of experience in thyroid CNB diagnosis, handling 10 cases in the first year and 112 cases in the second year.

Digital whole slide image

All CNB glass slides were digitally scanned at a 40× magnification using a Hamamatsu NanoZoomer S360 Digital Slide Scanner (Hamamatsu Photonics, Shizuoka Prefecture, Japan). The scanned images did not contain any meta-information or slide label details that could be used to identify patients. For research purposes, each image file was assigned a new identifier, which ensured patient anonymity and data privacy. Whole slide images were viewed and diagnosed using NDP.view2 Image viewing software (Hamamatsu Photonics).

Pathologist 2 reviewed the deidentified whole slide images of CNB and then examined the histologic slides of the matched tumor in a surgical specimen. To do this, we used the Philips IntelliSite Pathology Solution (Philips, Amsterdam, Netherlands), which is the primary diagnostic tool at the Department of Pathology in Seoul St. Mary's Hospital.

Education program

The educational program was conducted at the Department of Pathology, Seoul St. Mary's Hospital for 2 weeks. During the program, pathologist 2 participated in observation sessions, reviewed diagnostic cases, and engaged in interactive learning sessions under the guidance of pathologist 1. The primary aim of the program was to teach standard diagnostic techniques and guidelines through hands-on case reviews, discussions on guideline-based diagnosis, and feedback sessions.

The program's curriculum began with discussions to achieve a consensus utilizing the established guidelines by The Practice Guidelines Committee of the Korean Thyroid Association [9]. The educational materials for thyroid CNB consisted of 247 cases for education and training in the first round and 30 CNB cases for validation of educational effect in the second round. All cases with diagnostic categories IV and VI had confirmed pathologic diagnoses after surgery. Non-thyroidal lesions were immunohistochemically confirmed on biopsy specimens. Category II CNB cases without a surgically confirmed diagnosis were considered benign thyroid nodules if the size of the nodule remained stable or reduced throughout a 2-year observation period or if repeated FNAC and/or CNB yielded a benign diagnosis.

Pathologist 2 initially provided the diagnosis for all cases us-

 https://doi.org/10.4132/jptm.2024.06.24

ing her own diagnostic experience on the Korean CNB reporting system. The diagnostic results were then compared with those of pathologist 1. Afterward, discussions of the findings were held for each case, giving both pathologists an opportunity to provide feedback on their results, which helped to enrich the final diagnosis. Subsequently, discussions connecting the CNB findings with the gold standard post-operative results were conducted. As part of the educational program, a comprehensive validation was held at the end. This involved a second-round individual review of 30 entirely new cases.

Statistical analysis

A statistical analysis was performed to evaluate the level of agreement between two pathologists before and after an educational program. The agreement was measured as a percentage and also by using Cohen's kappa coefficient. The analysis was conducted by the SPSS software for Windows ver. 23.0 (IBM Corp., Armonk, NY, USA). The agreement percentage indicates the frequency of agreement between the pathologists, whereas Cohen's kappa coefficient takes into account the agreement that may occur by chance, providing a more precise measure of concordance. An increase in agreement percentage before and after the educational program indicates an improvement in the concordance between pathologists, which was achieved through educational exchange.

RESULTS

Characteristics of CNB cases

In the first round of evaluation, a total of 247 cases of thyroid CNB consisted of 30% benign thyroid lesions, 8.1% cases of non-invasive thyroid neoplasm with papillary-like nuclear features (NIFTP), 57.1% cases of thyroid cancers, 3.6% cases of non-thyroid cancers, two parathyroid lesions, and one schwannoma (Table 1). The benign thyroid lesions included follicular adenoma, oncocytic adenoma, and nodular hyperplasia. The cases of thyroid cancer included papillary thyroid carcinoma (PTC), invasive encapsulated follicular variant of PTC (IEFVPTC), follicular thyroid carcinoma, oncocytic thyroid carcinoma, poorly differentiated thyroid carcinoma, anaplastic thyroid carcinoma, medullary thyroid carcinoma (MTC), and lymphoma. Non-thyroid cancers included cases of metastases and other malignancies that did not fall within the specified group. In the second round of evaluation, a total of 30 independent cases were included, comprising 16 benign lesions, 13 cases of thyroid cancer, and one parathyroid lesion.

Table 1. The distribution of thyroid core needle biopsy samples used for review according to the final diagnosis

Diagnosis	First round (n=247)	Second round (n=30)
Benign	74 (30.0)	16 (53.3)
Follicular adenoma	49 (19.8)	2 (6.7)
Oncocytic adenoma	12 (4.9)	2 (6.7)
Nodular hyperplasia	13 (5.3)	12 (40.0)
NIFTP	20 (8.1)	0
Thyroid cancer	141 (57.1)	13 (43.3)
Papillary carcinoma	103 (41.7)	8 (26.6)
IEFVPTC	13 (5.3)	3 (10.0)
Follicular carcinoma	4 (1.6)	0
Oncocytic carcinoma	4 (1.6)	0
Poorly differentiated carcinoma	2 (0.8)	0
Anaplastic carcinoma	3 (1.2)	0
Medullary carcinoma	4 (1.6)	1 (3.3)
Lymphoma	8 (3.2)	1 (3.3)
Non-thyroid cancer	9 (3.6)	0
Metastatic carcinoma	8 (3.2)	0
Adenoid cystic carcinoma	2 (0.8)	0
Parathyroid	2 (0.8)	1 (3.3)
Schwannoma	1 (0.4)	0

Values are presented as number (%).
NIFTP, non-invasive thyroid neoplasm with papillary-like nuclear features; IEFVPTC, invasive encapsulated follicular variant of papillary thyroid carcinoma.

First-round assessment

The first-round assessment showed that two pathologists agreed on their diagnostic categories for 247 thyroid CNB specimens by 84.2% (Table 2). The Cohen's kappa coefficient was 0.74, which indicates a substantial level of agreement. Pathologist 1 did not diagnose categories III and V, while pathologist 2 diagnosed category III in 16 cases (6.5%) and category V in nine cases (3.6%). These were the main causes of discordance (Figs. 1–3). In the analysis of concordance based on the final diagnostic group, the following concordance rates were found: 87.8% for benign lesions, 90% for NIFTP, 81.6% for thyroid cancers, 88.9% for non-thyroid cancer, 50% for parathyroid lesion, and 100% for schwannoma.

Diagnostic accuracy comparison between pathologists

We compared the CNB diagnoses made by two pathologists with the final diagnoses to determine which pathologist was more accurate. The pathologists used their own diagnostic criteria to make the CNB diagnoses. We calculated the percentage of cases in each final diagnosis group that each pathologist diagnosed. Subsequently, we aggregated these percentages to determine each pathologist's overall accuracy. We used the following policy for categorizing the CNB diagnoses: Benign thyroid lesions

Table 2. Agreement rates of thyroid core needle biopsy between two pathologists based on the final diagnosis in the first round

Diagnostic category	Pathologist 1	Pathologist 2	Concordance	
			Rate (%)	Kappa
Total (n=247)			84.2	0.74
Category I	0	1		
Category II	10	14		
Category III	0	16		
Category IV	108	100		
Category V	0	9		
Category VI	126	105		
Parathyroid	2	1		
Schwannoma	1	1		
Benign (n=74)			87.8	0.62
Category II	10	8		
Category III	0	7		
Category IV	64	57		
Category V	0	0		
Category VI	0	2		
NIFTP (n=20)			90.0	[a]
Category III	0	2		
Category IV	20	18		
Thyroid cancer (n=141)			81.6	0.55
Category I	0	1		
Category II	0	5		
Category III	0	7		
Category IV	24	24		
Category V	0	9		
Category VI	117	95		
Non-thyroid cancer (n=9)			88.9	[a]
Category II	0	1		
Category VI	9	8		
Parathyroid (n=2)			50.0	[a]
Parathyroid	2	1		
Category IV	0	1		
Schwannoma (n=1)	1	1	100	[a]

NIFTP, non-invasive thyroid neoplasm with papillary-like nuclear features.
[a]Cohen's kappa cannot be computed because pathologist 1 is constant.

should be classified as category II, while NIFTP cases should be classified as category IV and cancers should be classified as category VI. Based on the classification policy, pathologist 1 correctly diagnosed approximately 63.9% of the relevant cases, while pathologist 2 correctly diagnosed approximately 52.9% of the relevant cases. Therefore, pathologist 1 had a higher accuracy rate in diagnosing the cases according to the given criteria, making him more aligned with the specified diagnostic expectations for benign, NIFTP, and cancer cases.

Second-round assessment

After the interactive learning sessions, a subsequent evaluation of thyroid CNB diagnosis was conducted. The two pathologists unanimously agreed to diagnose IEFVPTC, PTC, MTC, lymphoma, and parathyroid lesions. However, the agreement for nodular hyperplasia, follicular adenoma, and oncocytic adenoma was 83.3%, 50%, and 50%, respectively. During the second-round assessment, pathologist 1 consistently classified 12 cases of nodular hyperplasia as category 2, 2 cases of follicular adenoma as category 4, and two cases of oncocytic adenoma as category 4. Pathologist 2, on the other hand, diagnosed two cases of nodular hyperplasia as category 4, along with a diagnosis of category 2. Additionally, two cases of oncocytic adenoma and follicular adenoma were each diagnosed with category 2 and category 4.

Assessment of peer learning impact on diagnosis

To evaluate the impact of interactive peer learning sessions on thyroid CNB diagnosis, we focused on thyroid and parathyroid lesions, excluding metastatic cancers and other tumors (Fig. 4). During the first round, the concordance rate and Cohen's kappa coefficient between pathologist 1 and pathologist 2 were 84.0% and 0.73, respectively. In the second round, the concordance rate and Cohen's kappa coefficient between the same pathologists were 86.7% and 0.80, respectively (Table 3). This suggests an improvement in the level of agreement between pathologists compared to the first-round evaluation.

DISCUSSION

Pathology diagnosis is influenced by various factors that contribute to a degree of variability among observers. In the field of thyroid pathology, even the most widely accepted screening method, known as FNAC, continues to exhibit variability among different observers [12-14]. Diagnosing thyroid CNB samples can be challenging due to different levels of experience and exposure to the cases. This variability is common, especially when diagnosing indeterminate cases with category III, IV, or V. This is mainly due to the subtle nature of atypia, a limited amount of tumor cells, and uncertainty regarding the tumor capsule's status in CNB [15]. The complexity of these diagnoses highlights the need for continuous education and peer learning.

We demonstrated that consistent exposure and feedback are essential for improving diagnostic skills. In the first-round assessment, our analysis revealed an overall 84.2% concordance and a substantial agreement between the two pathologists. In addition to the propensity of using categories III and V, pathologist 2 also diagnosed fewer cases as category VI. The diagnosis of category III is considered appropriate when a follicular proliferative lesion displays focal nuclear atypia, characterized by nuclear enlarge-

https://doi.org/10.4132/jptm.2024.06.24

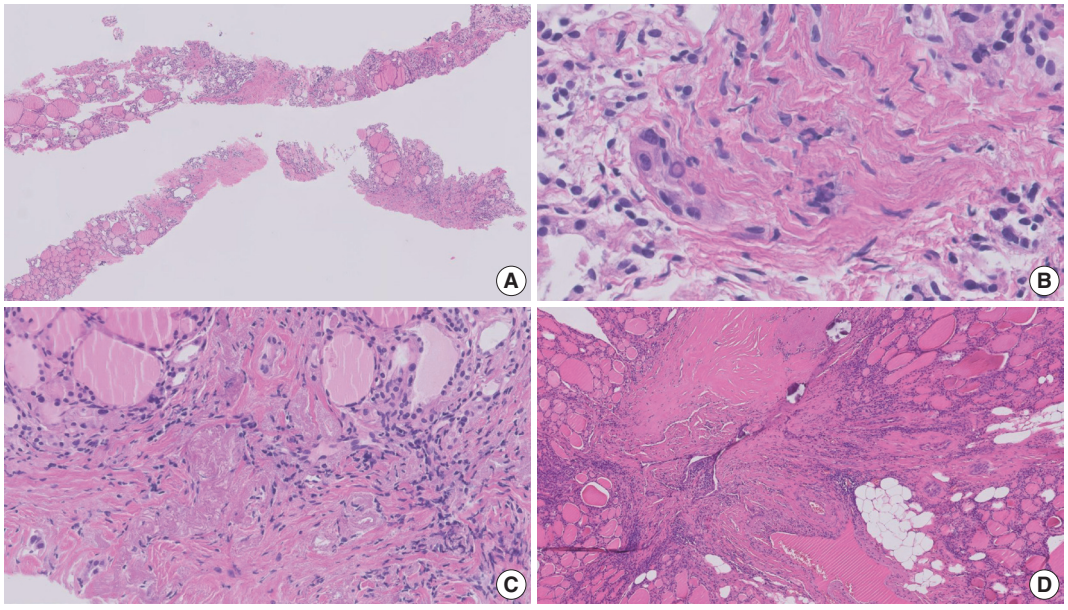

Fig. 1. A case of discrepant diagnosis between two pathologists in a core needle biopsy specimen with papillary thyroid carcinoma. (A) The biopsy specimen presents a fibrotic lesion with few tumor cells. On high-power views (B, C), a few tumor cells with nuclear features of papillary carcinoma were observed. One pathologist interpreted this case as an indeterminate follicular lesion (category III), while the other pathologist diagnosed it as papillary carcinoma (category VI). (D) A matched tumor in a surgical specimen reveals paucicellular papillary carcinoma.

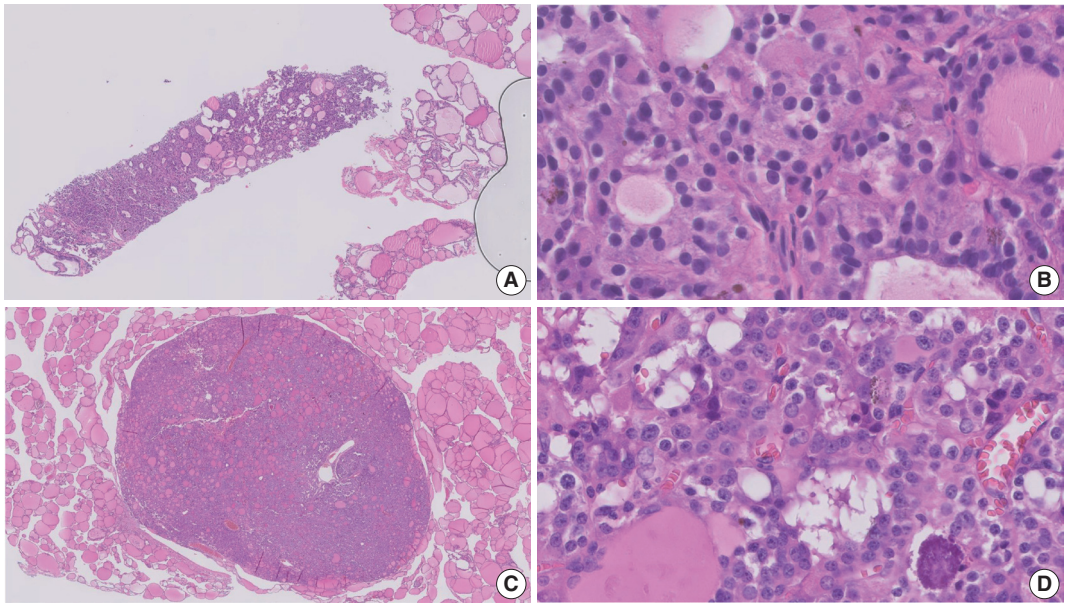

Fig. 2. A case of discrepant diagnosis between two pathologists in a core needle biopsy specimen with medullary thyroid carcinoma. (A) The biopsy specimen shows a tumor area with a mixed follicular and solid growth pattern, which has no fibrotic capsule and is detached from the surrounding normal thyroid tissue. (B) The tumor cells exhibit round to oval hyperchromatic nuclei and ill-defined amphophilic cytoplasm. One pathologist interpreted this case as an indeterminate follicular lesion (category III), while the other pathologist diagnosed it as medullary thyroid carcinoma (category VI). In the matched tumor in a surgical specimen (C, D), a well-defined medullary thyroid carcinoma is observed.

ment with pale chromatin, irregular nuclear membrane, and nuclear grooves amidst a predominantly benign background of follicles [9]. The challenges associated with the diagnosis of category III might be attributable to several factors. The subtlety of nuclear atypia, the presence of oncocytic nuclei, vacuoles, lymphocyte infiltration, and the occurrence of macrofollicles complicated accurate diagnosis. Artifacts introduced during the biopsy procedure, such as tissue distortion or fragmentation, further con-

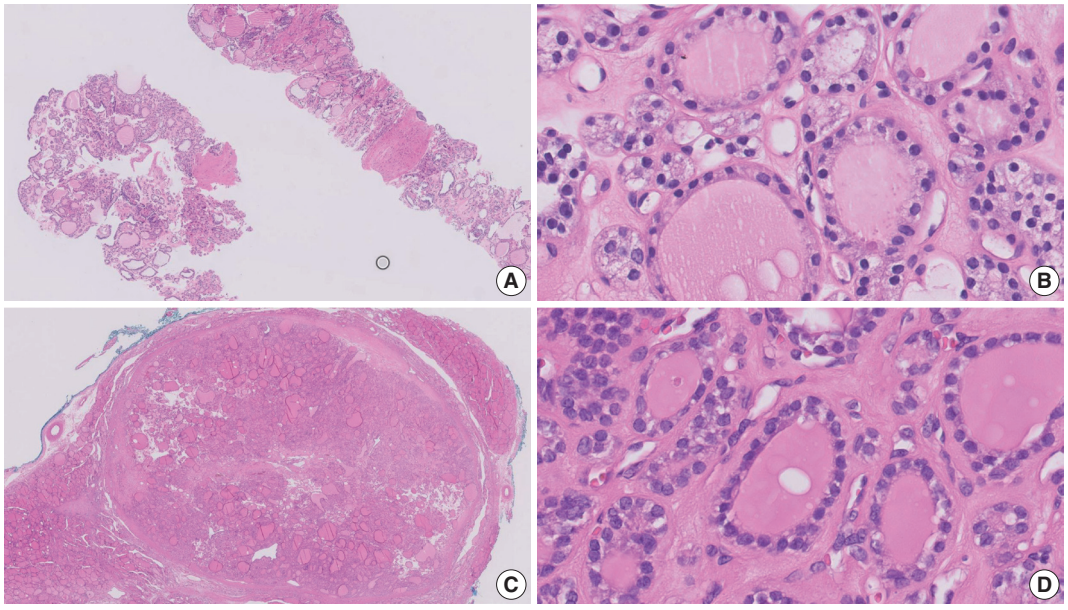

Fig. 3. A core needle biopsy specimen with non-invasive follicular thyroid neoplasm with papillary-like nuclear features (NIFTP) where two pathologists had discrepant diagnoses. (A) The biopsy specimen displays a follicular-patterned lesion that is separated from normal thyroid tissue by a thick fibrotic capsule. On the left side, the detached tumor tissue is visible. The histologic features of the tumor are not vastly different from normal tissue on a low-power view. (B) On a high-power view, subtle nuclear atypia is observed in tumor cells. One pathologist interpreted this case as an indeterminate follicular lesion (category III), while the other pathologist diagnosed it as follicular neoplasm with nuclear atypia (category IV). In the matched tumor in a surgical specimen (C, D), the tumor was diagnosed as NIFTP.

tribute to these diagnostic difficulties.

Over an extended period, histological assessment of the PTC nuclear features has been associated with potential interobserver disagreement, even in cases utilizing surgical specimens [16]. Previous studies have reported changes in nuclear features in CNB specimens [17,18]. Seok et al. [17] reported that the nuclei of PTC in CNB specimens are smaller and less irregular with less chromatin clearing than in thyroidectomy specimens. In a study conducted by Haq et al. [18], the nuclear morphology of CNB was compared to that of surgical specimens using a deep-learning model. The results showed a significant reduction in nuclear size, darker nuclear staining, and frequent nuclear vacuole artifacts in the CNB specimens of PTC. Although the PTC nuclear features were still detectable in microscopic appearance, they were more difficult to notice due to their smaller size and darker chromatin in the CNB specimens.

The microscopic appearance of PTC subtypes, particularly tall cell, follicular, and oncocytic, may vary between CNB and surgical specimens. The tall cell subtype is defined by the presence of more than 30% of tumor cells exhibiting a height at least three times greater than their width [19,20]. The presence of 'shrunken cells' in CNB samples poses a challenge to obtaining accurate measurements. Similarly, in cases where there is a clear-cut oncocytic appearance, the oncocytes may have enlarged nuclei, occasionally with bizarre shapes, and abundant granular eosinophilic cytoplasm. However, certain tumors displayed minimal oncocytic alterations, which posed a challenge in evaluating CNB samples. The absence of the usual prominent nucleoli observed in oncocytes further complicated the assessment. Large-sized follicles, which are more commonly encountered in nodular hyperplasia, require meticulous examination of nuclear atypia to exclude.

Category IV follicular neoplasm is diagnosed when there is an encapsulated follicular-patterned tumor, with or without nuclear atypia. The presence of a fibrous capsule in the CNB specimen plays a crucial role in determining category IV. Therefore, adequate sampling of the tumor, capsule, and adjacent non-neoplastic area is essential. Ideally, the tumor would be classified as category IV based on its microfollicular pattern, presence of atypical follicular cells distinct from adjacent normal follicles, and a portion of the fibrous capsule. In situations where a tumor is not accompanied by the capsule, it can be difficult to determine whether it should be categorized as III or IV [9]. This could be the reason why pathologist 2 used category III. In such cases, ultrasound images can be helpful in ensuring accurate intratumoral sampling and providing a clearer diagnosis.

The diagnosis of thyroid cancer cases can vary greatly depending on the pathologist. Pathologist 2 tends to have the most var-

 https://doi.org/10.4132/jptm.2024.06.24

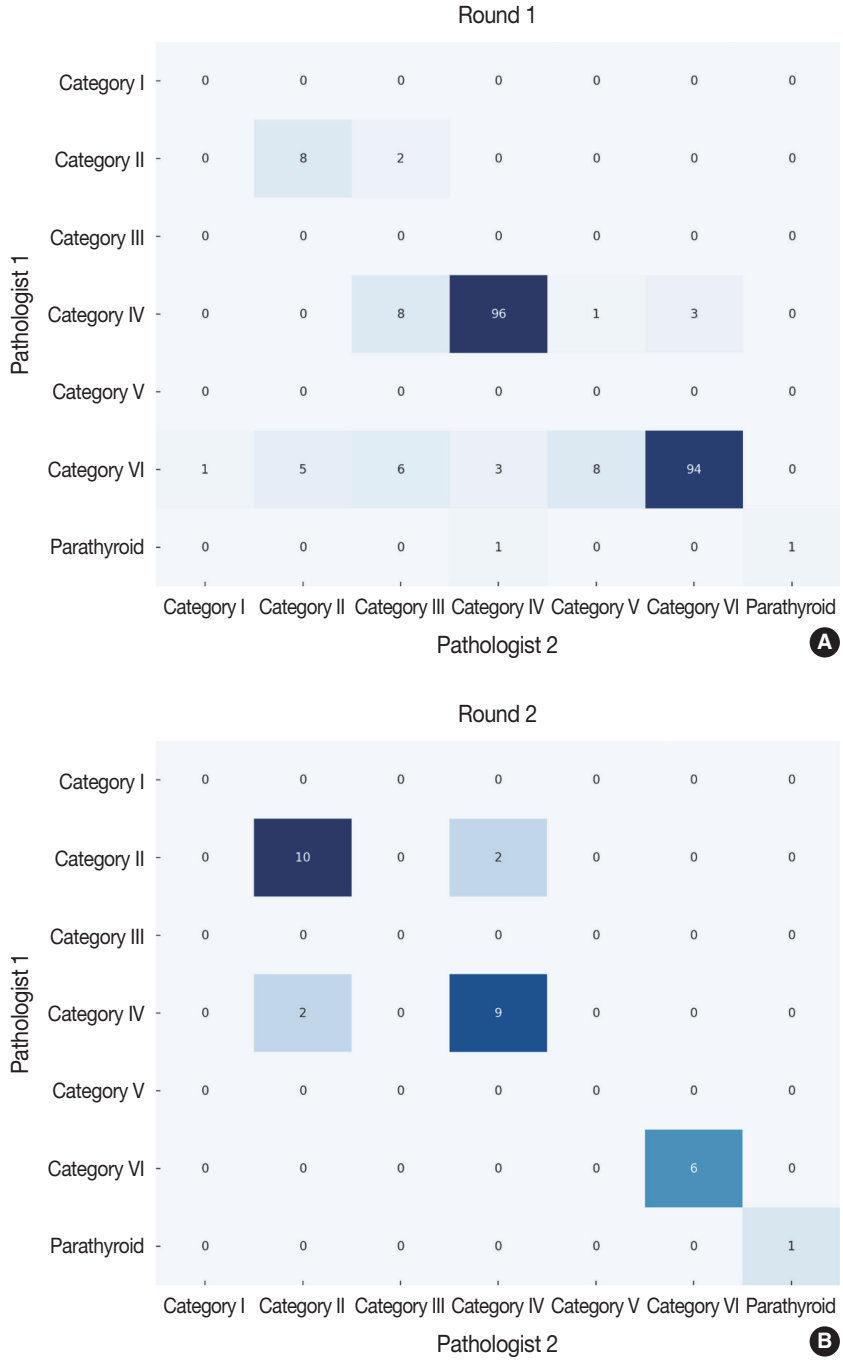

Fig. 4. Comparison of thyroid core needle biopsy diagnoses between two pathologists before and after peer learning in thyroid and parathyroid lesions. (A) In the first round (n=237), the confusion matrix between pathologist 1 and pathologist 2 shows a concordance rate of 84.0% and a Cohen's kappa coefficient of 0.73. (B) In the second round (n=30), the confusion matrix between pathologist 1 and pathologist 2 demonstrates a concordance rate of 86.7% and a Cohen's kappa coefficient of 0.80.

ied categorical diagnoses, while non-thyroidal cancer and parathyroid lesions show the lowest agreement. Pathologist 1, on the other hand, has a more distinct diagnosis for these entities. It is possible that this is due to the small number of tumor cells in the specimens or a lower level of confidence from pathologist 2 during the initial diagnosis.

The peer learning educational program allowed pathologist 2 to engage in discussions about challenging cases and to receive immediate feedback, which contributed to an increase in consistency and concordance in CNB interpretation. The peer learning

Table 3. Comparison of thyroid core needle biopsy diagnosis between two pathologists after peer learning in the second round

Diagnostic category	Pathologist 1	Pathologist 2	Concordance	
			Rate (%)	Kappa
Total (n=30)			87	0.80
Nodular hyperplasia (n=12)			83	
Category II	12	10		
Category IV	0	2		
Follicular adenoma (n=2)			50	
Category II	0	1		
Category IV	2	1		
Oncocytic adenoma (n=2)			50	
Category II	0	1		
Category IV	2	1		
IEFVPTC (n=3)			100	
Category IV	3	3		
Papillary carcinoma (n=8)			100	
Category IV	4	4		
Category VI	4	4		
Medullary carcinoma (n=1)			100	
Category VI	1	1		
Lymphoma (n=1)	1	1	100	
Parathyroid (n=1)	1	1	100	

IEFVPTC, invasive encapsulated follicular variant of papillary thyroid carcinoma.

aspect of the educational program was instrumental in addressing these challenges. By participating in discussions, observing cases, and receiving immediate feedback from pathologist 1, pathologist 2 was able to refine their diagnostic skills. This collaborative approach not only improved the overall concordance rate but also emphasized the value of standardizing diagnostic criteria to minimize ambiguity.

In addition to skill enhancement, our study also highlights the importance of a robust classification system for CNB diagnoses. The Korean Thyroid Association's guidelines provide a solid foundation for effective communication between pathologists and clinicians. After receiving appropriate training, pathologists from different backgrounds can successfully apply this diagnostic system. This framework has been proven effective in achieving accurate and reproducible diagnoses, even for those with varying levels of experience. This standardized approach plays a crucial role in reducing discrepancies and ensuring that patients receive appropriate and consistent care.

The educational program, designed to bridge these gaps, proved to be highly effective. Pathologist 2's interaction with pathologist 1 through discussions, case reviews, and immediate feedback facilitated a significant improvement in diagnostic concordance, reducing the variability in interpretation. The peer learning model adopted in the program provided a platform for addressing challenges and refining diagnostic skills, ultimately leading to better consistency and reliability in CNB interpretation.

A notable outcome from our program was the enhanced consensus achieved between the two pathologists, reflected in the second-round assessment. The increase in Cohen's kappa coefficient from 0.73 to 0.80 demonstrated the success of the peer learning approach in improving diagnostic accuracy. The consensus in diagnosing specific thyroid cancers, such as PTC and MTC, further validated the effectiveness of this collaborative model.

This study suggests that implementing similar educational exchanges and standardized classification systems in other areas of pathology can promote consistent diagnostic standards and reduce diagnostic discrepancies. By encouraging ongoing education, peer feedback, and standardization, the pathology community can improve the quality of diagnosis and patient care. These efforts contribute to the continued development of reliable diagnostic practices in thyroid CNB and beyond.

In conclusion, our educational program demonstrated that consistent exposure to complex cases, guided mentorship, and immediate feedback can substantially enhance the diagnostic skills of pathologists and improve the diagnostic accuracy of thyroid CNB. The variability in diagnostic outcomes, particularly in indeterminate cases, can be significantly reduced through structured educational programs and standardization of diagnostic frameworks. The success of this program in aligning diagnostic interpretations underscores the importance of collaborative learning and standardization. This approach can contribute to reducing diagnostic discrepancies and improving the quality of patient care in thyroid CNB. This model can be replicated in other areas of pathology to promote consistent diagnostic standards and facilitate knowledge exchange among professionals, contributing to the ongoing development of global pathology practices.

Ethics Statement

This study was performed in accordance with the principles of the Declaration of Helsinki and was approved by the Catholic Medical Center, The Catholic University of Korea (XC21ENDI0031K). Informed consent was waived because the study was conducted retrospectively.

Availability of Data and Material

All data analyzed during this study are included in this published article.

Code Availability

Not applicable.

ORCID

Agnes Stephanie Harahap https://orcid.org/0000-0001-8920-7873
Chan Kwon Jung https://orcid.org/0000-0001-6843-3708

https://doi.org/10.4132/jptm.2024.06.24

Author Contributions

Conceptualization: CKJ. Data curation: CKJ. Formal analysis: CKJ, ASH. Funding acquisition: CKJ. Investigation: CKJ. Methodology: ASH, CKJ. Project administration: CKJ. Resources: CKJ. Supervision: CKJ. Validation: ASH, CKJ. Visualization: CKJ. Writing—original draft: ASH, CKJ. Writing—review & editing: ASH, CKJ. Approval of final manuscript: ASH, CKJ.

Conflicts of Interest

C.K.J., the editor-in-chief of the *Journal of Pathology and Translational Medicine*, was not involved in the editorial evaluation or decision to publish this article. The remaining author has declared no conflicts of interest.

Funding Statement

This research was supported by a grant from the Korea Health Technology R&D Project through the Korea Health Industry Development Institute (KHIDI), funded by the Ministry of Health & Welfare, Republic of Korea (grant number: RS-2021-KH113146).

References

1. Kitahara CM, Schneider AB. Epidemiology of thyroid cancer. Cancer Epidemiol Biomarkers Prev 2022; 31: 1284-97.
2. Lee EK, Park YJ, Jung CK, Na DG. A narrative review of the 2023 Korean Thyroid Association management guideline for patients with thyroid nodules. Endocrinol Metab (Seoul) 2024; 39: 61-72.
3. Haugen BR, Alexander EK, Bible KC, et al. 2015 American Thyroid Association management guidelines for adult patients with thyroid nodules and differentiated thyroid cancer: the American Thyroid Association Guidelines Task Force on Thyroid Nodules and Differentiated Thyroid Cancer. Thyroid 2016; 26: 1-133.
4. Ali SZ, Baloch ZW, Cochand-Priollet B, Schmitt FC, Vielh P, VanderLaan PA. The 2023 Bethesda System for Reporting Thyroid Cytopathology. Thyroid 2023; 33: 1039-44.
5. Doubi A, Alrayes NS, Alqubaisi AK, Al-Dhahri SF. The value of repeating fine-needle aspiration for thyroid nodules. Ann Saudi Med 2021; 41: 36-42.
6. Suh CH, Baek JH, Choi YJ, et al. Efficacy and safety of core-needle biopsy in initially detected thyroid nodules via propensity score analysis. Sci Rep 2017; 7: 8242.
7. Kim HC, Kim YJ, Han HY, et al. First-line use of core needle biopsy for high-yield preliminary diagnosis of thyroid nodules. AJNR Am J Neuroradiol 2017; 38: 357-63.
8. Paja M, Del Cura JL, Zabala R, Korta I, Ugalde A, Lopez JI. Core-needle biopsy in thyroid nodules: performance, accuracy, and complications. Eur Radiol 2019; 29: 4889-96.
9. Jung CK, Baek JH, Na DG, Oh YL, Yi KH, Kang HC. 2019 Practice guidelines for thyroid core needle biopsy: a report of the Clinical Practice Guidelines Development Committee of the Korean Thyroid Association. J Pathol Transl Med 2020; 54: 64-86.
10. Hahn SY, Shin JH, Oh YL, Park KW. Ultrasound-guided core needle biopsy techniques for intermediate or low suspicion thyroid nodules: which method is effective for diagnosis? Korean J Radiol 2019; 20: 1454-61.
11. Suh CH, Baek JH, Lee JH, et al. The role of core-needle biopsy in the diagnosis of thyroid malignancy in 4580 patients with 4746 thyroid nodules: a systematic review and meta-analysis. Endocrine 2016; 54: 315-28.
12. Padmanabhan V, Marshall CB, Akdas Barkan G, et al. Reproducibility of atypia of undetermined significance/follicular lesion of undetermined significance category using the bethesda system for reporting thyroid cytology when reviewing slides from different institutions: a study of interobserver variability among cytopathologists. Diagn Cytopathol 2017; 45: 399-405.
13. Clary KM, Condel JL, Liu Y, Johnson DR, Grzybicki DM, Raab SS. Interobserver variability in the fine needle aspiration biopsy diagnosis of follicular lesions of the thyroid gland. Acta Cytol 2005; 49: 378-82.
14. Sripodok S, Benjakul N. Interobserver variability in inconclusive diagnostic categories of thyroid fine needle aspiration cytology: an urban-based tertiary hospital experience. Ann Diagn Pathol 2023; 63: 152083.
15. Jung CK. Reevaluating diagnostic categories and associated malignancy risks in thyroid core needle biopsy. J Pathol Transl Med 2023; 57: 208-16.
16. Elsheikh TM, Asa SL, Chan JK, et al. Interobserver and intraobserver variation among experts in the diagnosis of thyroid follicular lesions with borderline nuclear features of papillary carcinoma. Am J Clin Pathol 2008; 130: 736-44.
17. Seok JY, An J, Cho HY, Kim Y, Ha SY. Nuclear features of papillary thyroid carcinoma: comparison of core needle biopsy and thyroidectomy specimens. Ann Diagn Pathol 2018; 32: 35-40.
18. Haq F, Bychkov A, Jung CK. A matched-pair analysis of nuclear morphologic features between core needle biopsy and surgical specimen in thyroid tumors using a deep learning model. Endocr Pathol 2022; 33: 472-83.
19. Baloch ZW, Asa SL, Barletta JA, et al. Overview of the 2022 WHO classification of thyroid neoplasms. Endocr Pathol 2022; 33: 27-63.
20. Jung CK, Bychkov A, Kakudo K. Update from the 2022 World Health Organization classification of thyroid tumors: a standardized diagnostic approach. Endocrinol Metab (Seoul) 2022; 37: 703-18.

JPTM
Journal of Pathology and Translational Medicine 2024; 58: 214-218
https://doi.org/10.4132/jptm.2024.07.03

ORIGINAL ARTICLE

Single umbilical artery and associated birth defects in perinatal autopsies: prenatal diagnosis and management

Manushree Saxena, Bhagyashri Hungund

Department of Pathology, KAHER'S Jawaharlal Nehru Medical College, Belagavi, India

Background: The umbilical cord forms the connection between the fetus and the placenta at the feto-maternal interface and normally comprises two umbilical arteries and one umbilical vein. In some cases, only a single umbilical artery (SUA) is present. This study was conducted to evaluate associations between SUA and other congenital malformations discovered in perinatal autopsies and to ascertain the existence of preferential associations between SUA and certain anomalies. **Methods:** We evaluated records of all fetuses sent for autopsy to the Department of Pathology during the 10-year period from 2013 through 2022 (n=1,277). The data were obtained from the hospital's pathology laboratory records. The congenital anomalies were grouped by organ or system for analysis and included cardiovascular, urinary tract, nervous system, gastrointestinal tract, musculoskeletal, and lung anomalies. **Results:** A SUA was present in 8.61% of the autopsies. The gestational age of the affected fetuses ranged between 13 to 40 weeks. An SUA presented as an isolated single anomaly in 44 cases (3.4%). Of the 110 SUA cases, 60% had other congenital anomalies. There was a significant association between birth defects and SUAs ($p<.001$). Strong associations between SUA and urinary tract, lung, and musculoskeletal anomalies were observed. **Conclusions:** A SUA is usually seen in association with other congenital malformations rather than as an isolated defect. Therefore, examination for associated anomalies when an SUA is detected either antenatally or postnatally is imperative. The findings of this study should be helpful in counseling expectant mothers and their families in cases of SUA.

Key Words: Single umbilical artery; Congenital abnormalities; Antenatal diagnosis; Perinatal care

Received: December 10, 2023 **Revised:** April 5, 2024 **Accepted:** June 12, 2024
Corresponding Author: Bhagyashri Hungund, MD, Department of Pathology, KAHER'S Jawaharlal Nehru Medical College, Nehru Nagar, Belagavi 590010, Karnataka, India
Tel: +91-9964318708, Fax: +91-0831-2470759, E-mail: Bhagya78h@gmail.com, Manushree.s444@gmail.com

The umbilical cord forms a stable connection between the fetus and the placenta at the feto-maternal interface [1]. The cord develops between the third and seventh week following conception and usually comprises two umbilical arteries and one umbilical vein [2]. However, the presence of only a single umbilical artery (SUA) is the most common umbilical cord abnormality and occurs in 0.2%–1.2% of live newborns [3].

The definitive diagnosis can be made histologically by the visualization of only two umbilical cord vessels. Prenatal diagnosis of SUA can be made using antenatal visualization of the umbilical cord using ultrasonography, especially with color Doppler flow imaging [1]. SUA incidence varies between studies and tends to be higher in aborted fetus and autopsy studies [4,5].

Although its pathogenesis is not clearly understood, three theories have been put forth to explain the occurrence of SUA. One theory attributes SUA occurrence to primary agenesis of one artery, a second theory proposes atrophy or secondary atresia of a formerly normal umbilical artery as the cause, and the third theory implicates a persistent allantoic artery in the pathogenesis of SUA. From an embryological perspective, the second theory is the most plausible explanation [5].

An SUA is more frequently encountered in conjunction with a wide variety of other anomalies instead of as an isolated SUA (iSUA) [6]. Although other malformations are present in 10%–27% of cases of SUA, documented findings lack consistency [4,7,8]. The reported incidences of SUA with and without associated comorbidities in live births, either at term or pre-term, vary substantially among studies [4,9-12]. The ability to predict poor perinatal outcome and presence of other congenital malformations is often questioned [13].

Therefore, this study aimed to evaluate the association between SUA and other congenital malformations at the time of perinatal

pISSN 2383-7837
eISSN 2383-7845

autopsy and to ascertain the existence of any preferential associations between SUA and specific anomalies.

MATERIALS AND METHODS

Study design

This was a retrospective study performed at Jawaharlal Nehru Medical College and Research Centre, Belagavi, India. We evaluated records of all fetuses sent for autopsy to the Department of Pathology during the 10-year period from 2013 through 2022 (n = 1,277). The data were obtained from the hospital pathology laboratory records. The cases were either intrauterine deaths or abortions due to the detection of congenital anomalies. The presence of SUA was confirmed by histopathological examination of the umbilical cord (Fig. 1).

Information on gestational age at delivery, twinning, sex, and the presence of significant congenital anomalies was reviewed. The congenital anomalies were grouped by organ or system for analysis and included cardiovascular, urinary tract, nervous system, gastrointestinal tract (GIT), musculoskeletal, and lung anomalies.

Statistical analysis

The odds ratio (OR) and chi-square test were used for data analysis using SPSS ver. 23.0 (IBM Corp., Armonk, NY, USA). The OR and its 95% confidence interval (95% CI) were used to express the risk for incidence of a specific congenital abnormality related to SUA. The significance level was set at $p < .05$.

RESULTS

A SUA was found in 8.6% (110/1,277) of the autopsies. The gestational age of the fetuses ranged between 13 to 40 weeks. Three cases of SUA were twins; and, in each of these cases, the co-twin had three vessels. An iSUA was present in 44 cases (3.4%). Of the 110 cases with SUA, 60.0% (n = 66) had other congenital anomalies. There was a significant association between birth defects and SUA cases ($p < .001$) (Table 1).

The incidence of SUA was 4.5 times higher in malformed fetuses (21.4%, 66/308) than in fetuses without abnormalities (4.5%, 44/969).

A strong association with SUA was seen for urinary tract, lung, GIT, and musculoskeletal anomalies. The most associated anomaly was urinary tract defect; this was 4.7 times more likely to occur in SUA cases (OR, 4.7; 95% CI, 2.61 to 8.32; $p < .001$) (Table 2).

Anomalies of the cardiovascular system (CVS) and central nervous system (CNS) did not show significant associations with SUA ($p > .05$).

The congenital anomalies observed in the SUA group included 14 cases of anal atresia (12.7%), 12 cases of unilateral renal agenesis (10.9%), 11 cases of vertebral defects (10.0%), and 10 cases of anencephaly (9.0%). Other anomalies found along with SUA were eight cases of pulmonary hypoplasia (7.2%), six cases of diaphragmatic hernia (5.4%), six cases of sirenomelia sequence (5.4%), and six cases of multi-cystic dysplastic kidney (5.4%).

The urinary tract defects found in the SUA cases in this study were unilateral renal agenesis (n = 12), multi-cystic dysplastic kidney (n = 6), hydronephrosis (n = 5), horseshoe kidney (n = 5), bilateral renal agenesis (n = 4), urinary bladder agenesis (n = 3) and congenital megacystitis (n = 2). The lung defects included pulmonary hypoplasia (n = 8) and congenital cystic adenomatoid malformation (n = 1). The gastrointestinal defects included anal atresia (n = 14), diaphragmatic hernia (n = 6), omphalocele (n = 3), gastroschisis (n = 2), and esophageal atresia (n = 1). The musculoskeletal defects found were vertebral defects (n = 11), si-

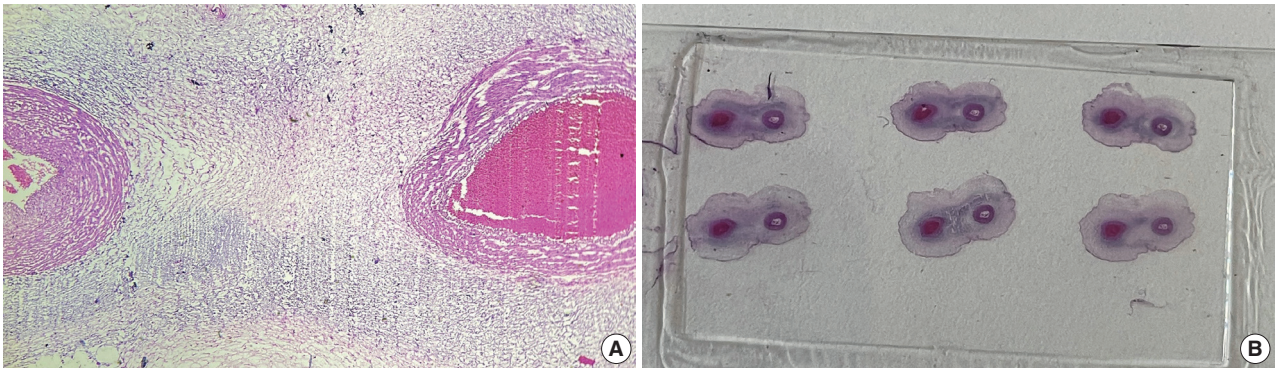

Fig. 1. Cross-section of an umbilical cord. (A) Microscopic image showing a single umbilical artery and one umbilical vein (hematoxylin and eosin). (B) Two vessels seen in the umbilical cord on the slide.

Table 1. Congenital anomalies in the SUA and normal umbilical cord groups

	With SUA (n=110)	Without SUA (n=1,167)	Chi-square	p-value
Total autopsy with birth defects (n=308)	66 (60.0)	242 (20.7)	84.674	<.001
Total autopsy without birth defects (n=969)	44 (40.0)	925 (79.2)		

Values are presented as number (%) unless otherwise indicated.
SUA, single umbilical artery.
p<.05 was considered statistically significant.

Table 2. Risks of congenital anomalies associated with SUA

Birth defect system	With SUA (n=66)	Without SUA (n=242)	OR (95% CI)	p-value
CNS	23 (34.8)	109 (45.0)	0.653 (0.371–1.150)	.140
Urinary tract	39 (59)	57 (23.5)	4.688 (2.642–8.319)	<.001
Lungs	9 (13.6)	13 (5.37)	2.781 (1.133–6.828)	.026
CVS	14 (21.2)	31 (12.8)	1.833 (0.909–3.691)	.090
Gastrointestinal	16 (24.2)	25 (10.3)	2.778 (1.381–5.587)	.004
Musculoskeletal	27 (40.9)	61 (25.2)	2.054 (1.162–3.633)	.013

Values are presented as number (%) unless otherwise indicated.
SUA, single umbilical artery; OR, odds ratio; 95% CI, 95% confidence interval; CNS, central nervous system; CVS, cardiovascular system.
p<.05 was considered statistically significant.

Table 3. External genitalia status of fetuses in all autopsies

	SUA group (n=66)	DUA group (n=242)	Chi-square	p-value
Female	23 (34.8)	101 (41.7)	10.343	.005
Male	36 (54.6)	136 (56.2)		
Ambiguous	7 (10.6)	5 (2.1)		

Values are presented as number (%) unless otherwise indicated.
SUA, single umbilical artery; DUA, double umbilical artery.
p<.05 was considered statistically significant.

renomelia (n = 7), talipes equinovarus (n = 4), cleft lip and/or palate (n = 4), and phocomelia (n = 1). CNS defects included anencephaly (n = 10), meningomyelocele (n = 5), congenital hydrocephalus (n = 3), spina bifida (n = 3), and encephalocele (n = 2). CVS defects included ventricular septal defect (n = 4), dextrocardia (n = 4), tetralogy of Fallot (n = 3), tricuspid atresia (n = 1), coarctation of the aorta (n = 1), and atrial septal defect (n = 1).

The results of our study showed 9.1% (10/110) of SUA cases had a VACTERL (vertebral anomalies-anal atresia-cardiac defects-tracheoesophageal fistula and/or esophageal atresia-renal anomalies-limb defects) association.

Of the 110 cases of SUA, 58 were male, 42 were female and 10 had ambiguous genitalia. Ambiguous genitalia were seen in 10.6% of SUA cases as compared to 2.1% of double umbilical artery cases (Table 3).

DISCUSSION

Estimates regarding malformations associated with SUA exhibit a marked degree of variation in different studies. This might be the result of different sampling sources and sample sizes or other methodological variations.

Information on SUA and its association with congenital abnormalities has primarily originated from two sources: (1) abortions, fetal deaths, and terminations of fetuses with anomalies and (2) live births [4].

Besides a less frequent association of congenital abnormalities with SUA, the incidence of SUA is lower in live births. Live births often show a reduced incidence and frequency of associated abnormalities because most of the affected fetuses have been aborted or terminated during pregnancy. This difference is highlighted by a meta-analysis of these data in which the incidence of SUA in the autopsy data sets approximates at 0.34%–7% and the associated anomalies at 0.25%–81.8% (generally 20%–25%) [14-18]. Additionally, there are temporal disparities between the studies that led to variations in the methods of detection and diagnosis.

Our study found an incidence of SUA at perinatal autopsy of 8.61%, which is comparable to the Nayak et al. study's [19] reported incidence of 7.9%.

Congenital anomaly was observed in 60% of the SUA group, significantly higher than in the "non SUA" group. This was consistent with the findings of Froehlich and Fujikura in which 53% of SUA cases involved other malformations [20]. Lilja [8] reported a 4.3-times higher risk of associated abnormalities in SUA cases; our study revealed a threefold increase in the risk.

In our study, urinary tract anomalies of varying severity were present in 35% of the SUA cases and indicated a strong association between urinary tract anomalies and SUA. This was consistent with most of the results reported by others [21-23]. This highlights the magnitude of urinary tract anomaly occurrence in these fetuses, but the pathogenesis and etiology of the association remain unclear.

In our study, the congenital anomalies associated with SUA included anal atresia, unilateral renal agenesis, vertebral defects, and anencephaly in decreasing frequency. These findings were consistent with those of another study in which renal agenesis,

https://doi.org/10.4132/jptm.2024.07.03

imperforate anus, and vertebral defects were the most specific defects associated with SUA [24]. A population study from Norway also reported a strong association between SUA and gastrointestinal atresia [25].

A study in mice showed that Hedgehog genes play a key role in the development of the feto-placental interface (arteries) and the visceral endoderm/hindgut [26]. This supplies a plausible explanation for the spectrum of malformations in the GIT associated with SUA in our study.

Anomalies of the CVS and CNS did not show a significant association with SUA in our study. This finding agreed with an analysis of autopsied fetuses with SUA that showed lesions of the CNS and CVS are least frequent in SUA cases [22].

Ambiguous genitalia were seen in 10.6% of SUA cases as compared to 2.1% of non-SUA cases in our study. This high occurrence in SUA cases could be due to the autopsy-based nature of this study; cases of ambiguous genitalia with other defects or chromosomal abnormalities may have been more likely to be detected prenatally and sent for autopsy. Therefore, the association cannot be directly attributed to SUA and should be tested in future studies.

Our findings suggest that SUA detection should be accomplished as early as possible because of its association with other congenital malformations.

One strength of the study was the large sample size. This is attributable to the referral nature of the hospital. Also, the detection of SUA in this study was highly sensitive and specific. This was achieved through histopathological examination of the umbilical cord in autopsied specimens.

The typical drawbacks of retrospective research apply to this study as well. Since healthy and surviving infants were not part of the study sample, an extrapolation of the findings to the general population mandates population-based studies.

We found an SUA in 8.61% of the perinatal autopsies. The overall prevalence of congenital anomalies in association with SUA was 60%, significantly greater than iSUA cases. Therefore, careful examination for other anomalies in SUA cases is imperative; detailed ultrasonography, echocardiography, and amniocentesis need to be used when an SUA is discovered during routine ultrasound. The findings of this study should be helpful for counseling expectant mothers and their families in cases of an SUA. We conclude that the identification of an SUA necessitates a thorough examination of the fetus for any other anomalies. Karyotyping for the detection of associated chromosomal abnormalities is a topic for future study.

Ethics Statement

All procedures performed in the current study were approved by the Institutional Ethics Committee (ref no. MCD/DOME/171 dated 19/04/2023). Formal written informed consent was not required; a waiver was obtained from the Institutional Ethics Committee because this was an autopsy-based study.

Availability of Data and Material

The datasets generated or analyzed during the study are available from the corresponding author on reasonable request.

Code Availability

Not applicable.

ORCID

Manushree Saxena https://orcid.org/0009-0002-0115-6325
Bhagyashri Hungund https://orcid.org/0000-0001-9173-4728

Author Contributions

Conceptualization: MS, BH. Data curation: MS. Formal analysis: MS. Investigation: MS. Methodology: MS, BH. Project administration: BH, MS. Resources: MS. Software: MS. Supervision: BH. Validation: BH, MS. Visualization: MS. Writing—original draft: MS. Writing—review & editing: MS, BH. Approval of final manuscript: all authors.

Conflicts of Interest

The authors declare that they have no potential conflicts of interest.

Funding Statement

No funding to declare.

Acknowledgments

The authors wish to thank Dr. Madhuker Saxena for exhaustively reviewing the manuscript and for useful constructive inputs.

References

1. Vrabie SC, Novac L, Manolea MM, Dijmarescu LA, Novac M, Siminel MA. Abnormalities of the umbilical cord. In: Tudorache S, ed. Congenital anomalies: from the embryo to the neonate. London: IntechOpen, 2017; 345-62.
2. Heil JR, Bordoni B. Embryology, umbilical cord [Internet]. Treasure Island: StatPearls Publishing, 2023 [cited 2024 Apr 4]. Available from: https://pubmed.ncbi.nlm.nih.gov/32491422/.
3. Csecsei K, Kovacs T, Hinchliffe SA, Papp Z. Incidence and associations of single umbilical artery in prenatally diagnosed malformed, midtrimester fetuses: a review of 62 cases. Am J Med Genet 1992; 43: 524-30.
4. Thummala MR, Raju TN, Langenberg P. Isolated single umbilical artery anomaly and the risk for congenital malformations: a meta-analysis. J Pediatr Surg 1998; 33: 580-5.
5. Persutte WH, Hobbins J. Single umbilical artery: a clinical enigma in modern prenatal diagnosis. Ultrasound Obstet Gynecol 1995; 6: 216-29.
6. Tulek F, Kahraman A, Taskin S, Ozkavukcu E, Soylemez F. Determination of risk factors and perinatal outcomes of singleton pregnancies complicated by isolated single umbilical artery in Turkish population. J Turk Ger Gynecol Assoc 2015; 16: 21-4.
7. Murphy-Kaulbeck L, Dodds L, Joseph KS, Van den Hof M. Single

umbilical artery risk factors and pregnancy outcomes. Obstet Gynecol 2010; 116: 843-50.
8. Lilja M. Infants with single umbilical artery studied in a national registry. 3: a case control study of risk factors. Paediatr Perinat Epidemiol 1994; 8: 325-33.
9. Tasha I, Brook R, Frasure H, Lazebnik N. Prenatal detection of cardiac anomalies in fetuses with single umbilical artery: diagnostic accuracy comparison of maternal-fetal-medicine and pediatric cardiologist. J Pregnancy 2014; 2014: 265421.
10. Burshtein S, Levy A, Holcberg G, Zlotnik A, Sheiner E. Is single umbilical artery an independent risk factor for perinatal mortality? Arch Gynecol Obstet 2011; 283: 191-4.
11. Bombrys AE, Neiger R, Hawkins S, et al. Pregnancy outcome in isolated single umbilical artery. Am J Perinatol 2008; 25: 239-42.
12. Dagklis T, Defigueiredo D, Staboulidou I, Casagrandi D, Nicolaides KH. Isolated single umbilical artery and fetal karyotype. Ultrasound Obstet Gynecol 2010; 36: 291-5.
13. Rittler M, Mazzitelli N, Fuksman R, de Rosa LG, Grandi C. Single umbilical artery and associated malformations in over 5500 autopsies: relevance for perinatal management. Pediatr Dev Pathol 2010; 13: 465-70.
14. Chow JS, Benson CB, Doubilet PM. Frequency and nature of structural anomalies in fetuses with single umbilical arteries. J Ultrasound Med 1998; 17: 765-8.
15. Abuhamad AZ, Shaffer W, Mari G, Copel JA, Hobbins JC, Evans AT. Single umbilical artery: does it matter which artery is missing? Am J Obstet Gynecol 1995; 173: 728-32.
16. Leung AK, Robson WL. Single umbilical artery: a report of 159 cases. Am J Dis Child 1989; 143: 108-11.
17. Tortora M, Chervenak FA, Mayden K, Hobbins JC. Antenatal sonographic diagnosis of single umbilical artery. Obstet Gynecol 1984; 63: 693-6.
18. Gossett DR, Lantz ME, Chisholm CA. Antenatal diagnosis of single umbilical artery: is fetal echocardiography warranted? Obstet Gynecol 2002; 100: 903-8.
19. Nayak SS, Shukla A, Girisha KM. Anomalies associated with single umbilical artery at perinatal autopsy. Indian Pediatr 2015; 52: 73-4.
20. Froehlich LA, Fujikura T. Follow-up of infants with single umbilical artery. Pediatrics 1973; 52: 6-13.
21. Singh V, Patel R, Pradhan P. Single umbilical artery and associated hydronephrosis: a report of 2 cases. J Reprod Med 2004; 49: 136-8.
22. Heifetz SA. Single umbilical artery: a statistical analysis of 237 autopsy cases and review of the literature. Perspect Pediatr Pathol 1984; 8: 345-78.
23. Srinivasan R, Arora RS. Do well infants born with an isolated single umbilical artery need investigation? Arch Dis Child 2005; 90: 100-1.
24. Martinez-Payo C, Gaitero A, Tamarit I, Garcia-Espantaleon M, Iglesias Goy E. Perinatal results following the prenatal ultrasound diagnosis of single umbilical artery. Acta Obstet Gynecol Scand 2005; 84: 1068-74.
25. Ebbing C, Kessler J, Moster D, Rasmussen S. Single umbilical artery and risk of congenital malformation: population-based study in Norway. Ultrasound Obstet Gynecol 2020; 55: 510-5.
26. Rodriguez AM, Downs KM. Visceral endoderm and the primitive streak interact to build the fetal-placental interface of the mouse gastrula. Dev Biol 2017; 432: 98-124.

 https://doi.org/10.4132/jptm.2024.07.03

JPTM
Journal of Pathology and Translational Medicine 2024; 58: 219-228
https://doi.org/10.4132/jptm.2024.07.12

ORIGINAL ARTICLE

Paricalcitol prevents MAPK pathway activation and inflammation in adriamycin-induced kidney injury in rats

Amanda Lima Deluque[1], Lucas Ferreira de Almeida[2], Beatriz Magalhães Oliveira[1], Cláudia Silva Souza[3], Ana Lívia Dias Maciel[1], Heloísa Della Coletta Francescato[1], Cleonice Giovanini[1], Roberto Silva Costa[4], Terezila Machado Coimbra[1]

[1]Laboratory of Renal Physiology, Department of Physiology, Ribeirao Preto Medical School, University of Sao Paulo, Ribeirao Preto, Sao Paulo, Brazil; [2]Department of Pediatrics, Child Health Research Center, University of Virginia School of Medicine, Charlottesville, Virginia, United States of America; [3]Transplantation Immunobiology Laboratory, Department of Immunology, Institute of Biomedical Sciences, University of Sao Paulo, Sao Paulo; [4]Laboratory of Renal Pathology, Division of Nephrology, Department of Internal Medicine, Ribeirao Preto Medical School, University of Sao Paulo, Ribeirao Preto, Sao Paulo, Brazil

Background: Activation of the mitogen-activated protein kinase (MAPK) pathway induces uncontrolled cell proliferation in response to inflammatory stimuli. Adriamycin (ADR)-induced nephropathy (ADRN) in rats triggers MAPK activation and pro-inflammatory mechanisms by increasing cytokine secretion, similar to chronic kidney disease (CKD). Activation of the vitamin D receptor (VDR) plays a crucial role in suppressing the expression of inflammatory markers in the kidney and may contribute to reducing cellular proliferation. This study evaluated the effect of pre-treatment with paricalcitol on ADRN in renal inflammation mechanisms. **Methods:** Male Sprague-Dawley rats were implanted with an osmotic minipump containing activated vitamin D (paricalcitol, Zemplar, 6 ng/day) or vehicle (NaCl 0.9%). Two days after implantation, ADR (Fauldoxo, 3.5 mg/kg) or vehicle (NaCl 0.9%) was injected. The rats were divided into four experimental groups: control, n=6; paricalcitol, n=6; ADR, n=7 and, ADR+paricalcitol, n=7. **Results:** VDR activation was demonstrated by increased CYP24A1 in renal tissue. Paricalcitol prevented macrophage infiltration in the glomeruli, cortex, and outer medulla, prevented secretion of tumor necrosis factor-α, and interleukin-1β, increased arginase I and decreased arginase II tissue expressions, effects associated with attenuation of MAPK pathways, increased zonula occludens-1, and reduced cell proliferation associated with proliferating cell nuclear antigen expression. Paricalcitol treatment decreased the stromal cell-derived factor 1α/chemokine C-X-C receptor type 4/β-catenin pathway. **Conclusions:** Paricalcitol plays a renoprotective role by modulating renal inflammation and cell proliferation. These results highlight potential targets for treating CKD.

Key Words: Vitamin D; Inflammation; Macrophages; Cellular proliferation; Renal insufficiency

Received: March 22, 2024 **Revised:** June 26, 2024 **Accepted:** July 11, 2024

Corresponding Author: Amanda Lima Deluque, PhD, Laboratory of Renal Physiology, Department of Physiology, Ribeirao Preto Medical School, University of Sao Paulo, Bandeirantes Avenue, 3900, Ribeirao Preto, Sao Paulo 14049-900, Brazil
Tel: +55-16-981812690, E-mail: amandalima_00@hotmail.com
Corresponding Author: Lucas Ferreira de Almeida, PhD, Department of Pediatrics, Child Health Research Center, University of Virginia School of Medicine, 409 Lane Rd MR4, Charlottesville, Virginia 22903, United States of America
Tel: +1-434-242-2687, E-mail: myr6by@uvahealth.org

Chronic kidney disease (CKD) is characterized by damage to renal endothelial cells and epithelial cells, resulting in tissue fibrosis and inflammation [1]. The loss of cell differentiation in CKD is directly linked to the interaction of cytokines, inflammatory factors, transcription factors, and cellular pathway activation [2]. Inflammation of kidney tissue contributes to the progression of the fibrotic process and CKD, regardless of its etiology [3]. The inflammatory response to epithelial and endothelial cell lesions involves the release of profibrotic and pro-inflammatory cytokines and chemokines, which induce the infiltration of inflammatory cells, mainly macrophages and monocytes, to the glomerulus and renal interstitium [4]. Molecules such as reactive oxygen species, tumor necrosis factor-α (TNF-α), and interleukin-1β (IL-1β) are produced by M1 macrophages. During the repair phase, the macrophage phenotype is converted to M2, conferring the secretion of anti-inflammatory cytokines such as interleukin-10, which contributes to the resolution of the tissue injury [5].

Adriamycin-induced nephropathy (ADRN) is one of the most

pISSN 2383-7837
eISSN 2383-7845

relevant rat models used to study the mechanisms involved in the pathogenesis of CKD. The ADRN rat model is similar to focal segmental glomerulosclerosis in humans, showing morphological characteristics of damage to a portion (segmental) of the glomerular capillaries in some of the glomurulus (focal area). These alterations result in renal dysfunction, glomerular fibrosis, and progressive albuminuria, which was seen in our previous work [1]. Studies have shown that tubulointerstitial inflammation in the ADRN model results in the recruitment of immune cells that secrete pro-inflammatory and profibrotic cytokines such as transforming growth factor β (TGF-β), TNF-α, and IL-1β [6,7]. The mitogen-activated protein kinase (MAPK) pathway also participates in adriamycin (ADR)-induced tubular injury to induce uncontrolled cell proliferation and differentiation in response to extracellular and intracellular stimuli [8]. Smad-dependent TGF-β is the main pathway in the pathogenesis of fibrosis and inflammation in CKD. Smad-independent pathways can also be activated to mediate renal fibrosis, such as the MAPK pathways mediated by extracellular signal-regulated kinase (ERK1/2), p38 MAPK and c-Jun N-terminal kinase (JNK), which represent non-canonical pathways activated by TGF-β1 [9].

Vitamin D receptor (VDR) activators have been used to evaluate the effects of vitamin D (Vit. D) in various experimental and clinical models of kidney disease [10]. Paricalcitol [19-nor-1.25 (OH2D2)], one of the synthetic analogs of calcitriol, exhibits immunomodulatory effects by inhibiting the secretion of pro-inflammatory cytokines [11,12] and profibrotic cytokines such as TGF-β, which consequently decreases cell loss and epithelial-mesenchymal transition by directly activating VDR [1,10]. Vit. D in its active form improved the inflammation and oxidative stress in acute kidney injury induced by cisplatin in rats [13] and exhibited protective effects on the outer and inner medullary structure in progressive kidney disease caused by a lack of renin-angiotensin system during rat kidney development [14]. Previous studies from our laboratory have shown that deficiency of Vit. D during adulthood in rats worsened renal function and disrupted renal structure when associated with diabetes [15], and its supplementation improved endothelial function and structure [5]. However, the direct effects of prior activation of the VDR before the onset of CKD have not yet been fully elucidated. These findings may contribute to better understanding of the mechanisms involved in preventing the progression of CKD. The present work evaluated the effect of paricalcitol treatment on the activity of inflammatory pathways in the ADR-induced CKD model.

MATERIALS AND METHODS

Animals and experimental design

The experimental protocol followed the ethical principles of animal experimentation outlined by the National Council for the Control of Animal Experimentation (CONCEA). This study was approved by the Ethics Committee on the Use of Animals (CEUA) of the Ribeirão Preto Medical School - University of São Paulo (FMRP-USP) (approval no. 194/2017).

Male Sprague-Dawley rats weighing 180–200 g were housed in a temperature-controlled environment (22°C) under a 12-hour light/dark cycle in the animal housing center of the Renal Physiology Laboratory. The animals received diet and water ad libitum. The animals were divided into four experimental groups: control: rats received 0.9% NaCl solution by pump and intravenous injection, n = 5; paricalcitol: rats received paricalcitol (6 ng/day) by pump and 0.9% NaCl solution by intravenous injection, n = 5; ADR: rats received 0.9% NaCl solution by pump and ADR by intravenous injection (3.5 mg/kg), n = 7; and ADR + paricalcitol: rats received paricalcitol (6 ng/day) by pump and ADR by intravenous injection (3.5 mg/kg), n = 7. Paricalcitol (6 ng/day, Zemplar, Abbvie Laboratories, Abbott Park, IL, USA) or vehicle (0.9% sodium chloride [NaCl] solution) was administered via a mini osmotic pump (Model 2004, Alzet, Cupertino, CA, USA) surgically implanted in the animal's back under inhalation anesthesia with isoflurane (Cristália, Sao Paulo, Brazil). The infusion was continuous throughout the 27 days of observation. At 48 hours after implantation, the animals received ADR (3.5 mg/kg, doxorubicin hydrochloride/Fauldoxo, Libbs, Sao Paulo, Brazil) or vehicle (0.9% NaCl solution) via an intravenous injection in the tail vein.

The animals were followed up for 4 weeks after the single injection of ADR without any intervention. On the 27th day, the animals were anesthetized to remove the kidneys for immunohistochemistry, enzyme-linked immunosorbent assay (ELISA) and Western blot.

Immunohistochemical analysis

The kidney tissue was fixed with methacarn solution (60% methanol, 30% chloroform, and 10% acetic acid); after 24 hours, the solution was replaced with 70% alcohol. The tissue was embedded in paraffin, deparaffinized, and hydrated. Nonspecific antigen binding was blocked by incubation for 20 minutes with goat serum and endogenous peroxidase blocking. The slides were microwaved and immersed in citrate buffer pH 6.0 or ethylenediaminetetraacetic acid (EDTA) pH 8.5 for antigen retrieval. The

 https://doi.org/10.4132/jptm.2024.07.12

sections were incubated with antibody against cluster of differentiation 68 (CD68, 1/100, MCA341R, Bio-Rad Laboratories Inc., Hercules, CA, USA) overnight at 4°C. The slides were then washed with buffer (phosphate bufered saline, 0.15 M NaCl, and PO4 buffer, pH = 7.4) and incubated with anti-mouse secondary antibody for 30 minutes. Avidin-biotin-peroxidase complexes (Vector Laboratories, Newark, CA, USA) and 3,3'-diaminobenzidine (Sigma Chemical Company, St. Louis, MO, USA) were used to detect the antigens. The sections were counterstained with methyl green, dehydrated, and mounted. Images were obtained and data were quantified at high magnification (400×). Thirty consecutive 0.1 mm^2 fields of the cortex and 20 consecutive 0.1 mm^2 fields of the outer medullary compartment were evaluated for CD68 expression. Additionally, 30 cortical and 20 juxta-medullary glomeruli were assessed. The glomerular, tubulo-interstitial cortical, and medullary changes were quantified using NIH Image J software (Bethesda, MD, USA), and the average values per kidney were calculated. The results are expressed as the percentage of positive labeling in the glomerulus, cortex, and outer medulla.

ELISA analysis

Kidney tissues were homogenized in lysis buffer (50 mM Tris-hydrochloric acid [HCl], pH 7.4; 150 mM NaCl; 1% Triton X-100; protease inhibitor cocktail [100×] and 0.001 M EDTA, pH 8 [Thermo Fisher Scientific Inc., Waltham, MA, USA]) and centrifuged at 4°C at 10,000 rpm for 20 minutes. The concentrations of TNF-α and IL-1β in kidney tissue homogenates were evaluated by ELISA kits (R&D Systems Inc., Minneapolis, MN, USA). The Bradford method was used to determine the protein levels in lysates; the results were corrected for the total protein quantity in tissue and expressed in pg/mg of tissue protein.

Western blot analysis

Kidney tissues were lysed as for ELISA. Protein samples (60 μg) were heated to 100°C in sample buffer containing β-mercaptoethanol. The samples were separated by polyacrylamide gel electrophoresis (sodium dodecyl sulfate polyacrylamide gel electrophoresis, 12%) and transferred to nitrocellulose membranes overnight at 4ºC. The membranes were incubated for 1 hour in blocking buffer (Tris-buffered saline Tween 20, TBSt, 5% skimmed milk) or 3% bovine serum albumin and washed in buffer (TBSt, 0.1% Tween 20, pH 7.6). The membranes were then incubated overnight at 4°C with antibodies against arginase I (1/1,000, sc-18351, Santa Cruz Biotechnology, Santa Cruz, CA, USA), arginase II (1/1,000, sc-18357, Santa Cruz Biotechnology), CD68 (1/2,000, MCA341R, Bio-Rad Laboratories Inc.), C-X-C chemokine receptor type 4 (CXCR4; 1/500, LS-B6709, LifeSpan BioSciences Inc., Lynnwood, WA, USA), 24-hydroxylase (CYP24A1, 1/500, H0000159-M02, Abnova, San Diego, CA, USA), glyceraldehyde-3-phosphate dehydrogenase (GAPDH; 1/1,000, cod. 2118L, Cell Signaling Technology, Danvers, MA, USA), nuclear factor κB alpha inhibitor (IκBα, 1/1,000, sc-371, Santa Cruz Biotechnology), nuclear factor κB beta inhibitor (IκBβ, 1/1,000, sc-945, Santa Cruz Biotechnology), nuclear factor-κB (NF-κB; 1/1,000, sc-7151, Santa Cruz Biotechnology), proliferating cell nuclear antigen (PCNA; 1/500, P8825, Sigma Chemical Company), phospho-extracellular signal-regulated kinase 1/2 (p-ERK1/2; 1/500, sc-7383, Santa Cruz Biotechnology); phospho-c-Jun N-terminal kinase (p-JNK; sc-6254, Santa Cruz Biotechnology), phospho-p38 MAPK (1/500, P8825, Sigma Chemical Company), stromal cell-derived factor 1α (SDF-1α; 1/500, 14-7992-83, eBioscience, San Diego, CA, USA), zonula occludens-1 (ZO-1; 1/250, 61-7300, Zymed, Carlsbad, CA, USA), and β-catenin (1/2,000, sc-7199, Santa Cruz Biotechnology). The membranes were then washed and incubated with peroxidase-conjugated mouse anti-IgG (P0447, 1/5,000, Dako Corporation, Copenhagen, Denmark), rabbit anti-IgG (P0448, 1/2,000, 1/5,000 or 1/10,000, Dako Corporation or sc-2357 [Santa Cruz Biotechnology]) or anti-goat (sc-2768, 1/5,000, Santa Cruz Biotechnology) for 1 hour at room temperature. GAPDH was used as the loading control. Bands were visualized using enhanced chemiluminescence reagents (Sigma-Aldrich) and an imaging system (Kodak Gel Logic 2200, Austin, TX, USA). Band intensity was quantified by densitometry using ImageJ NIH 1.52A imaging software (http://www.nih.gov). Protein expression was determined as the percentage of the band density of the protein of interest and the reference protein compared with the control group. The control value was designated as 100%.

Statistical analysis

Data were tested for normality using the Kolmogorov-Smirnov distribution normality test. One-way analysis of variance (ANOVA) followed by the Newman-Keuls multiple comparisons test was used to analyze normally distributed data. Data are expressed as mean ± standard error of the mean. The Kruskal-Wallis nonparametric test, followed by Dunn's post-test, was used to analyze non-normally distributed data expressed as medians and percentiles (25%–75%). Statistical analyses were conducted using GraphPad Prism ver. 9.0 for Windows (GraphPad Software, San Diego, CA, USA). $p < .05$ was considered statistically significant.

RESULTS

Paricalcitol treatment increased Vit. D content in kidney tissue

The expression of CYP24A1, an enzyme that finely regulates Vit. D levels, was used as an indicator of activated intrarenal Vit. D content. A reduction of CYP24A1 expression was observed in the rats in the ADR group compared with the control and paricalcitol groups (Fig. 1), indicating less Vit. D in this tissue. These changes in CYP24A1 expression were significantly prevented in the ADR + paricalcitol group compared with the ADR group, which shows a higher content of the Vit. D in the kidneys of animals treated with paricalcitol.

Paricalcitol treatment attenuated macrophage infiltration induced by ADR

The expression of CD68, a marker of macrophages and monocytes, was increased in the glomerulus, cortex, and outer medulla of animals in the ADR group compared with the control and paricalcitol groups. Compared with the ADR group, the ADR + paricalcitol group showed a decrease in the expression of CD68 in all compartments (Fig. 2A–D). Western blot analysis of CD68 showed similar results (Fig. 2E).

There was an increase in TNF-α and IL-1β (pro-inflammatory cytokines) in the ADR group compared with the control and paricalcitol groups. The cytokine levels were lower in the ADR + paricalcitol group than in the ADR group (Fig. 2F, G). A reduction in arginase I expression, here used as a repair macrophage marker, was observed in the kidney tissue of the animals in the ADR group compared with control and paricalcitol groups. This reduction was reversed in the ADR + paricalcitol group compared with the ADR groups. Also for arginase I, a lower expression was seen in the animals in the paricalcitol group, demonstrating the effect of this Vit. D analog in modulating the differentiation of tissue macrophages (Fig. 2H). Arginase II was increased in the ADR group compared with the control group. This increase was attenuated in the ADR+paricalcitol group compared with the ADR group (Fig. 2I).

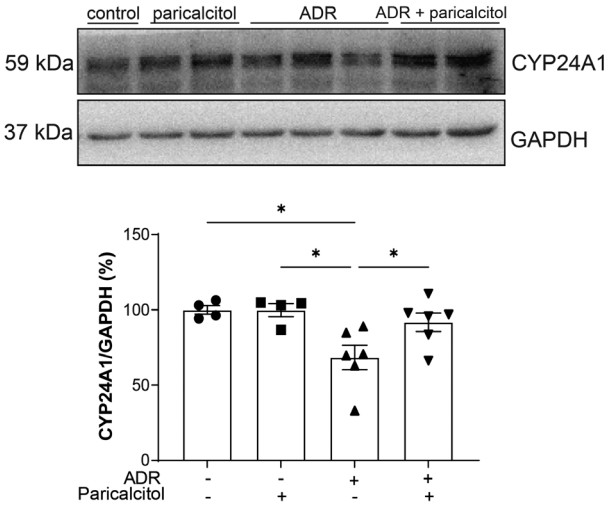

Fig. 1. Western blot analysis of CYP24A1 in kidney. Glyceraldehyde-3-phosphate dehydrogenase (GADPH) was used as loading control. Data from the control (dots), paricalcitol (squares), adriamycin (ADR; upward facing triangles) and ADR + paricalcitol (downward facing triangles) groups. n = 4–6 for each group. One-way ANOVA and Newman-Keuls multiple comparisons; data are expressed as mean ± standard error of the mean. *p < .05.

Paricalcitol treatment regulated MAPK pathway activation and attenuated the changes in ZO-1 and PCNA expression induced by ADR

We evaluated the activation of MAPK-related pathways and the inflammatory process. The level of p-p38 was lower in the ADR + paricalcitol group compared with the control, paricalcitol, and ADR groups (Fig. 3A). An increase in p-JNK and p-ERK1/2 was seen in the ADR group compared with the control group; this increase was attenuated in the ADR + paricalcitol group (Fig. 3B, C).

The expression of ZO-1 was decreased in the ADR group compared with the control and paricalcitol groups. The ADR + paricalcitol group also showed a reduction of ZO-1 expression compared to control and paricalcitol groups. However, this expression was increased when compared to ADR group (Fig. 3D). A significant reduction in PCNA in kidney tissue was observed in the ADR+paricalcitol group compared with the ADR group (Fig. 3E).

Paricalcitol treatment attenuated the pro-inflammatory pathways induced by ADR

No difference was observed in the expression of the NF-κB protein among the four groups (p > .05) (Fig. 4A). However, a reduction in the inhibitory proteins IκBα and IκBβ was observed in the ADR group compared with the control and paricalcitol groups. The ADR + paricalcitol group also significantly reduced IκBα levels compared to the control and paricalcitol groups, but increased compared to the ADR group (Fig. 4B). The same profile was observed for IκBβ (Fig. 4C).

The SDF-1α/CXCR4 pathway was significantly increased in the ADR group compared with the control and paricalcitol groups. Treatment with active Vit. D attenuated the expression

https://doi.org/10.4132/jptm.2024.07.12

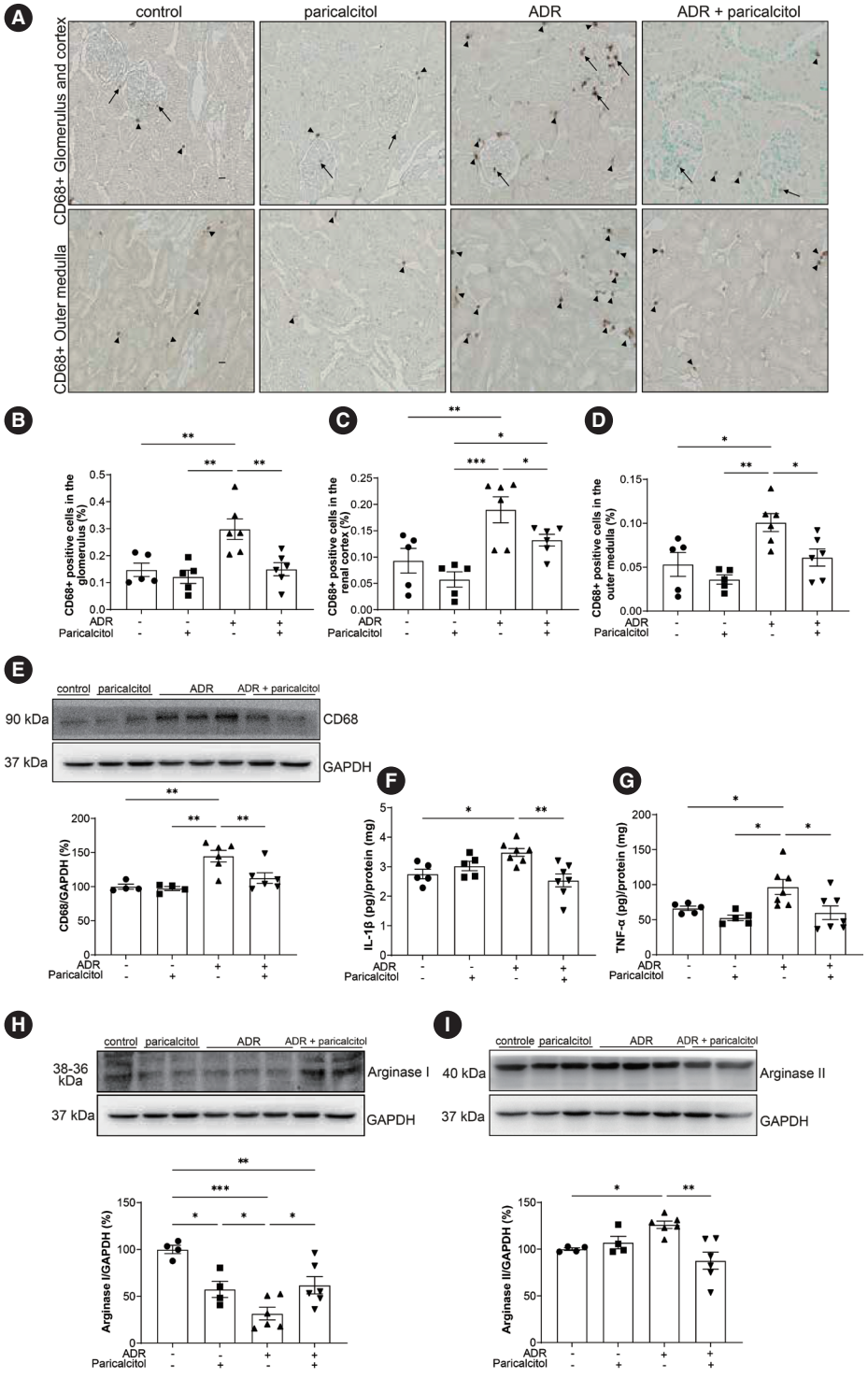

Fig. 2. Analysis of macrophages in kidney tissue. (A) Immunolocalization of CD68 in renal compartments. Arrows indicate positive expression of CD68 in the glomerulus. Arrowheads indicate positive CD68 expression in the tubulointerstitial compartments. Percentage of CD68-positivity in the glomerulus (B), in the cortex (C), and in the outer medulla (D). (E) Densitometric analysis of CD68. Cytokines and macrophage profile in kidney tissue. Enzyme-linked immunosorbent assay for interleukin-1β (IL-1β) (F) and tumor necrosis factor-α (TNF-α) (G). Densitometric analysis of arginase I (H) and arginase II (I) in the kidney. Glyceraldehyde-3-phosphate dehydrogenase (GADPH) was used as loading control. Data from the control (dots), paricalcitol (squares), adriamycin (ADR; upward facing triangles) and ADR+paricalcitol (downward facing triangles) groups. n=4–6 for each group. One-way ANOVA and Newman-Keuls multiple comparisons; data are expressed as mean±standard error of the mean. *p<.05, **p<.01, ***p<.001.

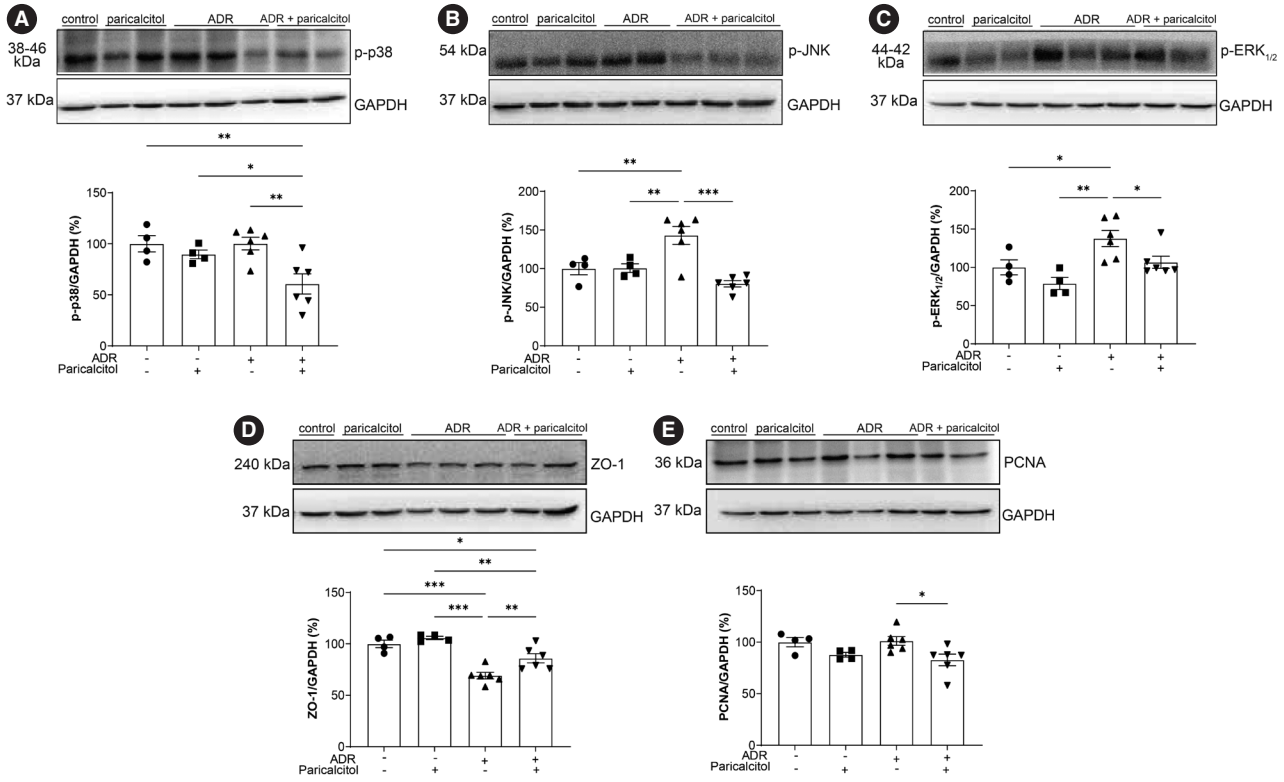

Fig. 3. Activation of mitogen-activated protein kinase pathways. Analysis of p-p38 (A), p-JNK (B), p-ERK1/2 (C), zonula occludens-1 (ZO-1) (D), and proliferating cell nuclear antigen (PCNA) (E). Glyceraldehyde-3-phosphate dehydrogenase (GADPH) was used as loading control. Data from the control (dots), paricalcitol (squares), adriamycin (ADR; upward facing triangles) and ADR + paricalcitol (downward facing triangles) groups. n = 4–6 for each group. For (A–D), one-way ANOVA and Newman-Keuls multiple comparisons; data are expressed as mean±standard error of the mean. *p<.05, **p<.01, ***p<.001.

of these pro-inflammatory proteins (Fig. 4D, E). The β-catenin protein showed similar expression in the ADR group compared with the control groups and its expression was attenuated in the kidneys in the ADR + paricalcitol group (Fig. 4F).

DISCUSSION

In the present study, we investigated the role of active Vit. D in ADR-induced kidney damage. The protective effects of paricalcitol may be related to increased expression of CYP24A1, which contributed to reduced expression of mediators of the Smad2/3-independent TGF-β pathway, thus reducing the fibrotic process observed in our study. The data also demonstrated the effect of paricalcitol in reducing the inflammatory process in the ADR rat model. Together, these results demonstrate that paricalcitol may attenuate CKD by increasing the availability of active Vit. D in renal tissue to generate anti-inflammatory and anti-fibrotic responses. Vit. D levels are finely regulated by the CYP24A1 enzyme or 24-hydroxylase, which catabolizes calcidiol and calcitriol. Thus, CYP24A1 plays an essential role in modulating local Vit. D activity and can be an indicator of active Vit. D in tissue [16,17]. Vit. D in its active and circulating form may increase the levels of its receptor, VDR, as observed in our previous study [1], in ADR-induced kidney injury, contributing to the recovery of the changes in kidney function and structure.

Some evidence has indicated a therapeutic effect of Vit. D in CKD in humans, mainly due to its antifibrotic and anti-inflammatory effects related to the reduction of cytokine secretion via the VDR. Paricalcitol was also shown to reduce vascular calcification and help in the preservation of kidney function from its antiproteinuric effects [12,18]. The accumulation and migration of macrophages in kidney diseases are associated with functional and structural kidney damage [18]. Our study demonstrated that paricalcitol attenuated the accumulation of macrophages in all the compartments evaluated in the ADR + paricalcitol group animals and reduced the secretion of cytokines and activating pro-inflammatory pathways. TNF-α and IL-1β were increased

 https://doi.org/10.4132/jptm.2024.07.12

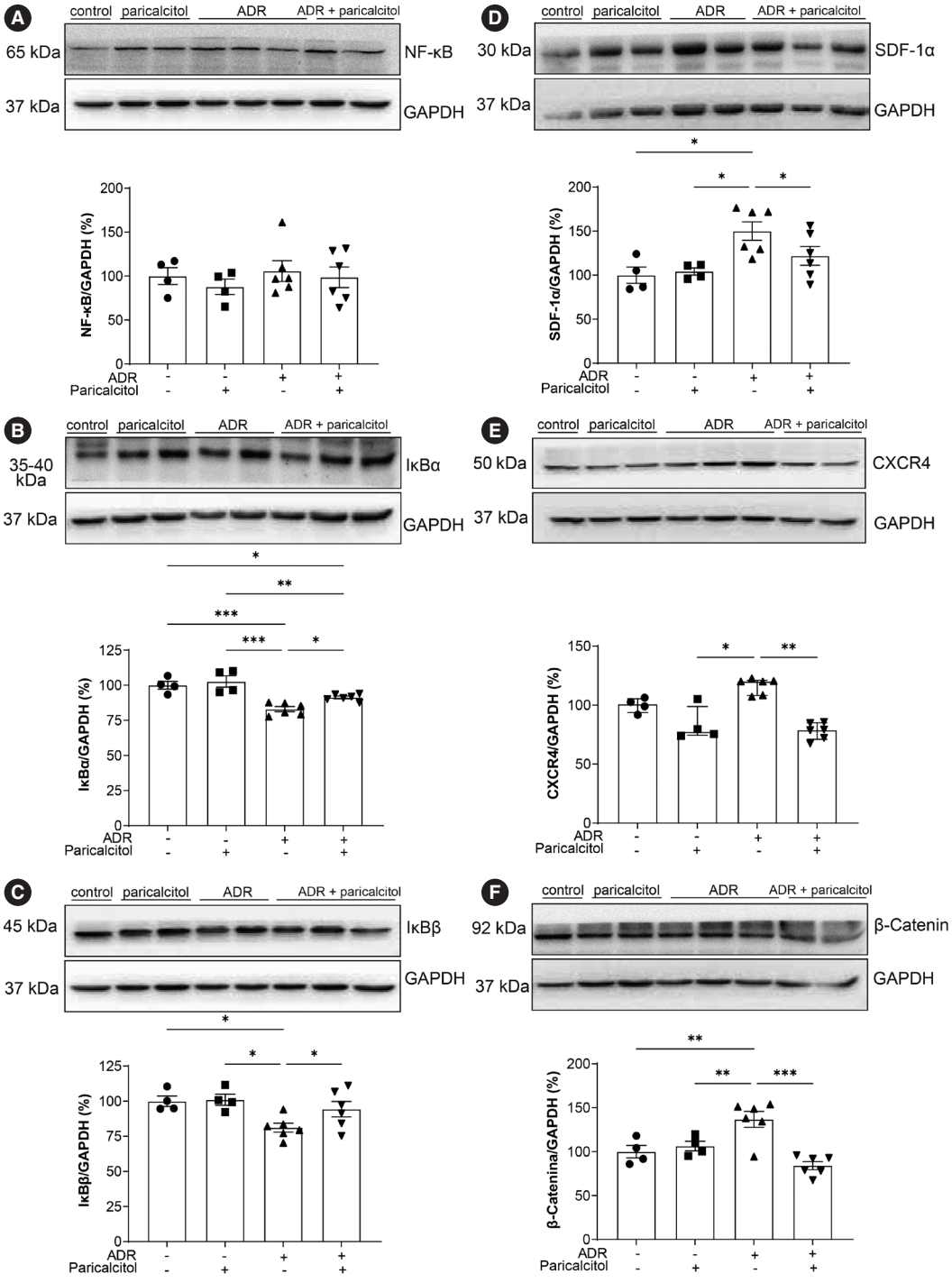

Fig. 4. Analysis of pro-inflammatory pathways in renal tissue. Analysis of nuclear factor-κB (NF-κB) (A), nuclear factor κB alpha inhibitor (IκBα) (B), nuclear factor κB beta inhibitor (IκBβ) (C), stromal cell-derived factor 1α (SDF-1α) (D), C-X-C chemokine receptor type 4 (CXCR4) (E), and β-catenin (F). Glyceraldehyde-3-phosphate dehydrogenase (GADPH) was used as loding control. Data from the control (dots), paricalcitol (squares), adriamycin (ADR; upward facing triangles) and ADR+paricalcitol (downward facing triangles) groups. n=4–6 for each group for (A, B, C, D, F). One-way ANOVA and Newman-Keuls multiple comparisons; data are expressed as mean±standard error of the mean. (E) Kruskal-Wallis and Dunn's post-test; data are expressed as median and percentiles (25%–75%). *p<.05, **p<.01, ***p<.001.

in ADR animals, pointing to the response of pro-inflammatory activity caused by ADR in rats. In our study, paricalcitol likely exerted anti-inflammatory effects by increasing arginase I levels. Arginase I and II are involved in the production of NO by the endothelium and also with the immune system modulation. While arginase II overexpression in macrophages increases the production of pro-inflammatory cytokines, arginase I inhibits and attenuates inflammation in cardiac tissue [19]. In this study, we observed an increase in arginase I and a reduction in arginase II in the ADR animals treated with paricalcitol. These results demonstrated that paricalcitol has an anti-inflammatory action, as evidenced by a decrease in M1 macrophages and an increase in M2 macrophages. Thus, the macrophages in the kidneys of ADR + paricalcitol animals, at least part of them, have anti-inflammatory and reparative activity in the tissue, improving tissue fibrosis and modulating the immune response. Our study showed a reduction of arginase I in the paricalcitol group compared to control. This result reinforces the role of Vit. D in protecting tissue when an inflammatory process occurs. Otherwise, repair macrophages are not needed. Under normal conditions, macrophages are not recruited to the healthy tissue, with fewer pro-inflammatory and fibrotic actions induced by ADR and angiopoietin-2 [1].

ADR induces the phosphorylation of MAPKs (p38, JNK, and ERK1/2) [8], which may be associated with podocyte loss and proteinuria. MAPK signaling is triggered by mechanical and chemical stressors, leading to the regulation of cell proliferation, differentiation, and apoptosis [20,21]. We saw that all MAPK signaling pathways were activated in the kidneys of the ADR group compared with controls. Paricalcitol attenuated these changes, which contributed to the improvement in kidney function and structure. Vit. D plays an active regulatory role in attenuating the phosphorylation of ERK1/2, JNK and p38, which is reflected in a reduction in cell proliferation [22,23].

The progression of CKD is also associated with damage to structural proteins, such as ZO-1, which tightens epithelial cell layer junctions to create a selective paracellular barrier in the glomerulus and tubules [24]. ZO-1 is a cytoplasmic protein that transmits information to the nucleus in response to cell-cell contact. ZO-1 modulates cell cycle progression and controls cell proliferation and differentiation through interaction with ZO-1-associated nucleic acid (ZONAB) [24]. ZONAB promotes the expression of the PCNA gene, promoting the cell cycle transition from G1 phase to S phase [25]. In our study, ZO-1 was decreased in the ADR group. The loss of cellular integrity and ZO-1 decrease can generate abnormal ZONAB transcripts, leaving this protein free to induce PCNA transcription [26]. There was an attenuation of PCNA in the kidney tissue of animals in the ADR+paricalcitol group. We also found that PCNA is attenuated by Vit. D, reducing the exacerbated proliferation of various cell types, especially mesenchymal cells and macrophages [13,15,23].

VDR activation also suppresses activation of the MAPKs and NF-κB pathways [27,28]. In our study, no differences were observed in the expression of NF-κB in the treated groups, although its two inhibitory proteins, IκBα and IκBβ, were decreased in the ADR + paricalcitol group. Studies have shown the anti-inflammatory role of active Vit. D in reducing the activation of TGF-β1/Smad2/3, a mechanism that contributes to the greater availability of Smad7, increasing the expression and activity of IκBα and contributing to the reduction of inflammatory cell infiltration in renal tissue [29]. Thus, these results suggest that Vit. D functions in these pathways, even if indirectly. In the ADRN model, CXCR4 is activated by the SDF-1α ligand, which triggers an increase in β-catenin to induce podocyte injury and proteinuria [30], showing new TGF-β–independent pathways for the evolution of proteinuric diseases. Previous study from our laboratory showed decreased CXCR4 in animals with acute kidney injury induced by cisplatin treated with calcitriol, with more significant regeneration of tubular cells and less endothelial dysfunction [13]. Active Vit. D reduces the expression of profibrotic pathways such as Wnt/β-catenin, decreasing glycogen synthase kinase-3β and Snail, proteins involved in the epithelial-mesenchymal transition. Decreasing this mechanism also leads to lower proteinuria through the direct physical interaction of VDR/β-catenin, reducing nuclear β-catenin and therefore cell proliferation [31]. Again, in our model, we observed the direct and indirect actions of paricalcitol and endothelium-tubular cell interaction to reduce mechanisms of inflammation and fibrosis in CKD.

Our study showed that paricalcitol attenuates the renal inflammatory process induced by ADR in rats. Paricalcitol induced anti-inflammatory and anti-proliferative effects by inhibiting macrophage accumulation and cytokine secretion and inducing M2 macrophages in renal tissue, regulating the MAPK, NF-κB/IκBα/IκBβ and CXCR4/SDF-1α/β-catenin pathways. Our results suggest that paricalcitol may exhibit anti-fibrotic, anti-inflammatory, and anti-proliferative therapeutic roles in preventing renal injury in early CKD.

Ethics Statement

The animal study protocol was approved by the Brazilian College of Animal Experimentation and the Animal Experimentation Committee of the University of Sao Paulo at Ribeirao Preto Medical School (COBEA/CE-

https://doi.org/10.4132/jptm.2024.07.12

TEA/FMRP-USP, protocol no. 194/2017).

Availability of Data and Material

The datasets generated or analyzed during the study are available from the corresponding author on reasonable request.

Code Availability

Not applicable.

ORCID

Amanda Lima Deluque	https://orcid.org/0000-0002-8827-7172
Lucas Ferreira de Almeida	https://orcid.org/0000-0002-5731-1219
Beatriz Magalhães Oliveira	https://orcid.org/0000-0002-9008-4425
Cláudia Silva Souza	https://orcid.org/0000-0002-3210-1434
Ana Lívia Dias Maciel	https://orcid.org/0009-0009-8285-9591
Heloísa Della Coletta Francescato	https://orcid.org/0000-0001-6034-1235
Cleonice Giovanini	https://orcid.org/0009-0002-7177-3126
Roberto Silva Costa	https://orcid.org/0000-0003-3639-0189
Terezila Machado Coimbra	https://orcid.org/0000-0002-2906-8231

Author Contributions

Conceptualization: ALD, LFA, BMO, CSS, ALDM, HDCF, CG, RSC, TMC. Data curation: ALD, BMO, CSS, ALDM. Formal analysis: ALD, BMO, CSS, ALDM. Funding acquisition: TMC, RSC. Methodology: HDCF, CG. Resources: TMC, RSC. Writing—original draft: ALD, LFA. Writing—review & editing: ALD, LFA, BM, CSS, ALDM, HDCF, CG, RSC, TMC. Approval of final manuscript: all authors.

Conflicts of Interest

The authors declare that they have no potential conflicts of interest.

Funding Statement

This work was supported by the Coordenação de Aperfeiçoamento de Pessoal de Nível Superi-or – Brasil (CAPES) – Finance Code 001 and the Conselho Nacional de Desenvolvimento Científico e Tecnológico (CNPq, grant number 303252/2021-9).

Acknowledgments

The authors thank Guilherme Lemos and Flávio Leite for help with the immunohistochemistry sections.

References

1. Deluque AL, Oliveira BM, Souza CS, et al. Paricalcitol improves the angiopoietin/Tie-2 and VEGF/VEGFR2 signaling pathways in adriamycin-induced nephropathy. Nutrients 2022; 14: 5316.
2. Hua W, Ten Dijke P, Kostidis S, Giera M, Hornsveld M. TGFbeta-induced metabolic reprogramming during epithelial-to-mesenchymal transition in cancer. Cell Mol Life Sci 2020; 77: 2103-23.
3. Meng XM, Nikolic-Paterson DJ, Lan HY. Inflammatory processes in renal fibrosis. Nat Rev Nephrol 2014; 10: 493-503.
4. Jourde-Chiche N, Fakhouri F, Dou L, et al. Endothelium structure and function in kidney health and disease. Nat Rev Nephrol 2019; 15: 87-108.
5. Tang PM, Nikolic-Paterson DJ, Lan HY. Macrophages: versatile players in renal inflammation and fibrosis. Nat Rev Nephrol 2019; 15: 144-58.
6. Zoja C, Abbate M, Remuzzi G. Progression of renal injury toward interstitial inflammation and glomerular sclerosis is dependent on abnormal protein filtration. Nephrol Dial Transplant 2015; 30: 706-12.
7. Wu Q, Li W, Zhao J, et al. Apigenin ameliorates doxorubicin-induced renal injury via inhibition of oxidative stress and inflammation. Biomed Pharmacother 2021; 137: 111308.
8. Li W, He W, Xia P, et al. Total extracts of *Abelmoschus manihot* L. attenuates adriamycin-induced renal tubule injury via suppression of ROS-ERK1/2-mediated NLRP3 inflammasome activation. Front Pharmacol 2019; 10: 567.
9. Sureshbabu A, Muhsin SA, Choi ME. TGF-beta signaling in the kidney: profibrotic and protective effects. Am J Physiol Renal Physiol 2016; 310: F596-F606.
10. Martinez-Arias L, Panizo S, Alonso-Montes C, et al. Effects of calcitriol and paricalcitol on renal fibrosis in CKD. Nephrol Dial Transplant 2021; 36: 793-803.
11. Egido J, Martinez-Castelao A, Bover J, et al. The pleiotropic effects of paricalcitol: beyond bone-mineral metabolism. Nefrologia 2016; 36: 10-8.
12. Salanova Villanueva L, Gil Giraldo Y, Santos Sanchez-Rey B, Aguilera Peralta A. Paricalcitol regulatory effect on inflammatory, fibrotic and anticalcificating parameters in renal patiente: far beyond mineral bone disease regulation. Nefrologia (Engl Ed) 2020; 40: 171-9.
13. Oliveira BM, de Almeida LF, Deluque AL, et al. Calcitriol reduces the inflammation, endothelial damage and oxidative stress in AKI caused by cisplatin. Int J Mol Sci 2022; 23: 15877.
14. Deluque AL, de Almeida LF, Francescato HD, et al. Effect of calcitriol on the renal microvasculature differentiation disturbances induced by AT(1) blockade during nephrogenesis in rats. Front Med (Lausanne) 2020; 7: 23.
15. Souza CS, Deluque AL, Oliveira BM, et al. Vitamin D deficiency contributes to the diabetic kidney disease progression via increase ZEB1/ZEB2 expressions. Nutr Diabetes 2023; 13: 9.
16. Bikle DD. Vitamin D metabolism, mechanism of action, and clinical applications. Chem Biol 2014; 21: 319-29.
17. Reis NG, Francescato HD, de Almeida LF, Silva C, Costa RS, Coimbra TM. Protective effect of calcitriol on rhabdomyolysis-induced acute kidney injury in rats. Sci Rep 2019; 9: 7090.
18. Agarwal R, Acharya M, Tian J, et al. Antiproteinuric effect of oral paricalcitol in chronic kidney disease. Kidney Int 2005; 68: 2823-8.
19. Huen SC, Cantley LG. Macrophages in renal injury and repair. Annu Rev Physiol 2017; 79: 449-69.
20. Li Z, Wang L, Ren Y, et al. Arginase: shedding light on the mechanisms and opportunities in cardiovascular diseases. Cell Death Discov 2022; 8: 413.
21. Sui X, Kong N, Ye L, et al. p38 and JNK MAPK pathways control the balance of apoptosis and autophagy in response to chemotherapeutic agents. Cancer Lett 2014; 344: 174-9.
22. Zhou Y, Wu Q, Du Z, et al. Verbena attenuates adriamycin-induced renal tubular injury via inhibition of ROS-ERK1/2-NLRP3 signal pathway. Evid Based Complement Alternat Med 2022; 2022: 7760945.
23. Chung S, Kim S, Kim M, et al. Treatment combining aliskiren with paricalcitol is effective against progressive renal tubulointerstitial fibrosis via dual blockade of intrarenal renin. PLoS One 2017; 12: e0181757.
24. de Almeida LF, Francescato HD, da Silva CG, Costa RS, Coimbra TM. Calcitriol reduces kidney development disorders in rats provoked by losartan administration during lactation. Sci Rep 2017; 7:

11472.
25. Diaz-Coranguez M, Liu X, Antonetti DA. Tight junctions in cell proliferation. Int J Mol Sci 2019; 20: 5972.
26. He L, Zhou Z, Shao Y, et al. Bradykinin potentially stimulates cell proliferation in rabbit corneal endothelial cells through the ZO-1/ZONAB pathway. Int J Mol Med 2018; 42: 71-80.
27. Raggi C, Luciani A, Nevo N, Antignac C, Terryn S, Devuyst O. Dedifferentiation and aberrations of the endolysosomal compartment characterize the early stage of nephropathic cystinosis. Hum Mol Genet 2014; 23: 2266-78.
28. Li X, Liu J, Zhao Y, et al. 1,25-dihydroxyvitamin D3 ameliorates lupus nephritis through inhibiting the NF-kappaB and MAPK signalling pathways in MRL/lpr mice. BMC Nephrol 2022; 23: 243.
29. Wang Q, He Y, Shen Y, et al. Vitamin D inhibits COX-2 expression and inflammatory response by targeting thioesterase superfamily member 4. J Biol Chem 2014; 289: 11681-94.
30. Meng XM, Nikolic-Paterson DJ, Lan HY. TGF-beta: the master regulator of fibrosis. Nat Rev Nephrol 2016; 12: 325-38.
31. Mo H, Ren Q, Song D, et al. CXCR4 induces podocyte injury and proteinuria by activating beta-catenin signaling. Theranostics 2022; 12: 767-81.

https://doi.org/10.4132/jptm.2024.07.12

JPTM
Journal of Pathology and Translational Medicine 2024; 58: 229-240
https://doi.org/10.4132/jptm.2024.07.13

ORIGINAL ARTICLE

Artificial intelligence algorithm for neoplastic cell percentage estimation and its application to copy number variation in urinary tract cancer

Jinahn Jeong[1], Deokhoon Kim[1], Yeon-Mi Ryu[2], Ja-Min Park[2], Sun Young Yoon[2], Bokyung Ahn[1], Gi Hwan Kim[1], Se Un Jeong[1]*, Hyun-Jung Sung[1], Yong Il Lee[1], Sang-Yeob Kim[2], Yong Mee Cho[1]

[1]Department of Pathology, Asan Medical Center, University of Ulsan College of Medicine, Seoul;
[2]Asan Institute for Life Sciences, Asan Medical Center, Seoul, Korea

Background: Bladder cancer is characterized by frequent mutations, which provide potential therapeutic targets for most patients. The effectiveness of emerging personalized therapies depends on an accurate molecular diagnosis, for which the accurate estimation of the neoplastic cell percentage (NCP) is a crucial initial step. However, the established method for determining the NCP, manual counting by a pathologist, is time-consuming and not easily executable. **Methods:** To address this, artificial intelligence (AI) models were developed to estimate the NCP using nine convolutional neural networks and the scanned images of 39 cases of urinary tract cancer. The performance of the AI models was compared to that of six pathologists for 119 cases in the validation cohort. The ground truth value was obtained through multiplexed immunofluorescence. The AI model was then applied to 41 cases in the application cohort that underwent next-generation sequencing testing, and its impact on the copy number variation (CNV) was analyzed. **Results:** Each AI model demonstrated high reliability, with intraclass correlation coefficients (ICCs) ranging from 0.82 to 0.88. These values were comparable or better to those of pathologists, whose ICCs ranged from 0.78 to 0.91 in urothelial carcinoma cases, both with and without divergent differentiation/subtypes. After applying AI-driven NCP, 190 CNV (24.2%) were reclassified with 66 (8.4%) and 78 (9.9%) moved to amplification and loss, respectively, from neutral/minor CNV. The neutral/minor CNV proportion decreased by 6%. **Conclusions:** These results suggest that AI models could assist human pathologists in repetitive and cumbersome NCP calculations.

Key Words: Artificial intelligence; Fluorescent antibody technique; Urologic neoplasms

Received: May 27, 2024 **Revised:** July 1, 2024 **Accepted:** July 11, 2024
Corresponding Author: Yong Mee Cho, MD, PhD, Department of Pathology, Asan Medical Center, University of Ulsan College of Medicine, 88 Olympic-ro 43-gil, Songpa-gu, Seoul 05505, Korea
Tel: +82-2-3010-4560, Fax: +82-2-472-7898, E-mail: yongcho@amc.seoul.kr

*Current address: Department of Pathology, Ewha Womans University Mokdong Hospital, Ewha Womans University College of Medicine, Seoul, Korea

Bladder cancer is one of the most highly mutated tumors with recurrent mutations, creating potential therapeutic targets in the majority (69%) of patients [1]. Recently, personalized treatments based on recurrent genetic alterations such as pan–fibroblast growth factor receptor (FGFR) inhibitors targeting *FGFR3* mutations and *FGFR3/2* fusions have been emerging, where an accurate molecular diagnosis is a prerequisite for such personalized treatment [2]. In addition, several agents such as human epidermal growth factor receptor 2 (HER2)–targeting antibody-drug conjugates for HER2-overexpressing bladder cancer are under investigation in clinical trials with promising efficacy reported [3,4].

Molecular tests such as targeted next-generation sequencing (NGS) are widely used not only to define disease-associated genetic alterations for diagnostic purposes but also to find drug-associated clinically actionable targets for personalized medicine. As an initial step of NGS, an accurate assessment of the neoplastic cell percentage (NCP) is essential because solid tumors, including bladder cancer, contain a variable amount of non-neoplastic cells such as desmoplastic fibroblasts, inflammatory cells, vascular endothelial cells, and smooth muscle cells. Depending on the NCP, an NGS test may proceed or be canceled for some specimens, especially those with a low tumor content near the cutoff level of the test. This is because NGS testing with insufficient neoplastic cells may lead to false negative results, even in the presence of a variant, when the test is conducted despite in-

pISSN 2383-7837
eISSN 2383-7845

adequate cellularity. Furthermore, an inappropriately assessed NCP produces noise and distorts the relationship between read counts, resulting in an inaccurate estimation of the copy number variation (CNV) in the NGS data [5].

NCP, also referred to as normal cell contamination, is defined as the fraction of cancer cells in a tumor. Currently, NCP is determined by visual examination by pathologists of hematoxylin and eosin (H&E) stained slides of tumor sections [6,7]. However, these pathologist estimates have limited accuracy and a wide range of interobserver variation [6,8]. To resolve this challenge, several in silico methods were developed by using genomic, epigenomic, or transcriptomic profiles. Although they appear to be accurate and bypass the effort of pathologists, these molecular estimates are obtained only after sequencing and analysis of the corresponding molecular tests has been completed. It has also been shown that there is poor concordance between pathologist and molecular estimates of NCP and limited concordance between genomic and transcriptomic derived estimates [8,9].

In bladder cancer, the accurate measurement of NCP is a difficult task due to its wide range of histologic variation, including sarcomatous dedifferentiation, mucinous and glandular differentiation, significant inflammatory cell infiltration, etc. The lack of an easily applicable and reproducible cell counting method that can be used as the ground truth value has hampered the development of a method for NCP assessment. Multiplex immunofluorescence (mIF) has been developed to simultaneously assess multiple biomarkers and allows a quantitative assessment of the tumor microenvironment, which consists of various immune cells and stromal cells in addition to tumor cells. Therefore, we assumed that mIF could be used for phenotyping and counting tumor cells, stromal cells, and immune cells in bladder cancer to provide a ground truth value of NCP, which is a prerequisite for the development of an accurate method of NCP assessment.

Artificial intelligence (AI) has emerged as a useful tool for quantitative and qualitative analyses of digital histopathology images [10]. AI-based quantitative image analysis has been reported to be able to estimate NCP in breast cancer and lung cancer, but not in urinary tract cancer [11-13]. In the present study, we developed AI models using digital images of urinary tract malignancies and convolutional neural network (CNN) models. The performance of the AI models was evaluated using mIF-driven NCP as ground truth values and compared to pathologists' estimates. The impact of AI models on the CNV of actionable genes was analyzed in NGS cases. The workflow diagram of this study is shown in Fig. 1.

MATERIALS AND METHODS

Patients with urinary tract cancer

It included patients with pathologically confirmed urinary tract malignancies treated at Asan Medical Center, Seoul, Republic of Korea with available clinical information and pathology materials, including H&E-stained slides and formalin-fixed, paraffin-embedded (FFPE) tissue blocks. Three cohorts were established: a developmental cohort, a validation cohort, and an application cohort. For the developmental cohort, 39 cases were selected from 322 cases of invasive high-grade urothelial carcinoma diagnosed between March 2022 and August 2022 to create cell patches for the training of CNN models. The validation cohort consisted of 119 NGS cases, with samples collected between May 2019 and February 2022, to validate the trained CNN models on cases similar to those in the clinical setting. The application cohort consisted of 41 NGS cases, with samples collected between March 2022 and August 2022, to evaluate the impact of AI-driven NCPs on the CNV of actionable genes identified by NGS analysis.

Tissue microarray construction

Tissue microarrays (TMAs) were generated in the validation cohort with 1 mm-diameter cores from 10% neutrally buffered FFPE tumor blocks using a tissue microarrayer (Quick-Ray, Unitma Co. Ltd., Seoul, Korea). To ensure that the TMA cores were representative of the validation cohort, three cores were collected from tumor areas that were representative of the histologic type and grade of each case, while attempting to avoid necrotic areas [7]. Different tumor locations (peripheral vs. central) were included, and an attempt was made to ensure that NCPs were evenly distributed by including tumor cells of different cell densities. To provide a negative control for AI-driven NCPs, areas without tumor cells were included.

Multiplex IF and multispectral imaging analysis

Four-micron-thick tissue sections were cut from the TMA construct; and then transferred onto plus-charged slides. mIF was performed using a Leica Bond Rx Automated Stainer (Leica Biosystems, Nussloch, Germany) and Opal Polaris 7-Color Automated immunohistochemistry (IHC) Detection Kit (Akoya Biosciences, Marlborough, MA, USA) as previously described [14]. After sequential reactions, the tissue sections were counterstained with 4',6-diamidino-2-phenylindole (DAPI) for nuclear staining (62248, Thermo Scientific, Waltham, MA, USA) and mounted with ProLong Gold antifade reagent (P36935, In-

https://doi.org/10.4132/jptm.2024.07.13

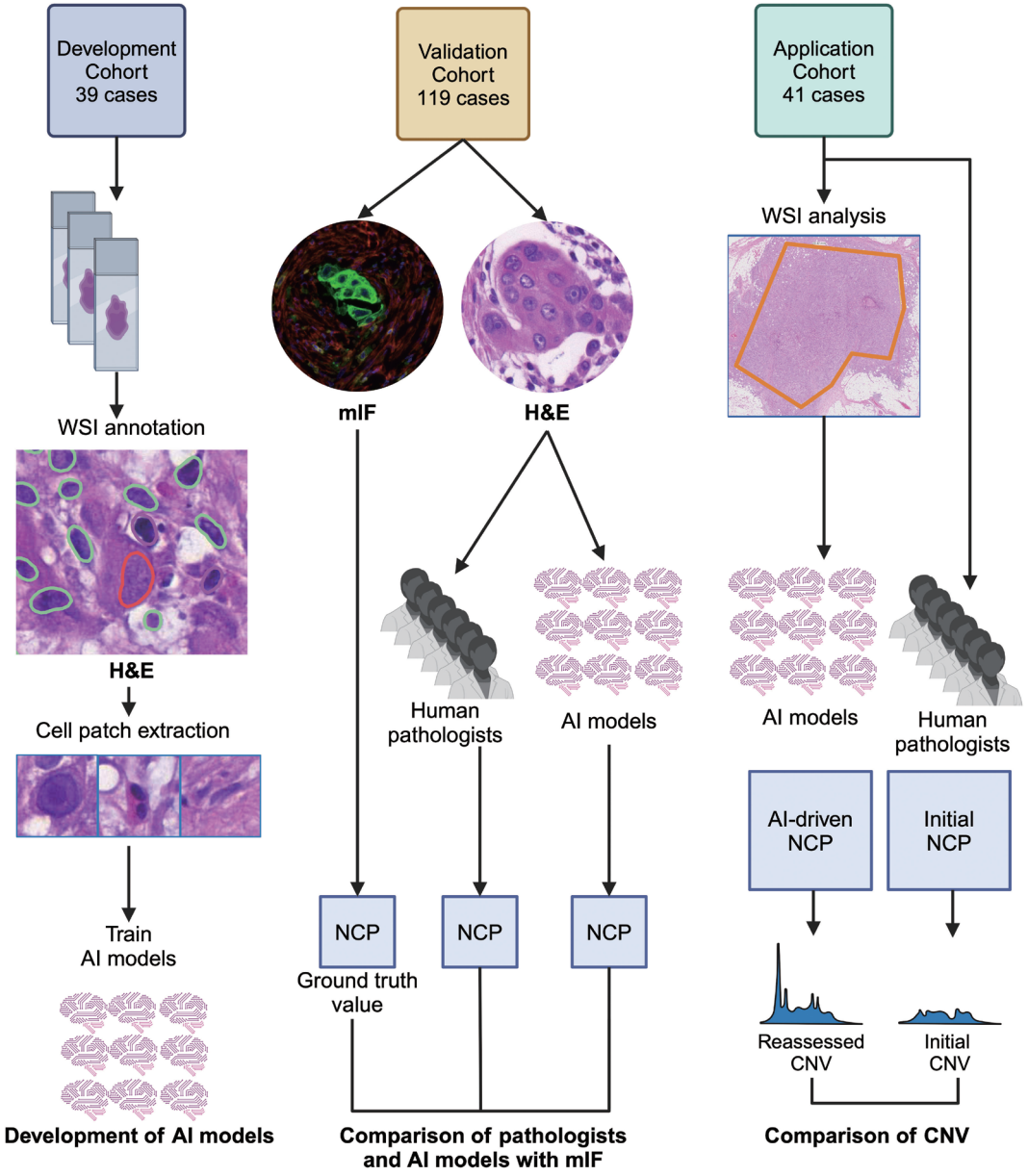

Fig. 1. Study overview. Artificial intelligence (AI) models were trained using cell patches extracted from the images of H&E slides of the developmental cohort. Using the validation cohort, the AI models and pathologists separately assessed neoplastic cell percentage (NCP) in the H&E images and their performances were assessed by comparing their estimates to the multiplex immunofluorescence (mIF)–driven estimates. The best AI model was applied to whole slide images (WSIs) of the application cohort to assess its impact on copy number variation (CNV). This figure was created with Biorender.com.

vitrogen, Carlsbad, CA, USA). The primary antibodies used in this study were CD45 (1:200, DAKO, Santa Clara, CA, USA) for immune cells, α-smooth muscle actin (SMA; 1:100, Zymed, San Francisco, CA, USA) for stromal cells, and pan-cytokeratin (CK; 1:300, Novus Biologicals, Littleton, CO, USA) for tumor cells with corresponding fluorophores for fluorescence signals Opal 570, Opal 690, and Opal 780, respectively. The multiplex-stained slides were scanned using a Vectra Polaris Automated Quantitative Pathology Imaging System (Akoya Biosciences), and the images were visualized with a Phenochart Whole Slide Viewer (Akoya Biosciences). Phenotyping of cellular components in the images was performed using inForm image analysis software and the phenoptr/phenoptrReports tissue analysis software packages (Akoya Biosciences). Based on the phenotyping, the mIF-driven NCP was calculated for each TMA core and used as the ground truth value.

Whole-slide scanning

H&E slides from the developmental and validation cohorts were scanned with a PANNORAMIC 250 Flash II scanner (3D HISTECH, Budapest, Hungary) at 40× magnification with 0.22 μm/pixel in a single layer. A Pathology Scanner SG300 (Philips, Best, The Netherlands) was used at 40× magnification with 0.25 μm/pixel in a single layer for the application cohort.

Cell patch generation for CNN model training

Scanned slides were assessed using open-source digital pathology software, QuPath v. 3.4.2 [15]. The representative regions of interest, at least one per slide in the developmental cohort, were drawn by one (J.J.) of the authors. Cell nuclei were detected with star-convex polygons using the provided QuPath plugin to avoid incomplete segmentation of overlapping nuclei [16]. The detected cells were then manually classified into three classes: tumor cells, stromal cells, or immune cells. For each detected cell, 100×100 pixel image patches were obtained with their class labels. The extracted cell patches of the three classes were divided into the training set, tuning set, and test set, at a 7:2:1 ratio.

CNN model training and performance metrics

Cell patches in the training and tuning sets were transformed into tensors and augmented by Pytorch library ver. 1.12.1 [17]. Cell patches were provided to nine open-source CNN models provided by Pytorch. The models were AlexNet with five convolutional layers and three fully connected layers [18], VGG with 16 convolutional layers and three fully connected layers [19], ResNet with deep convolutional networks (50 layers) and residual learning [20], WideResNet with three increased width residual networks [21], EfficientNet with scaling of depth, width, and resolution [22], EfficientNet V2 optimized with training-aware neural architecture search and scaling [23], MobileNet V2 with inverted residual blocks [24], MobileNet V3 improved with network architecture search and tuning [25], and ShuffleNet V2 focused on direct metrics such as speed [26]. The Adam optimizer was adopted with default hyperparameters ($\beta1 = 0.9$; $\beta2 = 0.999$; $\varepsilon = 1.0\times10^{-8}$) [27]. The Cross Entropy Loss function and Reduce LR On Plateau function were used as the loss function and learning rate scheduler, respectively. The batch size was set to 128 and the learning epoch was set to 80. The models were computed by two GPUs, RTX 3090 (NVIDIA, Santa Clara, CA, USA).

The performance of the trained models was evaluated in the predetermined test set with the following parameters: sensitivity, specificity, precision, accuracy, and F1 score.

Estimation of NCP by pathologists and AI models

In the validation cohort, six pathologists with varying levels of expertise estimated the NCP of each core using H&E-stained digital images of the TMA construct. The pathologists included one uropathologist (Y.M.C.), two fellows (S.U.J. and B.A.), and three residents (G.H.K., H.J.S., and Y.I.L.). They were instructed to estimate each individual TMA core by eyeball measurement, not by counting cells individually. They provided NCP estimates on a 5% scale, ranging from 0% to 100%.

To obtain AI-driven NCPs, the trained CNN models were applied on the H&E-stained digital images of the validation and application cohorts. The models classified the cells into three classes (tumor, stroma, or immune cells), and provided AI-driven NCP estimates of each TMA core in the validation cohort and each whole slide image in the application cohort.

Performance comparison of pathologists and AI models

The performance of pathologists and AI models in the validation cohort was evaluated by comparing them to mIF-driven NCP as the ground truth value using intraclass correlation coefficients (ICCs) with ICC (2,1) as an individual estimator [28]. The ICC was interpreted as poor (< 0.40), fair (0.40–0.59), good (0.60–0.74), and excellent (0.75–1.00) as previously proposed [29,30].

Selecting significant inter-rater variation in the NCP assessment

To identify TMA cores with significantly different NCP values between pathologists and AI models compared to the mIF, the mean absolute error (MAE) was calculated using the following formula for each TMA core in the validation cohort. The TMA cores with the top 20 MAE values for each group, pathologist and AI model, were selected for further analysis.

$$MAE = \sum_{i=1}^{n} \frac{|x_i - m|}{n}$$

(x_i, AI-driven NCP or pathologist NCP; m, mIF-driven NCP; n, number of estimations)

Copy number analysis

The NextSeq 550Dx Sequencing System (Illumina, San Diego, CA, USA) and DNA-based targeted gene panel (OncoPanel AMC v4.3 panel) were used for NGS analysis as described previously [31-33]. The panel consisted of approximately 1.2 Mbp with 33524 probes targeting 382 genes [31-33]. The tumor area was macrodissected from FFPE tissue blocks and used

https://doi.org/10.4132/jptm.2024.07.13

for DNA extraction. The copy number (CN) analysis was conducted using CNVkit's "batch" function [34]. The log2 ratio of the "cns" file in the analysis results had been utilized to calculate the estimated CN, using the NCP determined by a pathologist at initial diagnosis. The CN was re-evaluated by incorporating the AI-driven NCP.

The estimated CN was classified into three groups according to the Catalogue of Somatic Mutations in Cancer (COSMIC) [35]. The criteria for CNV were as follows: amplification, total CN≥5; loss, total CN≤0; neutral/minor alteration, total CN, 2–4 [36]. The impact of AI-driven NCP on CNV was assessed on the 166 actionable genes for solid tumors listed at OncoKB, regardless of cancer type and level of evidence [37].

RESULTS

Patient cohorts

In the developmental cohort, 39 cases were selected to include various subtypes, divergent differentiations, image artifacts, and commonly encountered specimen types for the training of CNN models on various pathologic features of urothelial carcinoma (Supplementary Table S1) [38]. Twenty-seven cases were pure invasive urothelial carcinoma. The remaining cases showed various histologic features, either single or in combination and included squamous (5 cases), sarcomatoid (3 cases), glandular (2 cases), small cell neuroendocrine (2 cases), microcystic (1 case), poorly differentiated (1 case), and micropapillary (2 cases) features (Table 1).

In the validation cohort, in addition to 113 cases of invasive high-grade urothelial carcinoma, it contained collecting duct carcinoma (2 cases), urachal adenocarcinoma (2 cases), invasive squamous cell carcinoma (1 case), and non-invasive low-grade papillary urothelial carcinoma (1 case). Fifty-seven cases of urothelial carcinoma were pure form and the others revealed various histologic features either isolated or in combination, including squamous (26 cases), micropapillary (24 cases), sarcomatoid (8 cases), nested (4 cases), giant cell (3 cases), glandular (2 cases), plasmacytoid (2 cases), and microcystic (2 cases) features (Table 1).

In the application cohort, 21 cases were pure invasive urothelial carcinoma and the remaining revealed squamous (8 cases), micropapillary (4 cases), sarcomatoid (3 cases), plasmacytoid (2 cases), small cell neuroendocrine (2 cases), giant cell (1 case) features, either single or in combination (Table 1).

Development of CNN models and their performance

In the development cohort, a total of 291 regions of interest (median, 6; range, 1 to 22 per case) were selected, attempting to include various histologic features of urothelial carcinoma. A total of 133,941 cell patches were extracted, consisting of 76,330 tumor cell patches, 24,297 stromal cell patches, and 33,314 immune cell patches (Fig. 2). The image patches in the training and tuning sets were converted into tensors and subjected to augmentation techniques such as random flipping, rotation, and padding to increase the diversity of the images for the generalization of the CNN models (Supplementary Fig. S1). These augmented patches were then fed into the nine CNN models to train them

Table 1. Clinicopathologic characteristics of the study cohorts

Variable	Developmental cohort (n=39)	Validation cohort (n=119)	Application cohort (n=41)
Sex			
Male	30 (76.9)	91 (76.5)	30 (73.2)
Female	9 (23.1)	28 (23.5)	11 (26.8)
Age (yr)	72 (43–97)	67.5 (35–90)	68 (43–86)
Tumor location			
Urinary bladder	29 (74.4)	52 (43.7)	20 (48.8)
Renal pelvis	4 (10.3)	19 (16.0)	11 (26.8)
Ureter	6 (15.4)	33 (27.7)	8 (19.5)
Others[a]	0	15 (12.6)	2 (4.9)
Procedure			
Transurethral resection	26 (66.7)	23 (19.3)	10 (24.4)
Curative surgery[b]	13 (33.3)	86 (72.3)	23 (56.1)
Endoscopic biopsy	0	1 (0.8)	8 (19.5)
Metastatectomy[c]	0	9 (7.6)	0
2022 WHO grade			
Low	0	1 (0.8)	0
High	39 (100)	113 (95.0)	41 (100)
Histologic variation			
None (pure form)	27 (62.8)	57 (47.9)	21 (50)
Squamous	5 (11.6)	26 (21.8)	8 (19.0)
Sarcomatoid	3 (7.0)	8 (6.7)	3 (7.1)
Glandular	2 (4.7)	2 (1.7)	0
Small cell	2 (4.7)	0	2 (4.8)
Micropapillary	2 (4.7)	24 (20.2)	4 (9.5)
Poorly differentiated	1 (2.3)	0	0
Microcystic	1 (2.3)	2 (1.7)	0
Others[d]	0	9 (7.6)	4 (9.5)
Nonurothelial[e]	0	5 (4.2)	0

Values are presented as median (range) or number (%).
WHO, World Health Organization.
[a]This category includes urethra, regional lymph node, distant organ metastasis, and kidney (for collecting duct carcinoma); [b]Curative surgery includes radical cystectomy, nephroureterectomy, distal ureterectomy, and partial cystectomy specimens; [c]Metastectomy sites are lymph nodes, peritoneum, adrenal gland, and lung; [d]In the validation cohort, invasive urothelial carcinoma with nested (4 cases), giant cell (3 cases), and plasmacytoid (2 cases) features were included. In the application cohort, plasmacytoid (3 cases) and giant cell (1 case) features were included; [e]Non-urothelial carcinoma includes collecting duct carcinoma, urachal adenocarcinoma, and pure squamous cell carcinoma cases.

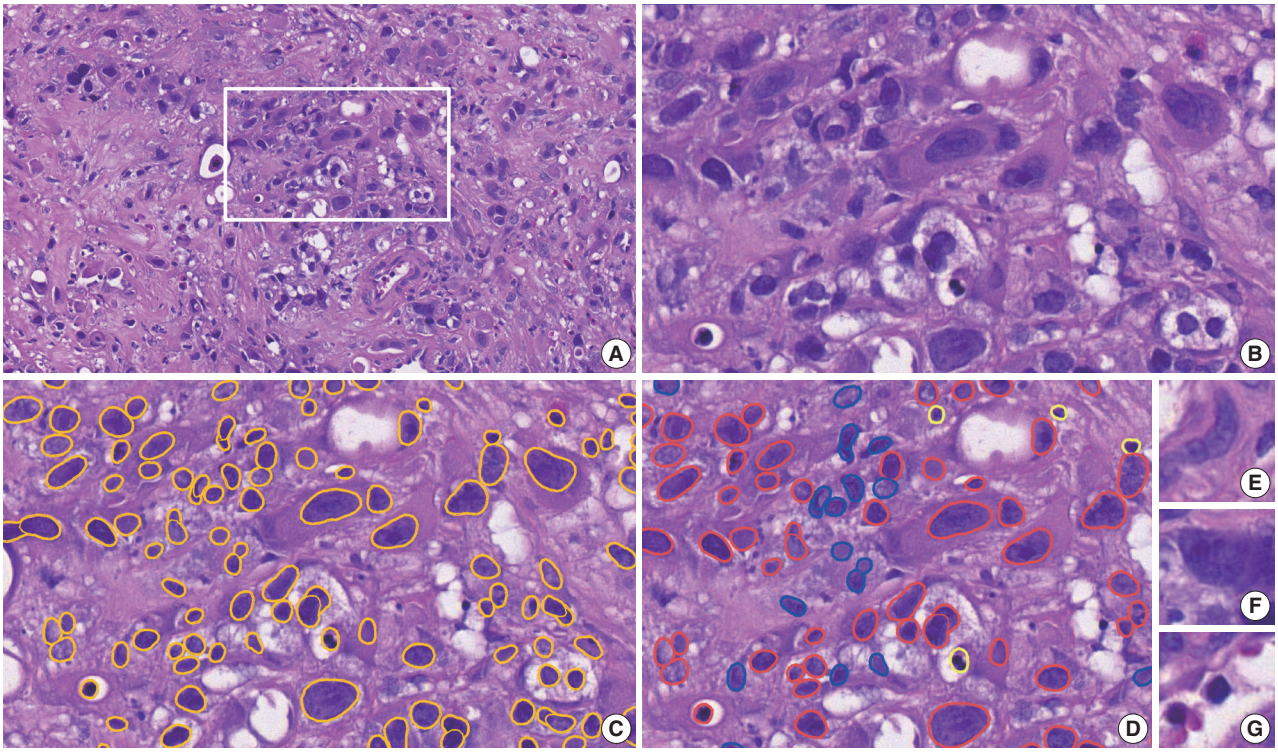

Fig. 2. Cell patch generation in the developmental cohort. (A) A region of interest (ROI) is manually selected in each digitally scanned whole H&E slide image. (B–D) On the high-magnification view of an ROI (B), nuclei are segmented by a yellow outline (C), then they are manually classified into tumor cells in red, stromal cells in blue, and immune cells in bright yellow (D). (E–G) Examples of extracted 100×100-pixel image patches: (E) a stromal cell, (F) a tumor cell, and (G) an immune cell.

to classify cell patches into the three specified classes.

When the model performance was evaluated at the patch level using the test set, EfficientNet showed the highest sensitivity (0.94) and accuracy (0.87). AlexNet and VGG demonstrated low accuracy (0.55, each) and therefore were excluded from further analysis (Table 2).

Table 2. Performance metrics of the nine CNN models in the development cohort

Model	Sensitivity	Specificity	Precision	Accuracy	F1-score
AlexNet	1.0	0.0	0.55	0.55	0.71
VGG	1.0	0.0	0.55	0.55	0.71
EfficientNet	0.94	0.88	0.90	0.87	0.92
EfficientNet V2	0.93	0.87	0.90	0.86	0.91
MobileNet V2	0.92	0.86	0.89	0.85	0.90
MobileNet V3	0.92	0.86	0.89	0.86	0.90
ResNet	0.92	0.88	0.90	0.86	0.91
WideResNet	0.92	0.89	0.91	0.86	0.91
ShuffleNet V2	0.93	0.87	0.89	0.86	0.91

CNN, convolutional neural network.

Calculation of mIF-driven NCP as the ground truth value

In the TMA construct generated from the validation cohort, 335 cores were available for mIF staining of pan-cytokeratin, CD45, and SMA (Fig. 3). The proportion of cells with a single immunophenotype, positive for only one marker, was 89.4%. The most common double-positive immunophenotype was double-positivity for CD45 and SMA, accounting for 6.9% of the total cell count. This was followed by double-positivity for CK and SMA, accounting for 0.4% of the total cell count (Supplementary Table S2). Since only tumor cells were used to estimate NCP, not immune and stromal cells, it was calculated by dividing the number of cytokeratin-positive tumor cells by the total number of DAPI-positive cells. The median NCP of the TMA cores was 51% (range, 0% to 99%) (Supplementary Fig. S2). Fifteen cores contained no tumor cells and 71 cores contained an NCP less than 20%, which is the cutoff value generally considered adequate for reliable mutation detection in NGS testing. There were no significant differences in the mIF-driven NCP estimates between tumor locations, procedures, or histology subtypes (data not shown).

https://doi.org/10.4132/jptm.2024.07.13

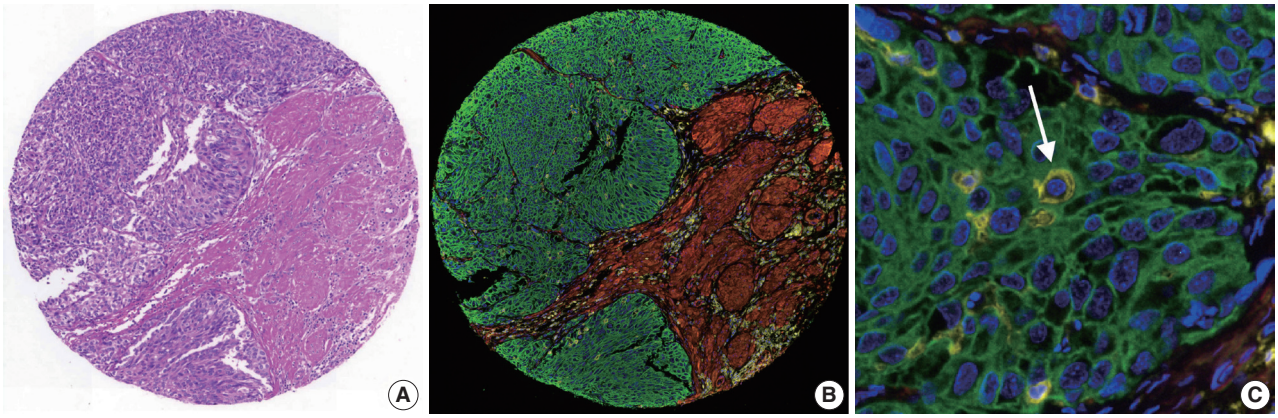

Fig. 3. Multiplex immunofluorescence (mIF). (A) Images of the H&E staining and (B) the corresponding mIF staining of a representative tissue microarray core from the validation cohort. (C) In the high-magnification view of (B), intratumoral lymphocytes are highlighted (arrow). (B, C) Blue, DAPI; green, pan-cytokeratin; red, α-smooth muscle actin; yellow, CD45.

Assessment of NCP by pathologists and AI models with comparison to mIF-driven NCP

The pathologists estimated the NCP of the TMA cores from the validation cohort with excellent reliability. The ICC values were within a range of 0.78 to 0.91, with the uropathologist estimating NCP with the highest reliability, 0.91 (95% confidence interval [CI], 0.89 to 0.93) (Table 3).

AI models also estimated NCP with excellent reliability, with ICCs ranging from 0.83 to 0.88. The most reliable model was EfficientNet with an ICC of 0.88 (95% CI, 0.78 to 0.92) (Table 3). MobileNet V3 showed the lowest agreement with the mIF-driven NCP with an ICC of 0.82 (95% CI, 0.7 to 0.88) (Table 3).

Performance comparison between AI models and pathologists

In general, the AI models showed a higher level of agreement with the mIF-driven NCP than did the pathologists, although the one uropathologist had the highest agreement of all raters. Even the lowest AI model, MobileNet V3, had a higher or similar level of agreement than all but one of the pathologists (Table 3). When the distribution of NCP estimates by the six individual pathologists and seven AI models were assessed for each TMA core, pathologists' NCP estimates were more variable in each range of NCP than AI-driven NCP estimates. However, the AI models tended to underestimate NCP when the mIF estimates were greater than 60% (Supplementary Fig. S3). They often misclassified neoplastic cells as stromal or immune cells when their nuclei became spindle-shaped or pyknotic due to degeneration, detachment from the epithelium, cauterization, and/or abundant cytoplasm. (Supplementary Table S3, Supplementary Fig. S4).

Table 3. Agreement between pathologist and AI-driven NCP on mIF-driven NCP in the validation cohort

Rater	ICC	95% CI
Pathologist		
Uropathologist	0.91	0.89–0.93
Fellow 1	0.80	0.53–0.89
Fellow 2	0.82	0.78–0.85
Resident 1	0.78	0.72–0.83
Resident 2	0.82	0.78–0.85
Resident 3	0.81	0.73–0.86
AI models		
EfficientNet	0.88	0.78–0.92
EfficientNet V2	0.87	0.84–0.89
MobileNet V2	0.87	0.85–0.90
MobileNet V3	0.82	0.70–0.88
ResNet	0.86	0.76–0.91
WideResNet	0.85	0.80–0.88
ShuffleNet V2	0.83	0.74–0.88

AI, artificial intelligence; NCP, neoplastic cell percentage; mIF, multiplex immunofluorescence; ICC, intraclass correlation coefficient; CI, confidence interval.

Performance comparison between AI models and pathologists according to histological variation

To evaluate the accuracy of NCP assessment according to histological variation, we divided the validation cohort into three groups: the pure form of urothelial carcinoma without divergent differentiation/subtype, urothelial carcinoma with divergent differentiation/subtype, and non-urothelial carcinoma, which included squamous cell carcinoma and urachal adenocarcinoma. The performance was measured against mIF-driven NCP (Supplementary Table S4).

The estimation of NCP by pathologists was excellent with and without divergent differentiation/subtype (minimum ICC, 0.76 and 0.82, respectively), but the performance was decreased

in non-urothelial carcinoma (minimum ICC, 0.61). The AI models demonstrated better or similar performance than the pathologists in cases of urothelial carcinoma, both with and without divergent differentiation/subtype (minimum ICC, 0.87 and 0.81, respectively). However, the performance of the AI models was markedly decreased in non-urothelial carcinoma cases, showing lower agreement (minimum ICC, 0.33) with mIF-driven NCP than those of pathologists (Supplementary Table S4).

Analysis of highly discrepant cases in NCP estimation

The top 20 TMA cores with high disagreement among pathologists showed abundant stroma (n = 5), large tumor cells with abundant cytoplasm (n = 4), cauterization artifact (n = 2), dense infiltration of inflammatory cells (n = 2), keratinization (n = 1), and mucinous histology (n = 1). Inaccurate assessment of mIF-driven NCP also resulted in high inter-pathologist discrepancies and was noted in cores with suboptimal cytokeratin staining (n = 3), degeneration (n = 1), and normal lung tissue (n = 1).

The top 20 TMA cores with high disagreement among the AI-models was noted in cores with cauterization (n = 5), abundant stroma (n = 3), spindling of tumor nuclei (n = 3), dense infiltration of inflammatory cells (n = 2), mucinous histology (n = 2), hypocellular stroma (n = 1), keratinization (n = 1), and abundant cytoplasm of tumor cells (n = 1). Inaccurate assessment of mIF-driven NCP was also noted in cores with suboptimal cytokeratin staining (n = 2) (Fig. 4).

Impact of AI-driven NCP estimation on CNV

In the application cohort, a total of 785 CNVs (median, 16; range 1 to 120 per case) were reported at initial diagnosis with 173 amplifications (22.0%), 77 losses (9.8%), and 535 neutral/minor alterations (68.2%).

AI-driven NCP was assessed using EfficientNet, which had the highest correlation with mIF. After applying the AI-driven NCP, 595 CNVs (75.8%) remained in the original groups and 190 (24.2%) were reclassified, resulting in 200 amplifications (25.5%), 80 losses (10.2%), and 505 neutral/minor alterations (64.3%). The 190 CNVs were reclassified into 66 amplifications (8.4%), 46 losses (5.9%), and 78 neutral/minor alterations (9.9%). Of note, 108 neutral/minor alterations (13.8%) at initial diagnosis were reclassified into either amplification (n = 64, 8.2%) or loss (n = 44, 5.6%) with the AI-driven NCPs, while neutral/minor alterations were reduced by 5.6%. Among the 77 CN losses at initial diagnosis, 41 (53.2%) were reclassified into neutral/minor alterations (Fig. 5, Supplementary Fig. S5).

Among the reclassified 190 CNVs, 55 CNVs belonged to actionable genes with 16 CNVs reclassified to amplification from loss or neutral/minor alteration and 16 CNVs reclassified to loss from amplification or neutral/minor alteration. The genes of 16 CNVs had therapeutic drugs associated with the corresponding CNV.

DISCUSSION

Here we report that AI models for NCP estimation in urinary tract cancer could be developed using open-source CNN models. The performance of the AI models was comparable to or better than that of pathologists. The application of the AI models reclassified a significant proportion of CNVs, with an increase of CN amplifications and losses and a decrease in neutral/minor CN alterations. In addition, we showed that mIF staining could be used to calculate NCP as a ground truth value for the development of AI models.

Since the estimation of NCP is critical for accurate interpretation of NGS results, which are important for treatment decision making, it has been recommended that NCP estimation should be performed by the pathologist evaluating the case by selecting the area with the highest density of viable neoplastic cells and avoiding areas with inflammatory cells, necrosis, desmoplastic stroma, and mucus [7]. Since there is significant inter-pathologist variation in NCP estimates [39], innovative techniques such as in silico analysis and digital estimation have been developed to overcome this issue. However, in order to develop new technologies, accurate NCPs must be available for use as a ground truth value, but obtaining this ground truth value has been a challenge. There has been limited study using mIF to obtain ground truth values, while IHC was used to create a ground truth value generated by manual annotation of tumor cells with reference to immunostained slides with thyroid transcription factor-1and napsin A for NCP in lung cancer [40].

Our study applied mIF as a new method for calculating NCP and used the mIF-driven estimates as a ground truth value, which is generally reliable but needs improvement. The cytoplasm stained for cytokeratin in tumor cells and CD45 in immune cells circumferentially surrounded the nuclei, so tumor cells and immune cells were easily immunophenotyped, but SMA staining was difficult to evaluate because the cell shapes were elongated and curved. Occasionally, cytoplasm outside the cross-section containing the nucleus interspersed between other cell types may appear as double/triple positive cells. In addition, cell types that cannot be defined by the three antibody types, such as neuronal cells, may be counted as unphenotyped cells.

https://doi.org/10.4132/jptm.2024.07.13

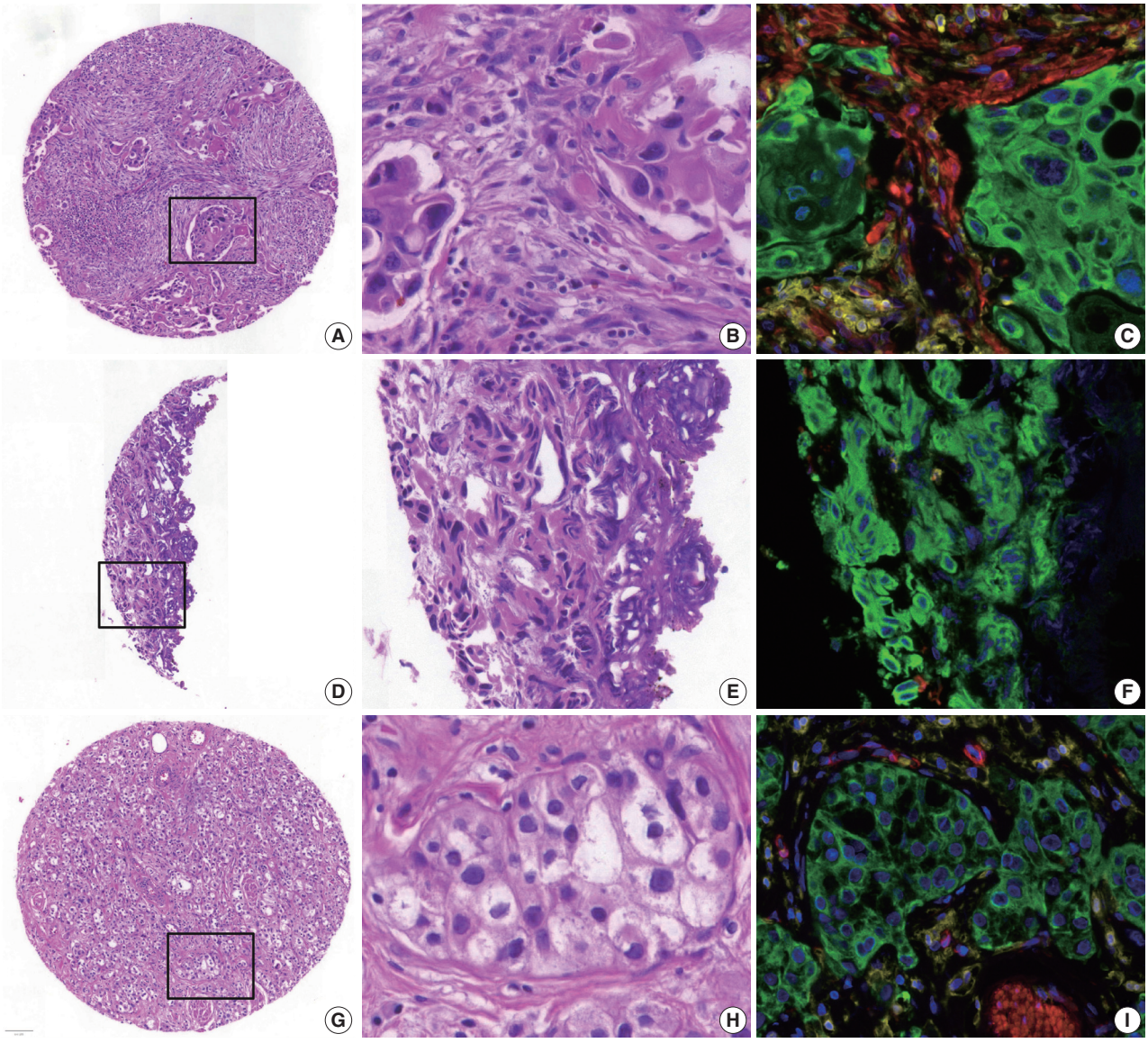

Fig. 4. Examples of high mean absolute error cores for neoplastic cell percentage (NCP) estimation. (A–C) Abundant stroma (multiplex immunofluorescence [mIF], 28%; pathologist NCP, 5%–30%; artificial intelligence [AI] models, 23%–44%). (D–F) Cauterization artifact (mIF, 98%; pathologists, 0%–80%; AI models, 51%–76%). (G–I) Abundant cytoplasm in tumor cells (mIF, 43%; pathologists, 65%–90%; AI models, 33%–49%). B, E, and H are high-magnification images of the square inset area in A, D, and G, respectively, and the corresponding mIF images are C, F, and I, respectively. (C, F, I) Blue, DAPI; green, pan-cytokeratin; red, α-smooth muscle actin; yellow, CD45.

Nevertheless, the unphenotyped mesenchymal cells and double-positive cells for CD45 and αSMA did not affect NCP estimation because only cytokeratin-positive tumor cells among the total DAPI-positive nuclei were calculated for NCP estimation. The CK and SMA double-positive cells, which may represent myofibroblasts, were low at 0.4% of the total cell count with an insignificant impact on NCP. Suboptimal cytokeratin staining was noted in few TMA cores and resulted in inaccurate estimates of mIF-driven NCP, which needs to be improved by further development of the mIF technique and image analysis software. In addition, NCP assessment should be performed on a well-preserved representative viable tumor area, avoiding tissue degeneration and cauterization artifacts.

After applying the AI-driven estimates in the application cohort, a significant proportion of cases were recategorized to have amplification or loss of CN on actionable target genes with a decrease of neutral/minor CN alteration, which would affect decision making for targeted drugs. It is worth noting that the majority of the CN loss at initial diagnosis was reclassified into the neutral/minor CN alteration group after applying AI-driven

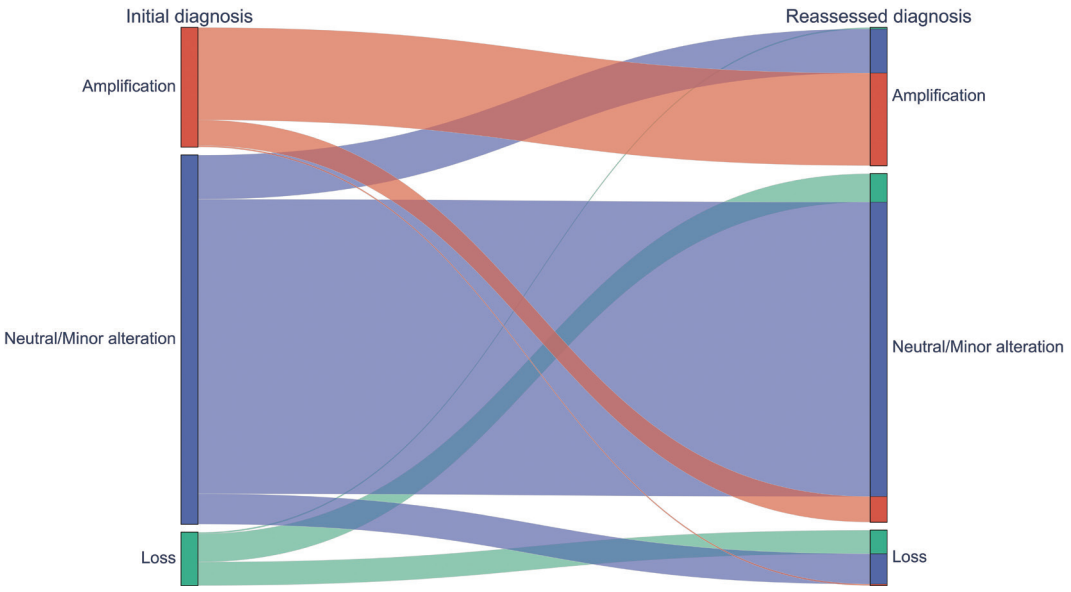

Fig. 5. A Sankey diagram showing the copy number variation of the initial diagnosis (left) and that after incorporation of artificial intelligence–driven neoplastic cell percentage (right).

NCP estimates, implying that assigning CN loss should be cautious during CNV interpretation.

As previously pointed out, a wide range of inter-pathologist variation was observed for samples with dense or scattered lymphocytic infiltrates or with mucinous stroma [39]. In addition, this study demonstrates that abundant stroma, cauterization and/or crush artifacts, and tumor cells with non-classic morphology, such as abundant cytoplasm and histologic subtypes, may lead to an inaccurate estimation of NCP and should be carefully evaluated.

Although the AI models were developed using limited training data from the developmental cohort, they provided reliable estimates of NCP in the validation cohort with a larger number of cases and a more diverse range of histological features. The AI model could also be applied to the digital images with variations in the quality of H&E slides scanned by different whole slide image scanners in the application cohort. The developmental cohort consisted of invasive urothelial carcinoma cases and the AI models were not specifically trained on non-urothelial carcinoma cases such as mucinous adenocarcinoma. Nevertheless, the AI models showed fair to good reliability, although their performance was significantly reduced compared to urothelial carcinoma cases. This suggests that the models have a degree of generalizability across diverse tumor morphologies of urinary cancers. However, it is also worth noting that the AI model underestimated NCP in cases with a higher NCP, indicating a need for further improvement of the model, especially when tumor tissues contained cauterization artifacts, or neoplastic cells with spindled or pyknotic nuclei, or abundant cytoplasm. The AI models could be improved if they were been trained on a dataset containing more of these features. While the performance of older AI models such as AlexNet and VGG was less satisfactory in classifying tumor cell patches, newer AI models with various levels of computational resources and cognitive abilities performed similarly, with accuracies above 0.85, and none of them showed a particularly superior performance.

This present study was associated with limitations, including its retrospective design and nature as a single-center study with a small number of cases. The uropathologist evaluation was excellent, but it is hard to generalize because it was only one person. In the future, these AI models need to be validated by a prospective multicenter study with a larger number of cases and participating pathologists. Further advances in mIF technology and in computational pathology will continue to increase the accuracy of AI models.

Supplementary Information

The Data Supplement is available with this article at https://doi.org/10.4132/jptm.2024.07.13.

Ethics Statement

The Institutional Review Board of the Asan Medical Center, Republic of Korea (#2022-1558) approved this study. All of the clinical investigations were conducted in line with the principles of the Declaration of Helsinki. Formal written informed consent was not required with a waiver by the appropriate IRB research ethics committee.

Availability of Data and Material

All raw data are available for researchers who reasonably request them from the corresponding author with approval of the institutional review boards.

Code Availability

Not applicable.

ORCID

Jinahn Jeong	https://orcid.org/0000-0002-0461-1904
Deokhoon Kim	https://orcid.org/0000-0002-3597-1048
Yeon-Mi Ryu	https://orcid.org/0009-0008-9359-5790
Ja-Min Park	https://orcid.org/0000-0002-4799-1599
Sun Young Yoon	https://orcid.org/0000-0001-7498-9497
Bokyung Ahn	https://orcid.org/0000-0002-0229-2276
Gi Hwan Kim	https://orcid.org/0000-0001-6228-764X
Se Un Jeong	https://orcid.org/0000-0001-8399-5792
Hyun-Jung Sung	https://orcid.org/0000-0002-8791-5945
Yong Il Lee	https://orcid.org/0009-0007-6126-9512
Sang-Yeob Kim	https://orcid.org/0000-0002-3724-256X
Yong Mee Cho	https://orcid.org/0000-0001-8766-2602

Author Contributions

Conceptualization: JJ, YMC. Formal analysis: JJ. Funding Acquisition: YMC. Methodology: JJ, DK. Resources: YMR, SYK, BA, GHK, SUJ, HJS, YIL, JMP, SYY. Supervision: YMC. Visualization: JJ. Writing—original draft preparation: JJ. Writing—review & editing: YMC. Approval of final manuscript: all authors.

Conflicts of Interest

The authors declare that they have no potential conflicts of interest.

Funding Statement

This study was supported by the Ministry of Science, ICT and Future Planning (2019R1A2C1088246) and a grant (2023IP0052-1) from the Asan Institute for Life Sciences, Asan Medical Center, Seoul, Republic of Korea.

References

1. Robertson AG, Kim J, Al-Ahmadie H, et al. Comprehensive molecular characterization of muscle-invasive bladder cancer. Cell 2018; 174: 1033.
2. Loriot Y, Necchi A, Park SH, et al. Erdafitinib in locally advanced or metastatic urothelial carcinoma. N Engl J Med 2019; 381: 338-48.
3. Sheng X, Yan X, Wang L, et al. Open-label, multicenter, phase II study of RC48-ADC, a HER2-targeting antibody-drug conjugate, in patients with locally advanced or metastatic urothelial carcinoma. Clin Cancer Res 2021; 27: 43-51.
4. Patelli G, Zeppellini A, Spina F, et al. The evolving panorama of HER2-targeted treatments in metastatic urothelial cancer: a systematic review and future perspectives. Cancer Treat Rev 2022; 104: 102351.
5. Zare F, Dow M, Monteleone N, Hosny A, Nabavi S. An evaluation of copy number variation detection tools for cancer using whole exome sequencing data. BMC Bioinformatics 2017; 18: 286.
6. Smits AJ, Kummer JA, de Bruin PC, et al. The estimation of tumor cell percentage for molecular testing by pathologists is not accurate. Mod Pathol 2014; 27: 168-74.
7. Dufraing K, van Krieken JH, De Hertogh G, et al. Neoplastic cell percentage estimation in tissue samples for molecular oncology: recommendations from a modified Delphi study. Histopathology 2019; 75: 312-9.
8. Haider S, Tyekucheva S, Prandi D, et al. Systematic assessment of tumor purity and its clinical implications. JCO Precis Oncol 2020; 4: PO.20.00016.
9. Yadav VK, De S. An assessment of computational methods for estimating purity and clonality using genomic data derived from heterogeneous tumor tissue samples. Brief Bioinform 2015; 16: 232-41.
10. Baxi V, Edwards R, Montalto M, Saha S. Digital pathology and artificial intelligence in translational medicine and clinical practice. Mod Pathol 2022; 35: 23-32.
11. Azimi V, Chang YH, Thibault G, et al. Breast cancer histopathology image analysis pipeline for tumor purity estimation. Proc IEEE Int Symp Biomed Imaging 2017; 2017: 1137-40.
12. Lin S, Samsoondar JP, Bandari E, et al. Digital quantification of tumor cellularity as a novel prognostic feature of non-small cell lung carcinoma. Mod Pathol 2023; 36: 100055.
13. Amin MB. Histological variants of urothelial carcinoma: diagnostic, therapeutic and prognostic implications. Mod Pathol 2009; 22 Suppl 2: S96-118.
14. Ahn J, Jin M, Song E, et al. Immune profiling of advanced thyroid cancers using fluorescent multiplex immunohistochemistry. Thyroid 2021; 31: 61-7.
15. Bankhead P, Loughrey MB, Fernandez JA, et al. QuPath: open source software for digital pathology image analysis. Sci Rep 2017; 7: 16878.
16. Schmidt U, Weigert M, Broaddus C, Myers G. Cell detection with star-convex polygons. In: Medical Image Computing and Computer Assisted Intervention - MICCAI 2018, Lecture Notes in Computer Science, Vol. 11071; 2018 Sep 16-20; Granada, Spain.
17. Paszke A, Gross S, Massa F, et al. Pytorch: an imperative style, high-performance deep learning library. In: Advances in Neural Information Processing Systems 32, NeurIPS 2019; 2019 Dec 8-14; Vancouver, BC, Canada.
18. Krizhevsky A, Sutskever I, Hinton GE. ImageNet classification with deep convolutional neural networks. In: Proceedings of the 25th International Conference on Neural Information Processing Systems, Vol. 1; 2012 Dec 3-6; Lake Tahoe, Nevada, CA, USA.
19. Simonyan K, Zisserman A. Very deep convolutional networks for large-scale image recognition. Preprint arXiv at: https://doi.org/10.48550/arXiv.1409.1556 (2014).
20. He K, Zhang X, Ren S, Sun J. Deep residual learning for image recognition. In: 2016 IEEE Conference on Computer Vision and Pattern Recognition (CVPR); 2016 Jun 27-30; Las Vegas, NV, USA.
21. Zagoruyko S, Komodakis N. Wide residual networks. Preprint arXiv at: https://doi.org/10.48550/arXiv.1605.07146 (2016).
22. Tan M, Le Q. EfficientNet: rethinking model scaling for convolutional neural networks. In: Proceedings of the 36th International Conference on Machine Learning (PMLR); 2019 Jun 9-15; Long Beach, CA, USA.
23. Tan M, Le Q. Efficientnetv2: smaller models and faster training. In: Proceedings of the 38th International Conference on Machine Learning (PMLR); 2021 Jul 18-24; Virtual Event.
24. Sandler M, Howard A, Zhu M, Zhmoginov A, Chen LC. Mobilenetv2: inverted residuals and linear bottlenecks. In: Proceedings of the IEEE/CVF Conference on Computer Vision and Pattern Recognition; 2018 Jun 18-23; Salt Lake City, UT, USA.
25. Howard A, Sandler M, Chen B, et al. Searching for MobileNetV3.

In: Proceedings of the IEEE/CVF International Conference on Computer Vision; 2019 Oct 27-Nov 2; Seoul, Korea.
26. Ma N, Zhang X, Zheng HT, Sun J. Shufflenet v2: practical guidelines for efficient CNN architecture design. In: Proceedings of the European Conference on Computer Vision (ECCV 2018); 2018 Sep 8-14; Munich, Germany.
27. Kingma DP, Ba J. Adam: a method for stochastic optimization. Preprint arXiv at: https://doi.org/10.48550/arXiv.1412.6980 (2014).
28. Shrout PE, Fleiss JL. Intraclass correlations: uses in assessing rater reliability. Psychol Bull 1979; 86: 420-8.
29. Robert ME, Ruschoff J, Jasani B, et al. High interobserver variability among pathologists using combined positive score to evaluate PD-L1 expression in gastric, gastroesophageal junction, and esophageal adenocarcinoma. Mod Pathol 2023; 36: 100154.
30. Cicchetti DV. Guidelines, criteria, and rules of thumb for evaluating normed and standardized assessment instruments in psychology. Psychol Assess 1994; 6: 284-90.
31. Kim JE, Chun SM, Hong YS, et al. Mutation burden and I index for detection of microsatellite instability in colorectal cancer by targeted next-generation sequencing. J Mol Diagn 2019; 21: 241-50.
32. Kim M, Lee C, Hong J, et al. Validation and clinical application of ONCOaccuPanel for targeted next-generation sequencing of solid tumors. Cancer Res Treat 2023; 55: 429-41.
33. Oh JH, Sung CO, Kim HD, Chun SM, Kim J. *BRCA*-mutated gastric adenocarcinomas are associated with chromosomal instability and responsiveness to platinum-based chemotherapy. J Pathol Transl Med 2023; 57: 323-31.
34. Talevich E, Shain AH, Botton T, Bastian BC. CNVkit: genome-wide copy number detection and visualization from targeted DNA sequencing. PLoS Comput Biol 2016; 12: e1004873.
35. Tate JG, Bamford S, Jubb HC, et al. COSMIC: the catalogue of somatic mutations In cancer. Nucleic Acids Res 2019; 47: D941-7.
36. Zhao M, Zhao Z. Concordance of copy number loss and down-regulation of tumor suppressor genes: a pan-cancer study. BMC Genomics 2016; 17 Suppl 7: 532.
37. Suehnholz SP, Nissan MH, Zhang H, et al. Quantifying the expanding landscape of clinical actionability for patients with cancer. Cancer Discov 2024; 14: 49-65.
38. Homeyer A, Geissler C, Schwen LO, et al. Recommendations on compiling test datasets for evaluating artificial intelligence solutions in pathology. Mod Pathol 2022; 35: 1759-69.
39. Lhermitte B, Egele C, Weingertner N, et al. Adequately defining tumor cell proportion in tissue samples for molecular testing improves interobserver reproducibility of its assessment. Virchows Arch 2017; 470: 21-7.
40. Sakamoto T, Furukawa T, Pham HH, et al. A collaborative workflow between pathologists and deep learning for the evaluation of tumour cellularity in lung adenocarcinoma. Histopathology 2022; 81: 758-69.

Supplementary Table S1. A checklist for generating cell patches in order to include various histologic features of urinary tract cancer in the developmental cohort

Tissue condition
1. Fixation
Well-fixed
Poorly-fixed
2. Cauterization effect
Present
Absent
3. Focusing
Well-focused
Partially focused out
4. Tissue section thickness
Thick
Thin
5. Tearing
Present
Absent
6. Background
Clear
Hemorrhagic
Degenerative
Necrotic
7. Location
In tissue
Floating in the background
8. Cellularity
High
Low
Cancer cells
1. Cell shape
Round to ovoid
Polygonal
Spindle
2. Cohesiveness
Cohesive
Overlapping
Poorly cohesive
3. Cell membrane
Distinct
Indistinct
4. Mitosis
Present
Absent
5. Nucleoli
Prominent
Inconspicuous
6. Chromatin
Fine
Coarse
Vesicular

7. Cytoplasmic hue
Eosinophilic
Amphophilic
Basophilic
Clear
8. Cytoplasm amount
Abundant
Moderate
Scant
Mesenchyme
1. Location
Intra-tumoral
Peri-tumoral
Extra-tumoral
2. Structure
Adipose tissue
Muscularis propria
Muscularis mucosae
Large vessel
Small vessel
Papillary core
Nerve
Granulation tissue
3. Reaction
Desmoplastic
Hyalinized
Myxoid
Edematous
Immune cells
1. Location
Intra-tumoral
Peri-tumoral
Extra-tumoral
2. Structure
Aggregated
Follicle
3. Cell type
Neutrophil
Eosinophil
Mature lymphocyte
Histiocyte

Supplementary Table S2. Total immunophenotyped cells by mIF

Immunophenotype	Cell counts	Percentage (%)
CK+/CD45–/aSMA–	863,531	40.7
CK–/CD45+/aSMA–	577,724	27.2
CK–/CD45-/aSMA+	455,225	21.5
CK+/CD45+/aSMA–	20,299	1.0
CK+/CD45+/aSMA+	56	0.0
CK+/CD45-/aSMA+	9,035	0.4
CK–/CD45+/aSMA+	145,584	6.9
CK–/CD45–/aSMA–	48,559	2.3
Total	2,120,013	100

mIF, multiplex immunofluorescence; CK, cytokeratin; SMA, smooth muscle actin.

Supplementary Table S3. Possible causes of underestimation of the AI Models in TMA cores with a high NCP (≥ 60%)

Possible causes	Core counts	Percentage (%)
Nuclear spindling	27	19.9
Nuclear degeneration (pyknosis)	22	16.2
Abundant cytoplasm	6	4.4
Mixed[a]	4	2.9
Cauterization	3	2.2
Unremarkable	74	54.4
Total	136	100

AI, artificial intelligence; TMA, tissue microarrays; NCP, neoplastic cell percentage.

[a]Three cores showed both features of nuclear degeneration (pyknosis) and spindling. One core showed both features of abundant cytoplasm and nuclear spindling.

Supplementary Table S4. Agreement between pathologist and AI-driven NCP on mIF-driven NCP according to histological variation

	ICC (95% CI)		
	Urothelial carcinoma without divergent differentiation/subtype (n=56)	Urothelial carcinoma with divergent differentiation/subtype (n=57)	Non-urothelial carcinoma (n=5)
Pathologist			
Uropathologist	0.91 (0.87 to 0.93)	0.94 (0.91 to 0.95)	0.75 (0.39 to 0.91)
Fellow 1	0.83 (0.59 to 0.91)	0.78 (0.48 to 0.89)	0.67 (0.13 to 0.89)
Fellow 2	0.83 (0.77 to 0.87)	0.84 (0.79 to 0.88)	0.61 (0.17 to 0.85)
Resident 1	0.82 (0.65 to 0.89)	0.76 (0.69 to 0.82)	0.77 (0.20 to 0.93)
Resident 2	0.84 (0.79 to 0.88)	0.84 (0.79 to 0.88)	0.63 (0.20 to 0.86)
Resident 3	0.83 (0.70 to 0.89)	0.80 (0.72 to 0.85)	0.64 (0.17 to 0.87)
AI model			
EfficientNet	0.89 (0.81 to 0.93)	0.89 (0.67 to 0.95)	0.62 (0.18 to 0.86)
EfficientNetV2	0.88 (0.83 to 0.91)	0.90 (0.85 to 0.93)	0.60 (0.12 to 0.85)
MobileNetV2	0.88 (0.84 to 0.91)	0.90 (0.87 to 0.93)	0.44 (–0.12 to 0.78)
MobileNetV3	0.81 (0.65 to 0.89)	0.87 (0.80 to 0.91)	0.33 (–0.18 to 0.71)
ResNet	0.87 (0.80 to 0.92)	0.87 (0.65 to 0.93)	0.48 (-0.0 to 0.79)
WideResNet	0.85 (0.78 to 0.90)	0.90 (0.86 to 0.92)	0.55 (0.05 to 0.8)
ShuffleNetV2	0.83 (0.68 to 0.90)	0.89 (0.84 to 0.92)	0.54 (0.03 to 0.82]

AI, artificial intelligence; NCP, neoplastic cell percentage; mIF, multiplex immunofluorescence; ICC, intraclass correlation coefficient; CI, confidence interval.

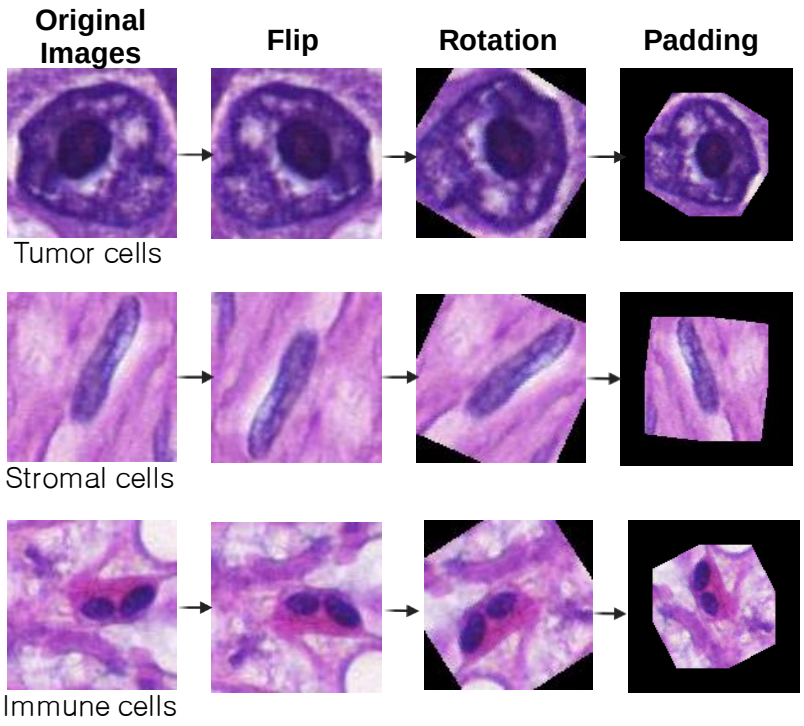

Supplementary Fig. S1. Image augmentation techniques (random flipping, rotation, and padding) are applied to tumor cells (upper), stromal cells (middle), and immune cells (lower) to improve the training of the convolutional neural network models.

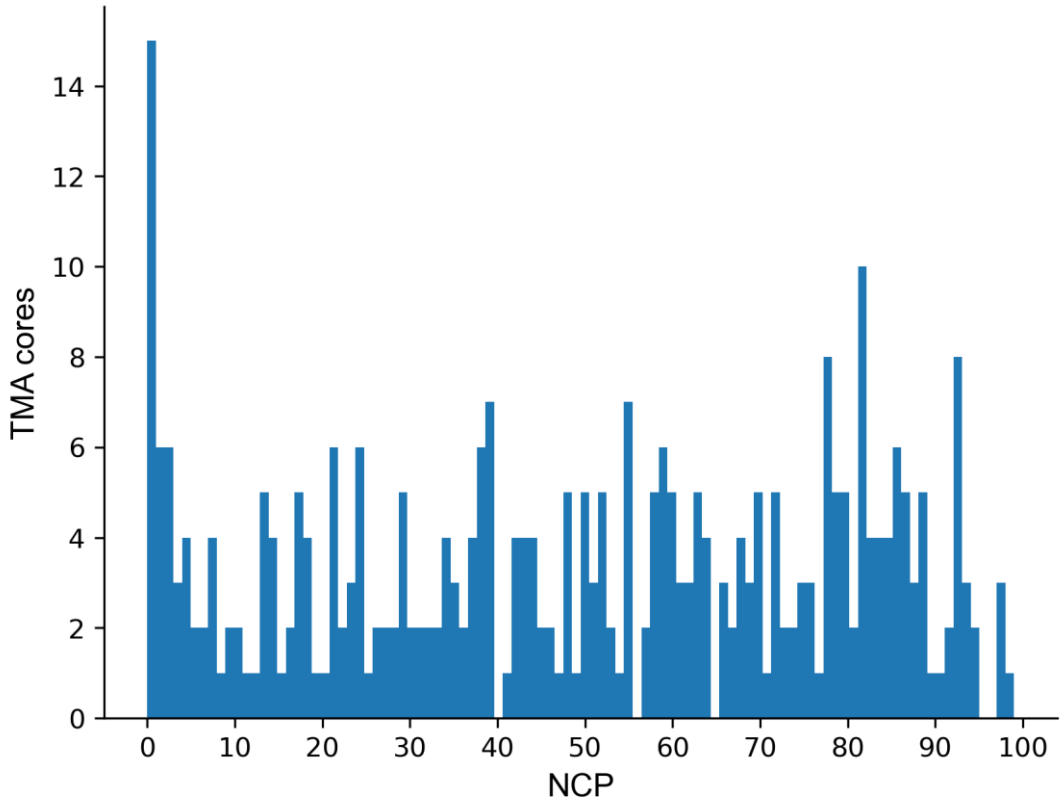

Supplementary Fig. S2. Distribution of multiplex immunofluorescence–driven neoplastic cell percentage (NCP) of 335 TMA cores of the validation cohort.

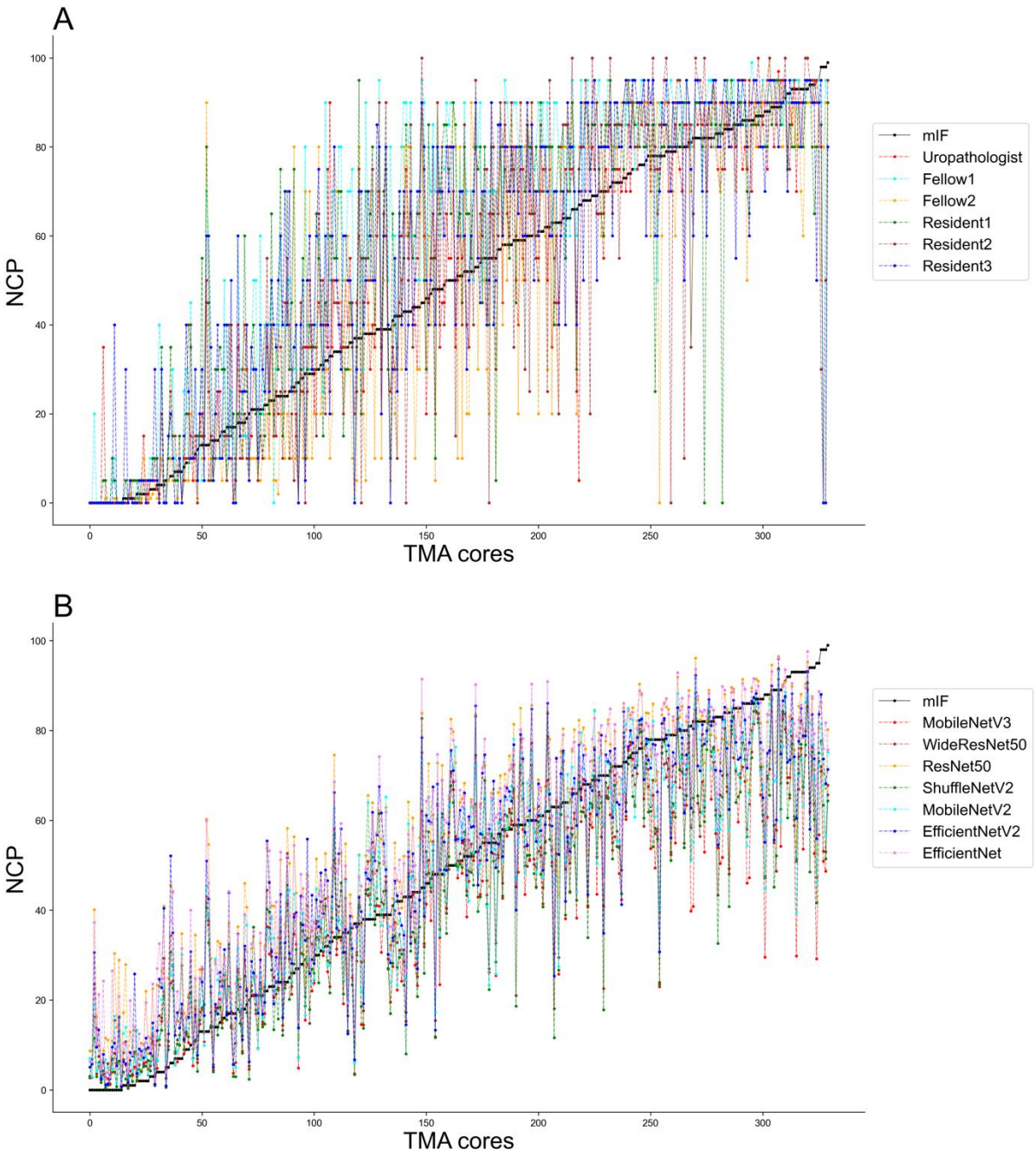

Supplementary Fig. S3. Distribution of neoplastic cell percentage (NCP) estimates by 6 individual pathologists (A) and 7 artificial intelligence (AI) models (B) for each tissue microarray (TMA) core. The TMA cores are sorted in ascending order of multiplex immunofluorescence (mIF)–driven NCP. Pathologists' NCP estimates are more variable at each range of NCP than AI-derived NCP estimates. However, AI models tend to underestimate at higher NCP.

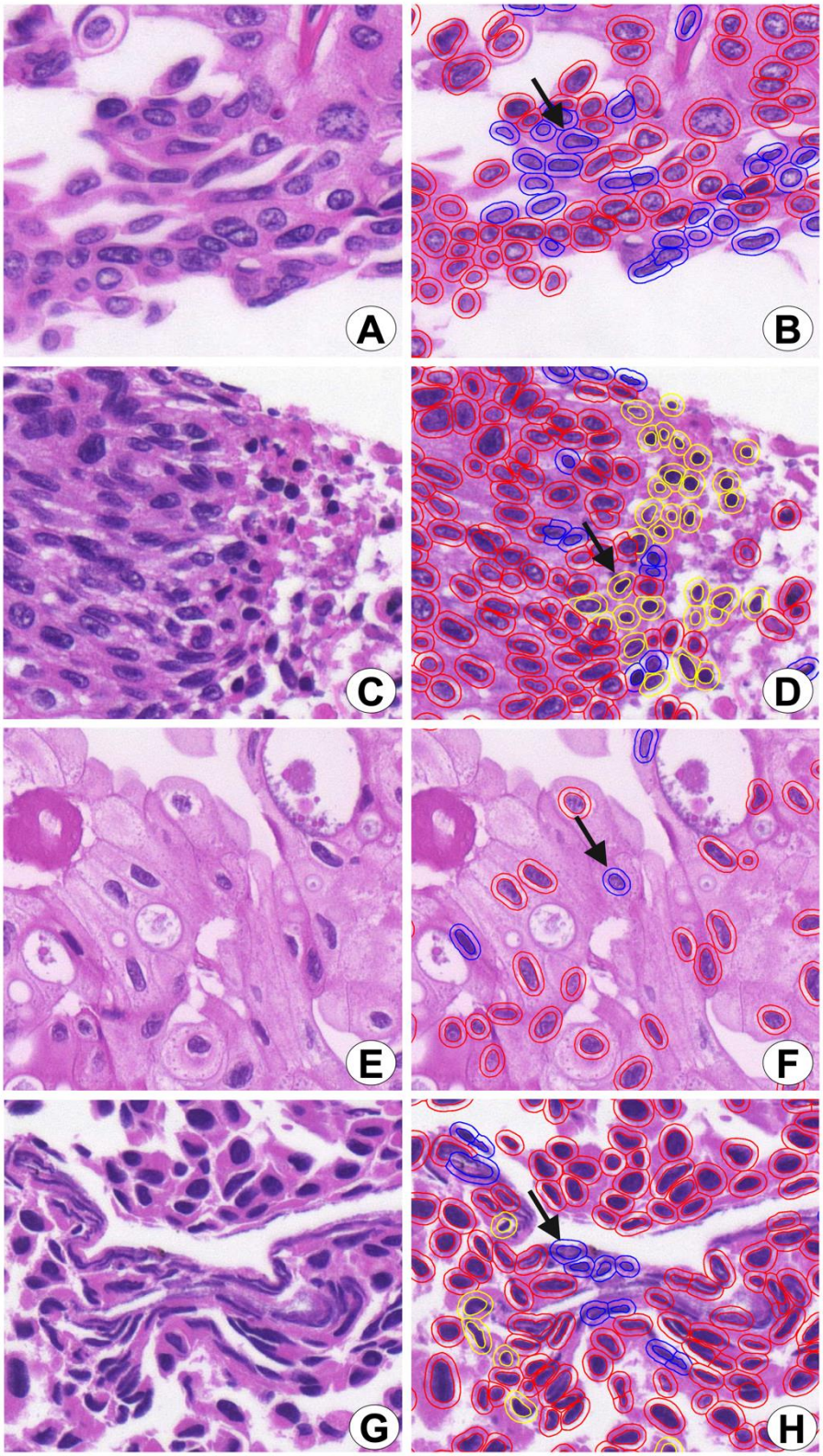

Supplementary Fig. S4. (A–H) Examples of tissue microarray (TMA) cores with high neoplastic cell percentage (≥60%) underestimated by artificial intelligence (AI) models. (A, B) Spindle-shaped nuclei misclassified as stromal cells (B, arrow). (C, D) Degenerated cells with pyknotic nuclei misclassified

as mostly immune cells (D, arrow). (E, F) Tumor cells with abundant cytoplasm misclassified as stromal cells (F, arrow). (G, H) Misclassification of tumor cells as stromal cells due to cauterization (H, arrow). (B, D, F, H) Cells classified by an AI model: red, tumor cells; blue, stromal cells; yellow, immune cells.

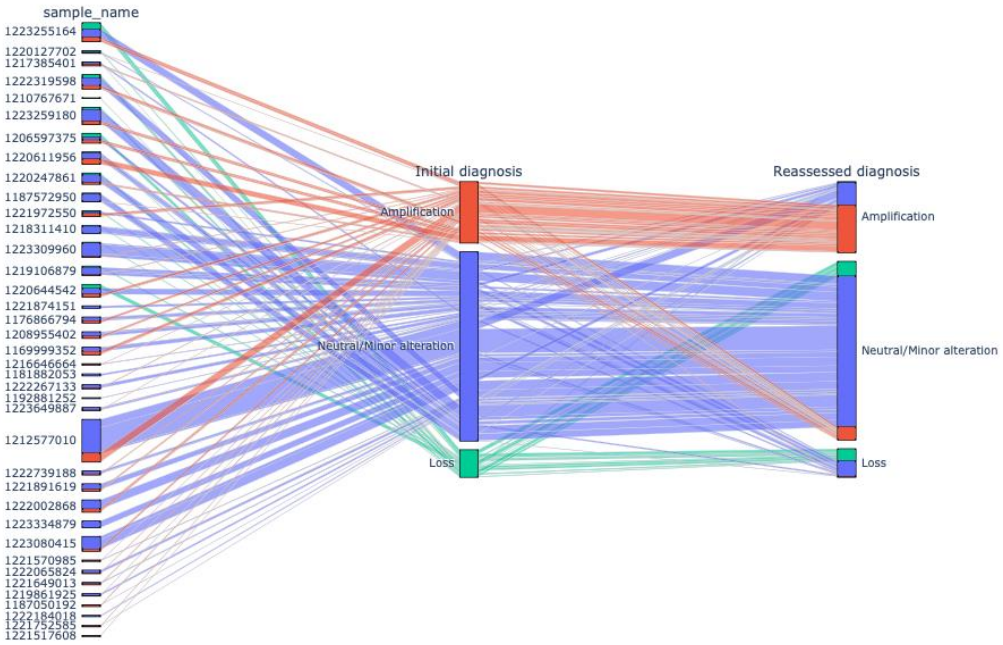

Supplementary Fig. S5. A Sankey diagram showing the copy number variation of each case in the application cohort with those at the initial diagnosis (left and middle) and those after incorporation of AI-driven neoplastic cell percentage (right).

JPTM
Journal of Pathology and Translational Medicine 2024; 58: 241-248
https://doi.org/10.4132/jptm.2024.07.14

ORIGINAL ARTICLE

International Academy of Cytology standardized reporting of breast fine-needle aspiration cytology with cyto-histopathological correlation of breast carcinoma

Shweta Pai[1,2]

[1]University Hospital Lewisham, London, UK;
[2]Department of Pathology, SCMCH & RI, Karnataka, India

Background: The International Academy of Cytology (IAC) has developed a standardized approach for reporting the findings of breast fine-needle aspiration cytology (FNAC). Accordingly, there are five chief categories of breast lesions, C1 (insufficient material), C2 (benign), C3 (atypical), C4 (suspicious), and C5 (malignant). The prognostication and management of breast carcinoma can be performed readily on the basis of this classification system. The aim of this study was to classify various breast lesions into one of the above-named categories and to further grade the C5 lesions specifically using the Robinson system. The latter grades were then correlated with modified Scarff-Bloom-Richardson (SBR) grades. **Methods:** This retrospective study was undertaken in the pathology department of a hospital located in the urban part of the city of Bangalore. All FNAC procedures performed on breast lumps spanning the year 2020 were included in the study. **Results:** A total of 205 breast lesions was classified according to the IAC guidelines into C1 (6 cases, 2.9%), C2 (151 cases, 73.7%), C3 (13 cases, 6.3%), C4 (5 cases, 2.5%), and C5 (30 cases, 14.6%) groups. The C5 cases were further graded using Robinson's system. The latter showed a significant correlation with the SBR system (concordance=83.3%, Spearman correlation=0.746, Kendall's tau-b=0.736, kappa=0.661, standard error=0.095, $p \leq .001$). **Conclusions:** A standardized approach for FNAC reporting of breast lesions, as advocated for by the IAC, improves the quality and clarity of the reports and assures diagnostic reproducibility on a global scale. Further, the cytological grading of C5 lesions provides reliable cyto-prognostic scores that can help assess a tumor's aggressiveness and predict its histological grade.

Key Words: International Academy of Cytology; Robinson's grading; Scarff-Bloom-Richardson grading; Breast neoplasms; Fine-needle aspirations

Received: March 19, 2024 **Revised:** July 11, 2024 **Accepted:** July 12, 2024
Corresponding Author: Shweta Pai, MBBS, MD, DipRCPath, FRCPath, University Hospital Lewisham, Lewisham High Street, London SE13 6LH, UK
Tel: +44-7958076986, E-mail: drshwetapai02@gmail.com

The prevalent perception of breast cancer as the most common kind of cancer affecting predominantly the Western hemisphere is no longer true. For instance, breast cancer was recently reported to have overtaken cervical cancer in India to become the most common cancer. According to the Indian Council of Medical Research, 150,000 new cases of breast cancer were reported in the year 2016 [1]. This surging new trend has directed the resolve of the national health planning sector toward identifying the best-available diagnostic tools for early-stage cancer detection. Mass deployment of such a tool would help to ensure better treatment outcomes marked by increased life expectancy of the survivors. By a majority consensus, fine-needle aspiration cytology (FNAC) was identified as one such ideal technique. The International Academy of Cytology (IAC) has formulated a process to ensure a standardized and comprehensive approach to FNAC reporting. Accordingly, they have categorized breast lesions into five categories, C1–C5 (C-code). At the inaugural Yokohama International Congress, attended by breast cancer specialists, there was a discussion on the use of a three- or a five-stage coding system. Congress attendees ultimately reached a consensus to employ a five-stage system: category 1, insufficient material; category 2, benign; category 3, atypical, probably benign; category 4, suspicious, probably in situ or invasive carcinoma; category 5, malignant.

pISSN 2383-7837
eISSN 2383-7845

Since the proposal of the aforementioned coding system, it has been widely employed on a worldwide scale. However, the respective definitions for categories 3 and 4 have recently come under scrutiny, as there is a recognized need for further debate on the grey area of atypia [2]. The IAC has attempted to refine these definitions by outlining specific criteria or scenarios wherein atypia can be deemed an appropriate diagnosis, which include the presence of epithelial hyperplasia with marked dispersal of columnar cells and minimal nuclear atypia, where the differential diagnosis is epithelial hyperplasia or low-grade intraductal carcinoma; the presence of intraductal papillomas with marked dispersal and diagnostic stellate papillary fragments, where the differential diagnosis is low-grade intraductal carcinoma; the presence of epithelial hyperplasia with a complex cribriform or micropapillary pattern, where the differential diagnosis is low-grade intraductal carcinoma; the presence of stromal hypercellularity without necrosis or nuclear atypia in a case of otherwise typical fibroadenoma, with consideration of the possibility of a low-grade phyllodes tumor; and the presence of smears with scant cellularity but minute epithelial fragments and single cells exhibiting eccentric cytoplasm, where the differential diagnosis is lobular carcinoma in situ or lobular carcinoma.

The IAC has established a checklist for FNAC of breast lesions, where an analytical approach based on cytological diagnostic criteria and pattern recognition can be used by cytopathologists for generating reports [2].

Histological grading of breast carcinoma employing the Elston-Ellis modification of the Scarff-Bloom-Richardson (SBR) grading system is a well-known and accepted approach with good correlation prognostically [3]. However, significant ambiguity persists around cytological grades. While many systems have been proposed to grade breast cancers preoperatively, the grading system of Robinson et al. best correlates with the SBR system [4-11].

In this current age of neo-adjuvant chemotherapy, it is highly recommended that the FNAC report incorporates grading of breast carcinoma. This would not only assist in the prognostication of breast cancer, but also be useful in cases that reject surgeries, cases with locally advanced disease, and cases of elderly patients with other co-morbidities [12,13].

Hence, the aim of the present study was to classify lesions of breast cancer diagnosed by FNAC according to the IAC scheme (C1–C5) with additional grading of malignant breast lesions (C5) using Robinson's system and to finally correlate the cytological grading with the standard Elston-Ellis modification of the SBR system.

MATERIALS AND METHODS

The current retrospective study was undertaken in the Department of Pathology at a tertiary medical care center in Bangalore city. A total of 205 patients who underwent an FNAC procedure for breast lumps between January 1, 2020, and December 31, 2020, were included in the study. Any cases subjected to neo-adjuvant chemotherapy were excluded. The FNAC technique was performed using 10-cc syringes with a 22–23-gauge needle under aseptic conditions. The samples obtained were smeared on glass slides and fixed with 95% ethyl alcohol. Staining was performed using hematoxylin and eosin and Leishman's method. IAC standardized reporting was used to classify all breast lesions into distinct C1–C5 categories. Further, the lesions that belonged to the C5 category were cytologically graded using Robinson's system.

The subsequent mastectomy specimens of breast carcinoma, received in the histopathology department, were fixed in 10% formalin. These specimens were grossly and aptly sampled after adequate fixation. The tissue samples were processed, and slides were prepared. Staining was performed using hematoxylin and eosin stain. Histological typing and further grading were performed using the gold-standard Elston-Ellis modification of the SBR grading system. Finally, cytological and histological grades were correlated for all the breast carcinoma cases (Tables 1, 2) [3,4].

Statistical analysis, including descriptive analysis and contingency table analysis (cross-tabulation procedure), was performed using SPSS software ver. 20 (IBM Corp., Armonk, NY, USA).

Table 1. Robinson's cytological grading of breast carcinoma

	Score 1	Score 2	Score 3
Dissociation	Cells mostly in clusters	Mixture of single and cell clusters	Cells mostly single
Cell size	1–2 × RBC size	3–4 × RBC size	≥5 × RBC size
Cell uniformity	Monomorphic	Mildly pleomorphic	Pleomorphic
Nucleoli	Indistinct	Noticeable	Prominent or pleomorphic
Nuclear margin	Smooth	Folds	Buds or clefts
Chromatin	Vesicular	Granular	Clumped and cleared

RBC, red blood cell.

https://doi.org/10.4132/jptm.2024.07.14

RESULTS

In the present study, 205 patients aged 20–60 years underwent FNAC for breast masses. According to the IAC standardized reporting, they could be graded with a C-code (C1–C5). Follow-up data were available for 127 of the cases, among which 96 were benign and 31 were malignant (Table 3).

Table 2. Modified Scarff-Bloom-Richardson histological grading of breast carcinoma

Feature	Score
Tubule formation (%)	
Majority of tumor (>75)	1
Moderate degree (10–75)	2
Little or none	3
Nuclear pleomorphism	
Small, uniform cells	1
Moderate increase in size/variation	2
Marked variation	3
Mitotic counts (per 10, 40× fields)	
0–5	1
6–10	2
>11	3
Grade	
Grade 1 (well differentiated)	3–5
Grade 2 (moderately differentiated)	6–7
Grade 3 (poorly differentiated)	8–9

Table 3. Correlation between IAC grading and histopathology follow-up

IAC grading cytology	Histopathology follow-up		No follow-up
	Benign	Malignant	
Category 1 (n=6)	1 (16.7)	0	5 (83.3)
Category 2 (n=151)	84 (55.6)	0	67 (44.4)
Category 3 (n=13)	10 (77.0)	0	3 (23.0)
Category 4 (n=5)	1 (20.0)	3 (60.0)	1 (20.0)
Category 5 (n=30)	0	28 (93.3)	2 (6.7)
Total (n=205)	96 (46.9)	31 (15.1)	78 (38.0)

Values are presented as number (%).
IAC, International Academy of Cytology.

Category 1: Insufficient material

Smears that do not show epithelial cells are labeled as insufficient or inadequate collections. According to the MD Anderson Cancer Center Group's proposal, the presence of 4–6 well-visualized groups ≥10 cells or flat sheets is considered adequate [14].

In the current study, the C1 category comprised six cases (2.9%), one of which was diagnosed as a case of benign breast disease on follow-up (Table 4).

Category 2: Benign

Category 2 comprised lesions showing benign epithelial clusters with no atypical or malignant features. High cellularity is rare in these cases, and cells present a low nucleocytoplasmic ratio, fine chromatin, no pleomorphism, and a smooth nuclear membrane. Fatty fragments are common, along with bare nuclei. Few cases show apocrine cells or histiocytes.

In the present study, most lesions belonged to the C2 category (151 cases, 73.7%). Among these 151 lesions, 64 (42.4%) were fibroadenomas, 31 (20.5%) were fibrocystic diseases, 24 (15.9%) were benign breast diseases, 12 (8.0%) were fibroadenoma with fibrocystic disease and gynecomastia, and 8 (5.3%) were inflammatory breast lesions (Fig. 1).

In the C2 category, follow-up data were available for 84 cases, including 47 cases of fibroadenomas, 18 cases of fibrocystic diseases, five cases of fibroadenomas with fibrocystic disease, four cases of gynecomastia, five cases of inflammatory breast lesions, and five cases of benign breast diseases (Table 4).

Category 3: Atypical, probably benign

Findings of category 3 lesions are similar to those in the benign category but with slight crowding, greater cellularity, pleomorphism, three-dimensional grouping, and nuclear enlargement.

Table 4. Cyto-histological correlation of category 1 and 2 lesions

Histopathology	IAC grading						
	C1 (n=6)	C2 (n=151)					
		Inflammatory lesion (n=8)	FA (n=64)	FCD (n=31)	FA with FCD (n=12)	BBD (n=24)	Gynecomastia (n=12)
BBD	1 (16.7)	1 (12.5)	-	-	-	5 (20.8)	-
Inflammatory lesion/abscess	-	4 (50.0)	-	-	-	-	-
FA	-	-	47 (73.4)	-	2 (16.7)	-	-
FCD	-	-	-	18 (58.0)	-	-	-
FA with FCD	-	-	-	-	3 (25.0)	-	-
Gynecomastia	-	-	-	-	-	-	4 (33.3)

Values are presented as number (%).
IAC, International Academy of Cytology; FA, fibroadenoma; FCD, fibrocystic disease; BBD, benign breast disease.

C3 lesions in our study were present in 13 cases (6.4%), including four (30.8%) each of fibrocystic disease with atypia and benign fibroepithelial neoplasm, three cases (23%) of fibroadenoma with atypia, and one case (7.7%) each of benign phyllodes tumor and papillary neoplasm (Fig. 2).

Follow-up data were available for 10 C3 cases, including three cases each of fibrocystic disease with atypia and fibroadenoma with atypia, two cases of benign fibroepithelial neoplasms, and one case each of benign phyllodes and a papillary neoplasm (Table 5).

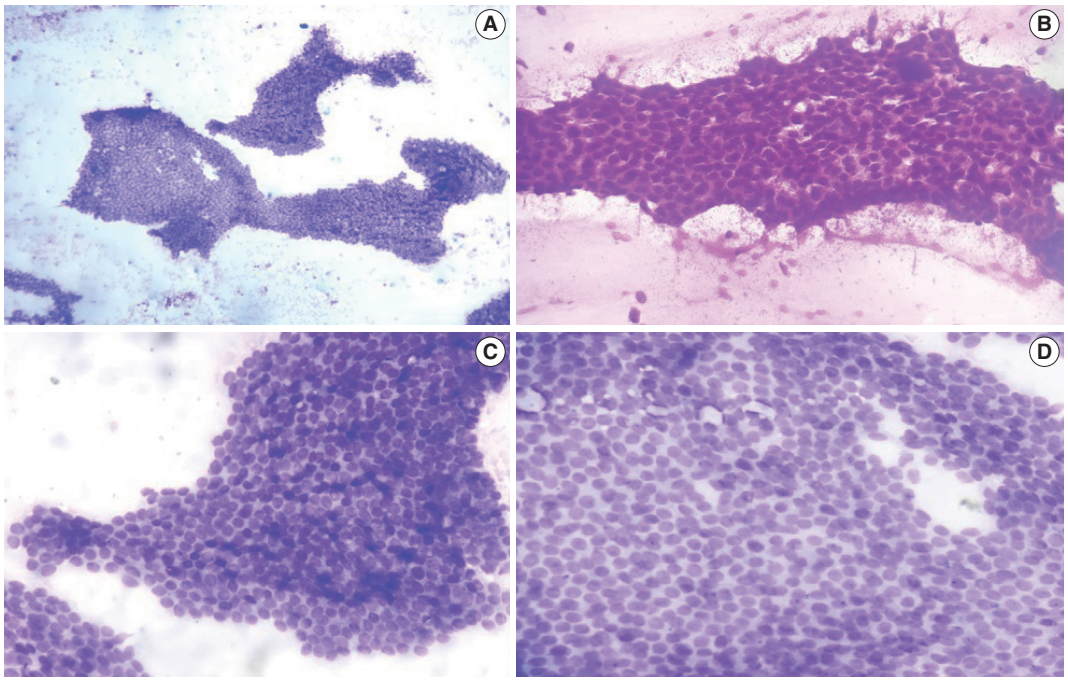

Fig. 1. C2 (benign category). (A, B) Fibroadenoma; note the branching sheets of cohesive cells giving the antler horn pattern (B, Leishmans). (C, D) Fibroadenoma with epithelial hyperplasia.

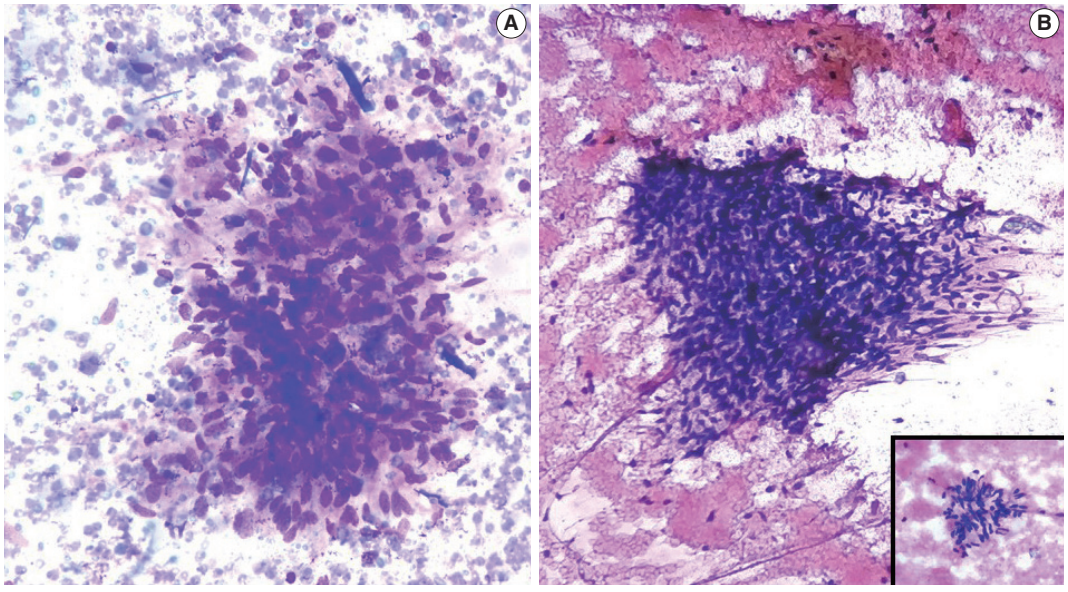

Fig. 2. C3 (atypical category). (A, B) Benign phyllodes tumor. Note the abundance of stromal fragments. The inset shows a high-power view (B, Leishmans).

https://doi.org/10.4132/jptm.2024.07.14

Category 4: Suspicious, probably in situ or invasive carcinoma

Category 4 lesions exhibit highly atypical findings that remain insufficient to label them malignant. Cases in this category include those with poorly preserved or hypocellular smears, those with focally atypical cells in a benign background, and those with an insufficient degree of atypia to classify C5 but where the atypia is greater than that of C3.

In the current study, C4 lesions suspicious for malignancy accounted for five cases (2.4%). On follow-up, three cases were confirmed to be ductal carcinoma; however, one case was negative for malignancy (Table 5).

Category 5: Malignant

These lesions show high cellularity. Cells are seen in singles or loose clusters, and malignant features such as hyperchromasia, high nucleocytoplasmic ratio, irregular nuclear contour, and conspicuous nucleoli are noted. Some cases show necrotic debris in the background.

In the present study, C5 lesions were the second most common entity, found in 30 cases (14.6%).

Follow-up was available for only 20 C5 cases, which were all confirmed to be ductal carcinoma (Table 5, Fig. 3).

All C5 cases underwent cytological grading using Robinson's system [4], and histopathological grading was completed using the Elston-Ellis modification of the SBR grading system [3].

In the present study, the Robinson grades showed very good concordance (83.3%) with the modified (Elston-Ellis) SBR grades, with high correlation (0.746), high Kendall's tau-b (0.736), high kappa value (0.661), substantial agreement, and a significant p-value (< .001) (Tables 6, 7, Fig. 4).

DISCUSSION

Diagnosing breast cancers at an early stage is imperative for favorable treatment outcomes, but cases often go undiagnosed

Table 5. Cyto-histological correlation of category 3, 4, and 5 lesions

Histopathology	IAC grading						
	C3 (n=13)					C4 (n=5)	C5 (n=30)
	FCD with atypia (n=4)	Benign fibroepithelial neoplasm (n=4)	FA with atypia (n=3)	Benign phyllodes tumor (n=1)	Papillary neoplasm (n=1)	Suggestive of ductal carcinoma	Ductal carcinoma
FA	1 (25.0)	-	2 (66.7)	-	-	-	-
Benign phyllodes	-	-	-	1 (100)	-	-	-
Complex FA	-	1 (25.0)	-	-	-	-	-
FA with apocrine change	-	-	1 (33.3)	-	-	-	-
Juvenile FA	-	1 (25.0)	-	-	-	-	-
FCD	2 (50.0)	-	-	-	-	-	-
Duct papilloma	-	-	-	-	-	-	-
Duct carcinoma	-	-	-	-	1 (100)	3 (60.0)	28 (93.3)
Negative for malignancy	-	-	-	-	-	1 (20.0)	-

Values are presented as number (%).
IAC, International Academy of Cytology; FCD, fibrocystic disease; FA, fibroadenoma.

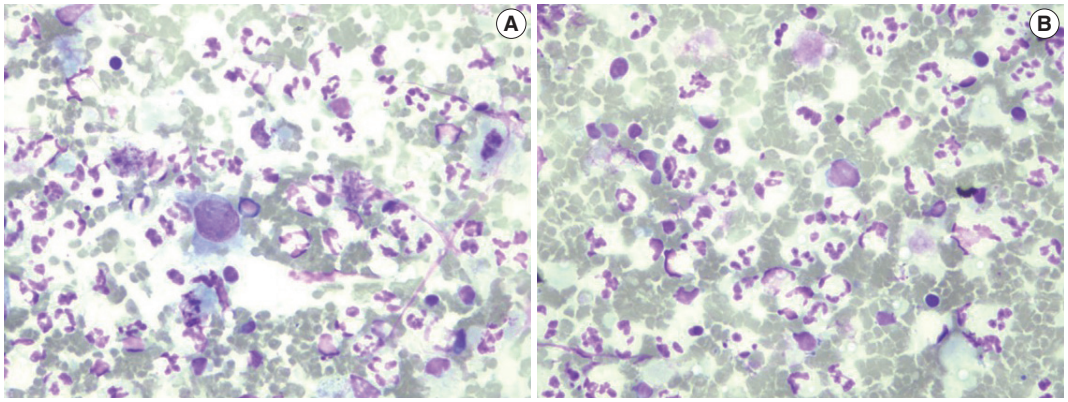

Fig. 3. C4 (suspicious for malignancy category). (A, B) Occasional malignant cells can be seen in the background of inflammatory cells.

Table 6. Comparison of Robinson and SBR grades

Grade	No. of cases	
	Robinson grading	SBR grading
Grade 1	11 (37)	7 (23.3)
Grade 2	18 (60)	21 (70)
Grade 3	1 (3)	2 (6.7)
Total	30 (100)	30 (100)

Vaues are presented as number (%).
SBR, Scarff-Bloom-Richardson.

Table 7. Statistical correlation of Robinson and SBR grades

Statistical analysis	Value
Concordance (CR)	83.3%
Spearman correlation (ρ)	0.746
Kendall's tau-b (t_b)	0.736
Kappa (κ)	0.661
Standard error	0.095
p-value	<.001

SBR, Scarff-Bloom-Richardson.

for socio-economic reasons. Hence, it is of paramount importance that an easy, cost-effective, and reliable investigation like FNAC be performed in such circumstances [15]. FNAC is a rapid, accurate, and relatively painless procedure [16]; however, translation of cytological patterns into histopathological patterns can be difficult, hindering diagnosis [17]. In such a scenario, structured reporting using IAC guidelines will not only help improve the quality and accuracy of the reports, but also ensure reproducibility of the findings on a global scale [2].

Category 1

Cases in the C1 category include those with an inadequate/insufficient sample, such as cases marked by hypocellular smears, errors in spreading/staining, excessive blood, crushing artifacts, degenerated cells, and poor fixation. However, cases with cysts, abscess, fat necrosis, or intra-mammary lymph nodes are not considered C1. The risk for malignancy among C1 cases is 4.8%

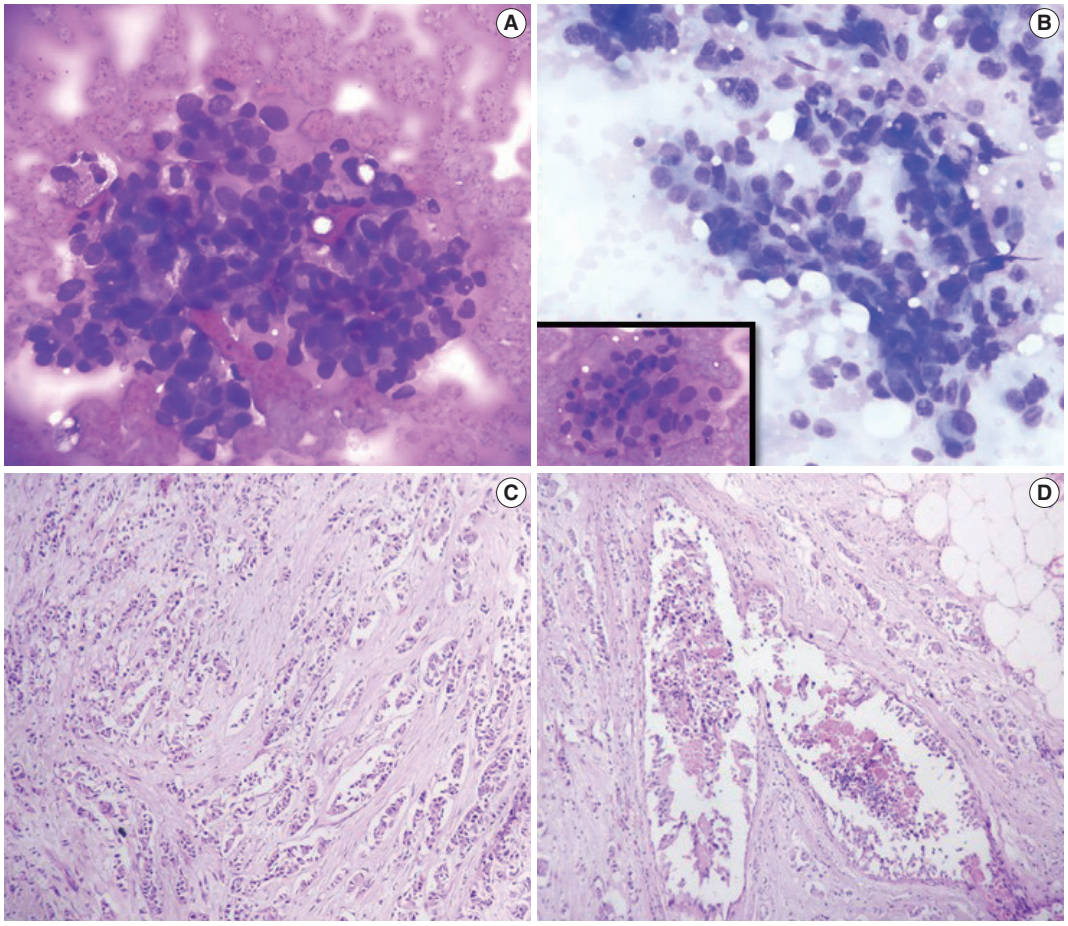

Fig. 4. C5 (malignant category). Invasive ductal carcinoma. (A, B) Cytological images; note the discohesive cluster of malignant cells with a high nucleocytoplasmic ratio, irregular nuclear membrane, and clumped chromatin. The inset shows a high-power view. (C, D) Histopathological images. Note the infiltrative cords, small nests, and occasional tubules of tumor cells within a prominent desmoplastic stroma.

https://doi.org/10.4132/jptm.2024.07.14

[18]. As shown in Table 8, our study documented a C1 prevalence of 2.9%, which was identical to that reported by Haobam et al. [19]. Meanwhile, Georgieva et al. [20] and Bajwa and Zulfiqar [21] reported much higher frequencies of C1 cases, which could be explained partly by the use of faulty techniques and inadequate expertise [22].

Category 2

Cases in the C2 category are considered benign and include instances of fibroadenoma, fat necrosis, abscess, granulomatous mastitis, and other benign entities such as intra-mammary lymph nodes. Cytology smears in these cases will demonstrate a regular ductal epithelium, cysts, or fibrofatty fragments depending on the etiology. The risk for malignancy is 1.4% [18].

Most of the cases in our study were C2 cases (73.7%), concurring with rates in other studies (Table 8). Among the C2 cases, fibroadenomas were most common (42%), as reported by Modi et al. [22], Panwar et al. [1], and Bajwa and Zulfiqar [21]. The second most common C2 lesions were those indicating fibrocystic disease (21%), as in Bajwa and Zulfiqar [21].

Category 3

Cases in the C3 category are atypical but probably benign and include papillary lesions and suspected phyllodes tumors. Cytology smears in such instances may show pleomorphism, increased cellularity, and loss of cohesion. The risk of malignancy is 13% [18]. No definitive surgery is recommended for cases in this category. The prevalence of C3 cases was 6.4% in the present study, similar to reports by both Bajwa and Zulfiqar [21] and Panwar et al. [1]. Meanwhile, Georgieva et al. [20] encountered a much lower frequency of C3 lesions (Table 8).

Category 4

Category 4 cases are suspicious for malignancy. Cytology findings may show scant/poor preservation of cells, along with occasional malignant cells or some features of malignancy. The overall risk of malignancy is 97.1% [18]. However, no definitive surgery is recommended for this category. Panwar et al. [1] reported very few cases (1.7%) of C4 lesions, which concurred with observations in our study. However, other studies have reported higher frequencies of C4 cases (Table 8).

Category 5

Category 5 is the malignant category. Here, cytology smears will show overt malignant features like a high nucleo-cytoplasmic ratio, hyperchromasia, irregular nuclear contours, and conspicuous nucleoli. The risk for malignancy is 100% [18]. C5 lesions were the second most common lesions after C2 lesions in our and other studies, which indicates a rising trend in the frequency of breast cancer cases.

Table 8. Comparison of various studies that used International Academy of Cytology Grading

	C1	C2	C3	C4	C5
Modi et al. [22]	1.4	72	3.4	6.5	16.7
Georgieva et al. [20]	25.6	44.3	2.2	5.3	22.5
Bajwa and Zulfiqar [21]	13.6	60.6	6.2	9.3	10.3
Haobam et al. [19]	2.9	50	3.5	6.5	37.1
Panwar et al. [1]	1.3	82.6	5.7	1.7	8.4
Present study	2.9	73.7	6.4	2.4	14.6

Values are presented as percentage.

Table 9. Comparison of correlation and concordance of Robinson and SBR grades between studies

	Arul and Masilamani [23]	Saha et al. [24]	Einstien et al. [25]	Present study
Spearman rank (r)	0.801	0.799	0.738	0.746
Kendall's tau-b rank (t)	0.783	-	-	0.736
Concordance (%)	88.3	77.2	77.7	83.3
Kappa (κ)	0.737	0.62	0.61	0.661
p-value	<.001	<.001	<.001	<.001
Agreement	Substantial	Substantial	Substantial	Substantial

In the present study, malignant cases (C5) were accurately identified by FNAC as later confirmed by histopathology. This was also true in Panwar et al. [1]. However, two cases (C5) were lost to follow-up in our study (Table 8).

Robinson's cytological system was used to grade all C5 lesions. This system is an excellent predictor of the aggressiveness of a tumor; compared to the standard histological grading approach, i.e., the modified SBR system, it exhibits substantial correlation in terms of Spearman's rank, Kendall's tau-b rank, concordance, kappa value, and p-value. This finding was reported in other studies like those by Arul and Masilamani [23] and Saha et al. [24] (Table 9) [25-28].

A standardized approach as advocated for by the IAC for FNAC reporting of breast lesions will not only improve the quality and clarity of reports, but also assures their reproducibility, internationally. Furthermore, the cytological grading of C5 lesions provides cyto-prognostic scores that can help assess the aggressiveness of a tumor and predict its histological grade.

Ethics Statement

All procedures performed in the current study were approved by the central government's institutional research ethics committee (reference no.: 532/L/11/12/Ethics/ESICMC&PGIMSR/Estt.Vol.IV; Jun 22, 2021) in ac-

cordance with the 1964 Declaration of Helsinki and its later amendments. Formal written informed consent was not required, with a waiver granted by the research ethics committee.

Availability of Data and Material

The datasets generated or analyzed during the study are available from the corresponding author on reasonable request.

Code Availability

Not applicable.

ORCID

Shweta Pai https://orcid.org/0000-0002-3164-8219

Conflicts of Interest

The authors declare that they have no potential conflicts of interest.

Funding Statement

No funding to declare.

References

1. Panwar H, Ingle P, Santosh T, Singh V, Bugalia A, Hussain N. FNAC of breast lesions with special reference to IAC standardized reporting and comparative study of cytohistological grading of breast carcinoma. J Cytol 2020; 37: 34-9.
2. Field AS, Schmitt F, Vielh P. IAC standardized reporting of breast fine-needle aspiration biopsy cytology. Acta Cytol 2017; 61: 3-6.
3. Elston CW, Ellis IO. Pathological prognostic factors in breast cancer. I. The value of histological grade in breast cancer: experience from a large study with long-term follow-up. Histopathology 1991; 19: 403-10.
4. Robinson IA, McKee G, Nicholson A, et al. Prognostic value of cytological grading of fine-needle aspirates from breast carcinomas. Lancet 1994; 343: 947-9.
5. Hunt CM, Ellis IO, Elston CW, Locker A, Pearson D, Blamey RW. Cytological grading of breast carcinoma: a feasible proposition? Cytopathology 1990; 1: 287-95.
6. Mouriquand J, Gozlan-Fior M, Villemain D, et al. Value of cytoprognostic classification in breast carcinomas. J Clin Pathol 1986; 39: 489-96.
7. Bansal C, Pujani M, Sharma KL, Srivastava AN, Singh US. Grading systems in the cytological diagnosis of breast cancer: a review. J Cancer Res Ther 2014; 10: 839-45.
8. Robinson IA, McKee G, Kissin MW. Typing and grading breast carcinoma on fine-needle aspiration: is this clinically useful information? Diagn Cytopathol 1995; 13: 260-5.
9. Wani FA, Bhardwaj S, Kumar D, Katoch P. Cytological grading of breast cancers and comparative evaluation of two grading systems. J Cytol 2010; 27: 55-8.
10. Das AK, Kapila K, Dinda AK, Verma K. Comparative evaluation of grading of breast carcinomas in fine needle aspirates by two methods. Indian J Med Res 2003; 118: 247-50.
11. Phukan JP, Sinha A, Deka JP. Cytological grading of breast carcinoma on fine needle aspirates and its relation with histological grading. South Asian J Cancer 2015; 4: 32-4.
12. Skrbinc B, Babic A, Cufer T, Us-Krasovec M. Cytological grading of breast cancer in Giemsa-stained fine needle aspiration smears. Cytopathology 2001; 12: 15-25.
13. Khan N, Afroz N, Rana F, Khan M. Role of cytologic grading in prognostication of invasive breast carcinoma. J Cytol 2009; 26: 65-8.
14. Sneige N. Should specimen adequacy be determined by the opinion of the aspirator or by the cells on the slides? Cancer 1997; 81: 3-5.
15. Hussain MT. Comparison of fine needle aspiration cytology with excision biopsy of breast lump. J Coll Physicians Surg Pak 2005; 15: 211-4.
16. McManus DT, Anderson NH. Fine needle aspiration cytology of the breast. Curr Diagn Pathol 2001; 7: 262-71.
17. Tariq GR, Haleem A, Zaidi AH, Afzal M, Abbasi S. Role of FNA cytology in the management of carcinoma breast. J Coll Physicians Surg Pak 2005; 15: 207-10.
18. Montezuma D, Malheiros D, Schmitt FC. Breast fine needle aspiration biopsy cytology using the newly proposed IAC Yokohama System for Reporting Breast Cytopathology: the experience of a single institution. Acta Cytol 2019: 1-6.
19. Haobam S, Thiyam U, Sharma DC. Cytomorphological study of breast lesions with sonomammographic correlation. J Evol Med Dent Sci 2015; 4: 14137-42.
20. Georgieva RD, Obdeijn IM, Jager A, Hooning MJ, Tilanus-Linthorst MM, van Deurzen CH. Breast fine-needle aspiration cytology performance in the high-risk screening population: a study of *BRCA1/BRCA2* mutation carriers. Cancer Cytopathol 2013; 121: 561-7.
21. Bajwa R, Zulfiqar T. Association of fine needle aspiration cytology with tumor size in palpable breast lesions. Biomedica 2010; 26: 124-9.
22. Modi P, Oza H, Bhalodia J. FNAC as preoperative diagnostic tool for neoplastic and non-neoplastic breast lesions: a teaching hospital experience. Natl J Med Res 2014; 4: 274-8.
23. Arul P, Masilamani S. Comparative evaluation of various cytomorphological grading systems in breast carcinoma. Indian J Med Paediatr Oncol 2016; 37: 79-84.
24. Saha K, Raychaudhuri G, Chattopadhyay BK, Das I. Comparative evaluation of six cytological grading systems in breast carcinoma. J Cytol 2013; 30: 87-93.
25. Einstien D, Omprakash BO, Ganapathy H, Rahman S. Comparison of 3-tier cytological grading systems for breast carcinoma. ISRN Oncol 2014; 2014: 252103.
26. Sinha S, Sinha N, Bandyopadhyay R, Mondal SK. Robinson's cytological grading on aspirates of breast carcinoma: correlation with Bloom Richardson's histological grading. J Cytol 2009; 26: 140-3.
27. Vasudev V, R R, V G. The cytological grading of malignant neoplasms of the breast and its correlation with the histological grading. J Clin Diagn Res 2013; 7: 1035-9.
28. Pal S, Gupta ML. Correlation between cytological and histological grading of breast cancer and its role in prognosis. J Cytol 2016; 33: 182-6.

JPTM
Journal of Pathology and Translational Medicine 2024; 58: 249-254
https://doi.org/10.4132/jptm.2024.05.15

CASE STUDY

Intravascular schwannoma as an extremely unusual cause of vein obstruction: a case report

Luis Miguel Chinchilla-Tábora[1,2,3], Beatriz Segovia Blázquez[4], José María Sayagués[1,2,3], Marta Rodríguez González[1,2,3], Joaquín González-Rivero[1,3], José Antonio Muñoz León[1,3], Andrea Beatriz Jiménez Pérez[1,3], Idalia González Morais[1], Diego Bueno-Sacristán[1], María Dolores Ludeña[1,2,3]

[1]Pathology Department, University Hospital of Salamanca, Salamanca;
[2]University of Salamanca, Salamanca;
[3]Institute for Biomedical Research of Salamanca (IBSAL), Salamanca;
[4]Pathology Department, Nuestra Señora de Sonsoles Hospital, Ávila, Spain

The blood vessel lumen is an extremely rare location for a benign peripheral nerve sheath tumor like schwannoma. Less than 10 cases have been previously reported. In this report, we present a case of a 68-year-old woman who had a soft tissue nodule at the posterior calf of her left leg during a physical examination. Pathological examination was performed after complete surgical excision. The patient underwent follow-up for 12 months after surgery without evidence of recurrence or any other complication. This is the first case of intravascular schwannoma reported as a cause of vein obstruction. Microscopically, the tumor was composed of Schwann spindle cells that were immunoreactive for S100 protein and SOX10. This tumor was surrounded by a well-defined vascular smooth muscle wall. Prospective series are required to improve the knowledge on the underlying mechanisms of intravascular schwannoma development.

Key Words: Neurilemmoma; Peripheral nervous system neoplasms; Nerve sheath neoplasms; Peripheral nervous system; Schwann cells

Received: April 8, 2024 **Revised:** May 5, 2024 **Accepted:** May 14, 2024
Corresponding Author: Luis Miguel Chinchilla-Tábora, MD, PhD, Servicio de Anatomía Patológica, planta cero, bloque G, Complejo Asistencial Universitario de Salamanca, Paseo de la Transición Española S/N, CP: 37007, Salamanca, Salamanca, Spain
Tel: +34-923291100 (ext. 56738), Fax: +34-923291131, E-mail: lmct@usal.es

Schwannoma is a benign neural tumor of Schwann cell origin on the nerve sheath [1]. Schwannomas are also called neurilemomas and are generally located in the deep dermis and subcutaneous tissue, but these can appear at different sites of the body. Spinal intradural extramedullary examples are common, and these form "dumbbell tumors" when expanding through the neural foramina as multiple paraspinal schwannomas. These "dumbbell tumors" are common in neurofibromatosis type 2. Cranial nerve involvement is not uncommon; cerebellopontine angle schwannoma arising from the vestibular division of the eighth cranial nerve is one of the most frequent presentations [2]. Spinal intramedullary; central nervous system (CNS); visceral, such as the gastrointestinal tract; and bone schwannomas are rare [3,4].

Low-power microscopic views of schwannomas are characterized by well-defined margins with frequent encapsulation. These tumors have two different alternating cellular areas in a biphasic growth pattern: the hypercellular areas consisting of spindle cell proliferation, Antoni A areas, and the hypocellular or cystic areas characterized by the presence of macrophages and collagen fibers, Antoni B areas. A frequently recognized morphological feature of schwannomas is the presence of Verocay bodies that consist of palisading nuclei alternating with acellular areas [5]. Immunohistochemically, schwannomas are characterized by diffuse and strong staining for S100 and SOX10 [6,7]. The diagnosis is made based on the classical morphologic characteristics, the biphasic growth pattern, and the diffuse S100 and SOX10 immunoreactivity.

Venous obstruction is the partial or complete occlusion of the blood vessel lumen and can be associated with low blood flow or increased pooling. The most common form of venous obstruction is deep vein thrombosis in the lower limb veins. Stasis results in viscosity increase and formation of microthrombi. This

pISSN 2383-7837
eISSN 2383-7845

is due to multiple factors that slow or obstruct the flow of venous blood. One of the most common causes is endothelial (intimal) damage secondary to intrinsic or external trauma. In a hypercoagulable state, a biochemical imbalance between procoagulant and anticoagulant factors occurs [8].

Intravascular schwannomas are extremely rare. In this report, we present a case of intravascular schwannoma, an unusual cause of deep venous obstruction. To the best of our knowledge, just four case reports had been published in English prior to this report [9–12]. Elucidating the signs and symptoms of this rare form of schwannoma is necessary to avoid misdiagnosis.

CASE REPORT

Case presentation

We present the case of a 68-year-old woman who had a three-year history of non-radiating pain on the medial side of her left leg, 5 cm distal to the popliteal fossa. No CNS disorders were identified at physical examination, and no other related symptoms were observed.

A soft tissue Doppler ultrasound was performed and showed a spindle-shaped to ovoid lesion, the largest diameter of which was 2.3 cm. The mass was in the deep subcutaneous tissue, near the muscular fascia (Fig. 1A, B) and did not display marked internal blood flow (Fig. 1B). The radiological characteristics of the lesion on ultrasonographic examination suggested the presence of a soft tissue tumor of probable neural origin. The lesion was completely surgically removed.

Pathologic characteristics

The macroscopic examination of the resected area revealed the presence of a soft tissue nodule, largest diameter 2.3 cm, with a vaguely spindle morphology and smooth external surface. The cut surface of the mass was grayish brown and had the consistency of rubber.

Microscopically, the tumor was nodular and composed of spindle cells. This tumor occupied the entire lumen of a venous vessel that had a thickened smooth muscle wall with focal myxoid degeneration and no elastic fibers (Fig. 1D). The lesion was composed of at least two intermingled cellular areas, at least one

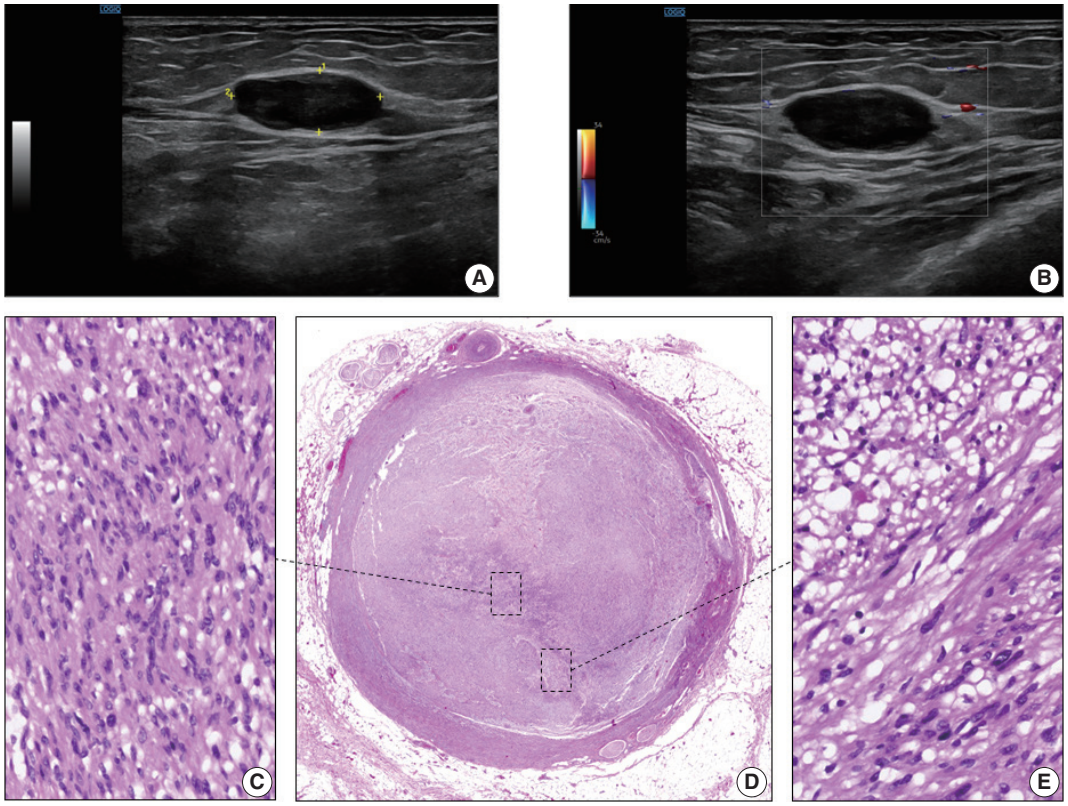

Fig. 1. Ultrasonographic imaging and morphological features. (A) Ultrasonographic characteristics of the tumor showing a 2.3 cm hypoechoic ovoid nodule. (B) Low blood flow around the tumor in the Doppler ultrasound view. (C) Hypercellular areas that consist of cohesive spindle cells (Antoni A zones). (D) The tumor shows an intravascular growth pattern, occupying the entire lumen of the blood vessel. (E) Hypocellular areas that consist of haphazardly arranged spindle cells in a loose myxoid stroma (Antoni B zones).

https://doi.org/10.4132/jptm.2024.05.15

of which shared features with the normal peripheral nerve sheath cells. Within these areas, some of the cells had elongated, fusiform, or oval hyperchromatic nuclei with sharp edges and scarce cytoplasm (Antoni A zones) (Fig. 1C); these were arranged to form parallel palisades with interposed filaments (Verocay bodies).

In addition, the tumor had areas composed of less cohesive cells with small, rounded nuclei and large pale cytoplasm in a loose myxoid stroma (Antoni B zones) (Fig. 1E). The lesion was not necrotic or hemorrhagic. Neither mitosis nor atypia was present. The venous vessel within which the tumor expanded was surrounded by tiny mature vessels, the vasa vasorum, and nerves, the nervi vasorum (Fig. 1D).

Immunohistochemistry

The tumor had typical immunohistochemical characteristics of a schwannoma. A diffuse and strong positivity for S100 protein (clone EP32, monoclonal antibody, ready-to-use on Leica BOND III system, Leica Biosystems, Newcastle Upon Tyne, UK) (Fig. 2A–D) and SOX10 (clone EP268, monoclonal antibody, ready-to-use on Leica BOND III system, Master Diagnóstica, Grenada, Spain) (Fig. 3A, B) was found in the tumor spindle cells. We also observed a normal nuclear expression level of H3K27me3 (clone C36B11, monoclonal antibody, 1:400 on Leica BOND III system, Cell Signaling Technology, Danvers, MA, USA) in the tumor cells (Fig. 3D). These markers were also positive in the nervi vasorum inside and around the vein wall. The tumor cells were negative for CD34 (clone QBEnd/10, monoclonal antibody, ready-to-use on Leica BOND III system, Leica Biosystems) (Fig. 3C), smooth muscle actin (SMA) (clone Alpha sm-1, monoclonal antibody, ready-to-use on Leica BOND III system, Leica Biosystems) (Fig. 2E, F), and CD31 (clone JC70A, monoclonal antibody, ready-to-use on Leica BOND III system, Leica Biosystems). CD34 (Fig. 3C) and CD31 highlight the endothelial elements inside the tumor and the vein endothelium surrounding the tumor. CD34 was also positive in some fibroblastic cells of the tumor stroma (Fig. 3C). SMA was positive in the smooth muscle cells of the vein wall, small vessels present in the vasa vasorum, and vessels inside the tumor (Fig. 2E, F).

DISCUSSION

Schwannoma is a nerve sheath tumor entirely or nearly entirely composed of differentiated neoplastic Schwann cells that are associated in some cases with different conditions such as

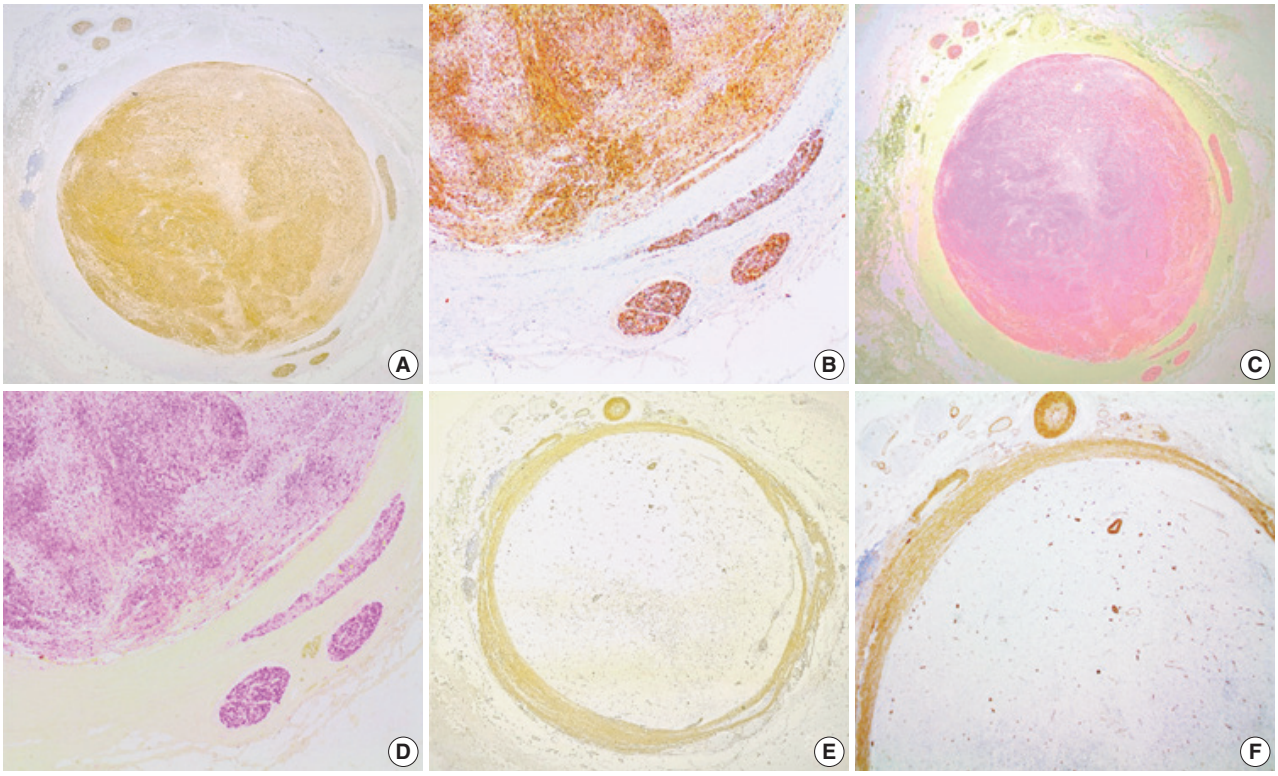

Fig. 2. Positivity for S100 protein in intravascular tumor cells (A–D) and nervi vasorum nerves (B, D). The smooth muscle cells of the vein wall show smooth muscle actin positivity (E, F).

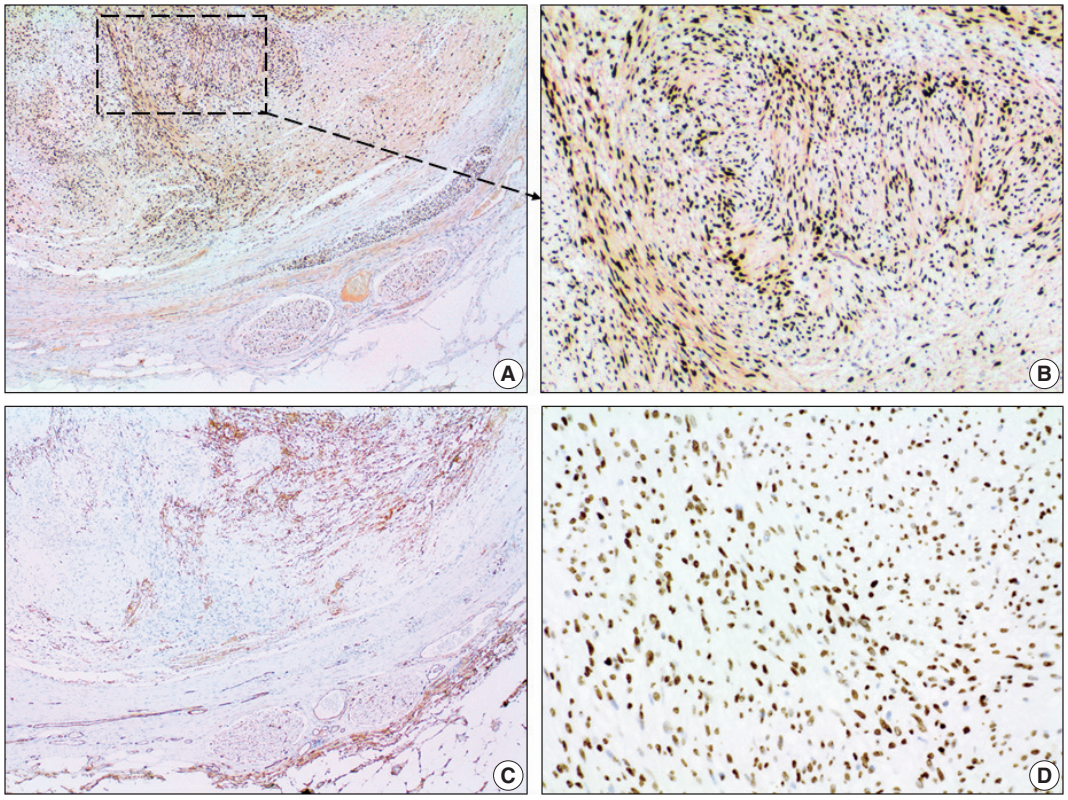

Fig. 3. Immunohistochemical characteristics. (A, B) The intravascular tumor cell positivity for SOX10. (C) Some fibroblastic cells of the tumor stroma, the endothelial cells of capillaries inside the tumor, the endothelium of the vein intima, and the vasa vasorum are CD34-positive. (D) The nuclear immunoreactivity for H3K27me3 is intact in tumor cells.

type 2 neurofibromatosis and schwannomatosis [1].

The incidence of intravascular schwannomas is unknown. The first published case of a schwannoma in a vein lumen was reported in 2011 by Gaudi et al. [5,9].

Venous obstruction is most commonly seen in the form of deep venous thrombosis [8,13]. To the best of our knowledge, a complete obstruction of a deep vein by an intravascular schwannoma has not been previously reported. This is the third reported case of an intravascular schwannoma located in the posterior calf and the first case of a schwannoma in a deep vein of the left leg. Our case showed some clinical similarities with the cases previously reported by other authors, such as the presence of localized pain, a long evolution period (3 years in our case), and recent size enlargement [9-12]. However, unlike previously reported cases in which the age range was 44–56 years and the tumor size range was 0.3–1.5 cm, our patient was older, 68 years, and the tumor was larger, 2.3 cm.

Various theories have been proposed to explain intravascular schwannoma onset. Some of these theories include the nerve origin being native to the vessel wall, tumor embolization, or direct tumor growth extension [9-11]. In some cases, the schwannomas show vascular alterations that display reactive vessel proliferation and tumor vessel permeability that allow for the schwannoma extension to vascular territories [14]. We theorize a nervi vasorum origin due to the proximity of the intravascular tumor to the nervi vasorum nerves (Fig. 4) seen in our case (Fig. 2A–D). Nervi vasorum, or "vessel nerves," are small nerves organized as a network and located in the outer and middle layers of the blood vessels [15,16]. Nervi vasorum play an important role in the maintenance of an appropriate tonus of vascular smooth muscle cells and regulate local blood pressure in doing so [17]. This vascular nerve system participates in the regulation of vasoconstriction and vasodilation and is generally composed of sympathetic fibers. Some of these trigger vasodilation and others induce vasoconstriction depending on the nature of the neurotransmitter and receptors located on the target cell, while parasympathetic stimulation triggers vasodilation.

The correct interpretation of histopathologic features by the pathologist is key to distinguish schwannomas from other tumors on the differential diagnosis list that includes neurofibroma, intravascular leiomyoma/leiomyosarcoma, intravascular lobular capillary hemangioma, intravascular fasciitis, and malignant pe-

https://doi.org/10.4132/jptm.2024.05.15

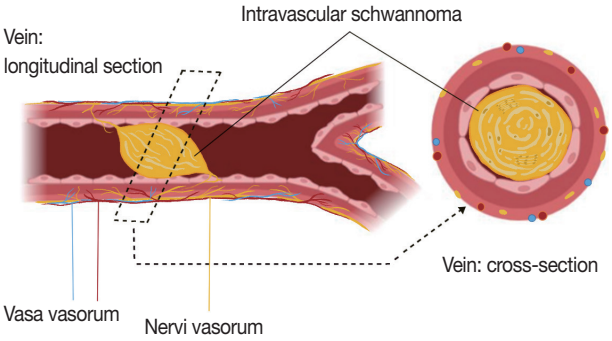

Fig. 4. Anatomical illustration image to explain the hypothetical nervi vasorum origin of intravascular schwannoma and to demonstrate the different biological structures involved. A longitudinal section view of a vessel with a schwannoma of intravascular growth and its hypothesized relation with the peripheral nerve sheath elements of the nervi vasorum network (left). Cross-section view of a blood vessel with a complete lumen obstruction by an intravascular schwannoma (right). Created in BioRender and Clip Studio Paint.

ripheral nerve sheath tumor.

The treatment of choice for schwannomas is surgery in the vast majority of symptomatic cases when the integrity of near organs is not compromised; but, in some cases, the surgical option depends on the tumor location [18,19]. There are no widely accepted treatment guidelines for this tumor. In all previously reported cases, surgical removal in these benign cases, as with conventional cases of schwannomas in other locations, has been the treatment of choice.

The patient is symptom-free after 12 months of follow-up from the surgery and continues to be monitored.

Recognizing the histopathologic features of this rare entity in an intravascular location is important to prevent misdiagnosis [11].

More studies with a large prospective series and molecular studies are required to elucidate the mechanisms underlying the development and the clinical and biological behavior of intravascular schwannomas.

Ethics Statement

Informed written consent was obtained from the patient. This case report was approved by the ethics committee of the University Hospital of Salamanca (2023 02 387).

Availability of Data and Material

The datasets generated or analyzed during the study are available from the corresponding author on reasonable request.

Code Availability

Not applicable.

ORCID

Luis Miguel Chinchilla-Tábora https://orcid.org/0000-0002-7435-3509
Beatriz Segovia Blázquez https://orcid.org/0009-0008-2286-0059
José María Sayagués https://orcid.org/0000-0003-0582-3500
Marta Rodríguez González https://orcid.org/0000-0001-8544-6201
Joaquín González-Rivero https://orcid.org/0009-0006-1543-011X
José Antonio Muñoz León https://orcid.org/0000-0001-9732-5044
Andrea Beatriz Jiménez Pérez https://orcid.org/0009-0009-3736-547X
Idalia González Morais https://orcid.org/0000-0002-4372-4725
Diego Bueno-Sacristán https://orcid.org/0000-0003-4785-5711
María Dolores Ludeña de la Cruz https://orcid.org/0000-0003-3991-5956

Author Contributions

Conceptualization: LMCT, BSB. Funding acquisition: MDLC, JMS. Investigation: LMCT, BSB. Resources: LMCT, BSB, JMS, MRG, JAML, ABJP, IGM, DBS, MDL. Writing—original draft: LMCT. Writing—review & editing: BSB, LMCT, JGR, ABJP, DBS, IGM, MRG, JAML, JMS, MDLC. Approval of final manuscript: all authors.

Conflicts of Interest

The authors declare that they have no potential conflicts of interest.

Funding Statement

No funding to declare.

References

1. Perry A. Schwannoma. In: WHO Classification of Tumours Editorial Board, ed. WHO classification of tumours: soft tissue and bone tumours. 5th ed. Lyon: IARC Press, 2020; 226-31.
2. Evans DG. Neurofibromatosis type 2 (NF2): a clinical and molecular review. Orphanet J Rare Dis 2009; 4: 16.
3. Casadei GP, Komori T, Scheithauer BW, Miller GM, Parisi JE, Kelly PJ. Intracranial parenchymal schwannoma: a clinicopathological and neuroimaging study of nine cases. J Neurosurg 1993; 79: 217-22.
4. Voltaggio L, Murray R, Lasota J, Miettinen M. Gastric schwannoma: a clinicopathologic study of 51 cases and critical review of the literature. Hum Pathol 2012; 43: 650-9.
5. Belakhoua SM, Rodriguez FJ. Diagnostic pathology of tumors of peripheral nerve. Neurosurgery 2021; 88: 443-56.
6. Guedes-Correa JF, Cardoso RS. Immunohistochemical markers for schwannomas, neurofibromas and malignant peripheral nerve sheath tumors: what can the recent literature tell us? Arq Bras Neurocir 2018; 37: 105-12.
7. Magro G, Broggi G, Angelico G, et al. Practical approach to histological diagnosis of peripheral nerve sheath tumors: an update. Diagnostics (Basel) 2022; 12: 1463.
8. Packer CF, Bickel S, Dattilo JB. Vein obstruction [Internet]. Treasure Island: StatPearls Publishing, 2023 [cited 2023 Dec 12]. Available from: http://www.ncbi.nlm.nih.gov/books/NBK537255/.
9. Gaudi S, Mills O, Goyette EF, Morgan MB. Intravascular schwannoma. Am J Dermatopathol 2011; 33: 850-4.
10. Park J, Lee D. Intraarterial schwannoma in horizontal segment of middle cerebral artery causing subarachnoid hemorrhage. J Neurosurg 2013; 118: 1069-71.
11. Ward RE, Shah JA, Mehregan DR, Ali L. A rare case of intravascular schwannoma. J Cutan Pathol 2018; 45: 731-3.
12. Dai A, Cai JP. Intravascular schwannoma: a review of a rare diag-

nosis. J Cutan Pathol 2021; 48: 314-7.
13. Stubbs MJ, Mouyis M, Thomas M. Deep vein thrombosis. BMJ 2018; 360: k351.
14. Papiez J, Rojiani MV, Rojiani AM. Vascular alterations in schwannoma. Int J Clin Exp Pathol 2014; 7: 4032-8.
15. Fernandez-Flores A, Saeb-Lima M, Cassarino DS. Intramural schwannoma involving a vein. J Cutan Pathol 2019; 46: 211-5.
16. Taylor AM, Bordoni B. Histology, blood vascular system [Internet]. Treasure Island: StatPearls Publishing, 2023 [cited 2024 Jan 22]. Available from: http://www.ncbi.nlm.nih.gov/books/NBK553217/.
17. Cabrera-Fischer EI, Bia D, Zocalo Y, Wray S, Armentano R. The adventitia layer modulates the arterial wall elastic response to intra-aortic counterpulsation: in vivo studies. Artif Organs 2013; 37: 1041-8.
18. Halliday J, Rutherford SA, McCabe MG, Evans DG. An update on the diagnosis and treatment of vestibular schwannoma. Expert Rev Neurother 2018; 18: 29-39.
19. Neurilemmoma (schwannoma) treatment and management [Internet]. Newark: Medscape, 2022 [cited 2023 Dec 15]; Available from: https://emedicine.medscape.com/article/1256405-treatment?form=fpf.

 https://doi.org/10.4132/jptm.2024.05.15

JPTM
Journal of Pathology and Translational Medicine 2024; 58: 255-260
https://doi.org/10.4132/jptm.2024.08.15

CASE STUDY

Rhabdomyosarcoma of the skull with *EWSR1* fusion and ALK and cytokeratin expression: a case report

Hyeong Rok An[1], Kyung-Ja Cho[1], Sang Woo Song[2], Ji Eun Park[3], Joon Seon Song[1]

Departments of [1]Pathology and [2]Neurosurgery, [3]Department of Radiology and Research Institute of Radiology, Asan Medical Center, University of Ulsan College of Medicine, Seoul, Korea

Rhabdomyosarcoma (RMS) comprises of heterogeneous group of neoplasms that occasionally express epithelial markers on immunohistochemistry (IHC). We herein report the case of a patient who developed RMS of the skull with *EWSR1* fusion and anaplastic lymphoma kinase (ALK) and cytokeratin expression as cytomorphologic features. A 40-year-old man presented with a mass in his forehead. Surgical resection was performed, during which intraoperative frozen specimens were obtained. Squash cytology showed scattered or clustered spindle and epithelioid cells. IHC revealed that the resected tumor cells were positive for desmin, MyoD1, cytokeratin AE1/AE3, and ALK. Although *EWSR1* rearrangement was identified on fluorescence in situ hybridization, *ALK*, and *TFCP2* rearrangement were not noted. Despite providing adjuvant chemoradiation therapy, the patient died of tumor progression 10 months after diagnosis. We emphasize that a subset of RMS can express cytokeratin and show characteristic histomorphology, implying the need for specific molecular examination.

Key Words: Rhabdomyosarcoma; Skull; *EWSR1* protein; Keratins; Cytology

Received: December 10, 2023 **Revised:** July 11, 2024 **Accepted:** August 14, 2024

Corresponding Author: Joon Seon Song, MD, PhD, Department of Pathology, Asan Medical Center, University of Ulsan College of Medicine, 88 Olympic-ro 43-gil, Songpa-gu, Seoul 05505, Korea
Tel: +82-2-3010-4548, Fax: +82-2-472-7898, E-mail: songjs@amc.seoul.kr

Rhabdomyosarcoma (RMS) is a heterogeneous group of malignant neoplasms that share common embryonic skeletal muscle features. It is one of the most common pediatric sarcomas and rarely presents in adults. Adults diagnosed with RMS have a poorer prognosis than do pediatric patients, with 5-year survival rates of 27% compared with 61%, respectively [1]. Currently, RMS is classified into embryonal, alveolar, pleomorphic, and spindle cell/sclerosing types and subdivided through molecular studies. For example, spindle cell/sclerosing RMS has a subset of genetic groups that include *MYOD1* mutation [2], *NCOA2* fusions [3], and *VGLL2* rearrangement [4].

Considering that all RMSs exhibit skeletal muscle differentiation, the diagnosis of this neoplasm has been primarily based on confirmation of the immunophenotype. Interestingly, RMSs occasionally exhibit aberrant cytokeratin expression [5]. Some of these multi-phenotypic RMSs have characteristic clinical, histologic, and molecular properties [6]. For example, one study recently described RMS with *EWSR1/FUS-TFCP2* fusion as a distinct entity of epithelioid and spindle cell RMS, characterized by a predilection for the craniofacial bone and the expression of cytokeratin AE1/AE3 and anaplastic lymphoma kinase (ALK) on immunohistochemistry (IHC) [7].

We herein report a case of RMS arising in the skull with *EWSR1* fusion and ALK and cytokeratin expression with squash smear cytology and surgical specimens.

CASE REPORT

A 40-year-old previously healthy man presented with a palpable, hard, unmovable mass in his right forehead that appeared 3 months prior. Magnetic resonance imaging detected a 2.7-cm-sized dumbbell-shaped enhancing mass in the right frontal bone involving the scalp and meninges (Fig. 1A). The mass was suspected to be a malignant bone tumor, such as Langerhans cell histiocytosis or metastasis.

Surgical resection was performed without biopsy, and sam-

pISSN 2383-7837
eISSN 2383-7845

ples from the scalp were obtained for intraoperative frozen section diagnosis. Squash cytology revealed small to large loosely cohesive clusters with smear artifact (Fig. 2A). The background was clear with few-to-no inflammatory cells and no necrosis. The clusters consisted of mixed epithelioid and spindle cells showing round-to-oval nuclei, prominent nucleoli, and granular chromatin with eosinophilic cytoplasm (Fig. 2B). Marked nuclear pleomorphism and scant mitotic activity were observed (Fig. 2C). Frozen section diagnosis confirmed positivity for malignancy.

During gross examination, we observed an ill-demarcated, homogenous, whitish, solid, hard mass in the skull measuring 2.5×2.2×1.1 cm and penetrating through the dura mater (Fig. 1B). The resected tumor consisted of spindle and epithelioid cells with primarily a fascicular or whirling arrangement and few portions of solid growth (Fig. 2D, E). The neoplastic cells had round, vesicular nuclei, prominent one or two macronucleoli and moderate-to-abundant eosinophilic cytoplasm. Brisk mitosis and necrosis were noted.

The tumor cells were diffusely positive for desmin (clone D33, 1:200, Dako, Santa Clara, CA, USA), MyoD1 (EP212, 1:50, Cell Marque, Rocklin, CA, USA), and cytokeratin AE1/AE3 (1:400, Novocastra, San Jose, CA, USA) and focally positive for ALK (5A4, 1:200, Novocastra), smooth muscle actin (M0851, 1:500, Dako), myogenin (F5D, 1:100, Cell Marque), epithelial membrane antigen (EMA; E29, 1:100, Dako), p53 (DO-7, 1:1,000, Dako), S100 (4C4.9, 1:400, Cell Marque), nestin (10C2, 1:1,000, Cell Marque), SATB2 (polyclonal, 1:200, Cell Marque) on IHC (Fig. 2F–I). Conversely, the tumor cells tested negative for myoglobin (Z001, 1:1,000, Thermo Fisher Scientific, Waltham, MA, USA), signal transducer and activator of transcription 6 (polyclonal, 1:1,000, Abcam, Cambridge, UK), cyclin-dependent kinase 4 (DCS-31, 1:100, Santa Cruz Biotechnology, Santa Cruz, CA, USA), MDM-2 (SPM14, 1:50, Zeta, Sierra Madre, CA, USA), CD34 (1:400, Cell Marque), ERG (EP111, 1:400, Cell Marque), and HMB45 (1:50, Dako). *EWSR1*, *ALK*, and *TFCP2* break-apart fluorescence in situ hybridization (FISH) revealed *EWSR1* rearrangement (Fig. 3A) but no *ALK* or *TFCP2* rearrangement (Fig. 3B, C). A molecular study using next-generation sequencing was attempted, but DNA quality was too degraded by decalcification.

Although our patient received one cycle of adjuvant chemotherapy (vincristine, doxorubicin, and cyclophosphamide according to the IRS-III protocol), the size of the suspicious mass continued to increase for 2 months. No gross tumor remained at the time of surgery. Intensity-modulated radiation therapy (4680 cGY/26fx), three cycles of second-line chemotherapy (ifosfamide, carboplatin, and etoposide), and one cycle of third-line chemotherapy (gemcitabine and doxorubicin) were provided consecutively for residual/recurrent tumor. Unfortunately, the patient's condition deteriorated with multiple metastases to the dura mater, skin, lung, rib, and abdominal cavity. The patient eventually died of tumor progression 10 months after diagnosis.

DISCUSSION

RMSs occurring in the head and neck, including the parame-

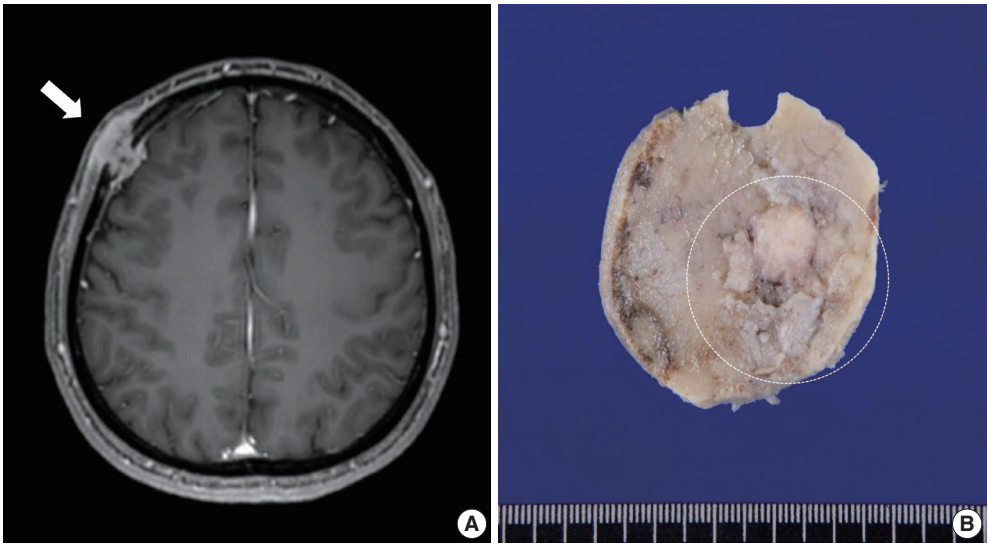

Fig. 1. Radiologic and gross findings. (A) Ga-enhanced T1-weighted magnetic resonance imaging shows a transdiploic mass in the frontal scalp involving the dura mater (arrow). (B) Grossly, an ill-circumscribed, whitish solid mass infiltrates the skull (circle).

https://doi.org/10.4132/jptm.2024.08.15

ningeal or orbital area, account for one-third of all cases of RMS in children and adolescents. Among adults, RMSs are most frequently observed in the extremities, followed by the chest/abdominal/pelvic, genitourinary, and head or neck regions [1]. However, RMSs of the skull are quite uncommon, with most cases originating from the skull base or temporal bone [8]. Primary tumors detected in the vault of the skull should be preferentially considered osteoma, osteosarcoma, Ewing sarcoma, Langerhans cell histiocytosis, plasmacytoma, or chondrosarcoma [9]. Moreover, for transdiploic lesions in the skull vault, radio-

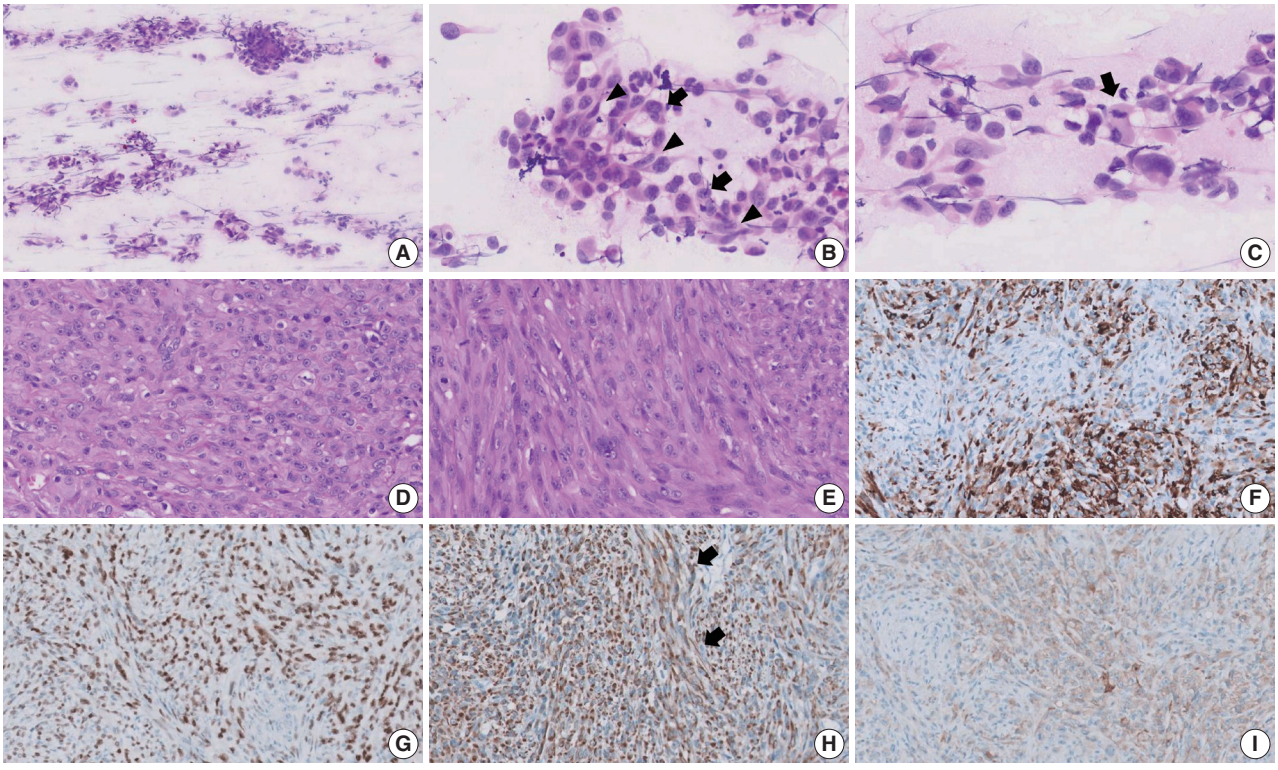

Fig. 2. Representative images of squash cytology, histologic, and immunohistochemical findings. (A) On frozen section, tumor clusters with smear artifacts are scattered in a clear background. (B) Epithelioid cells with abundant cytoplasm and prominent nucleoli are identified. A few spindle-shaped cells (arrowheads) and binucleation (arrows) are noted. (C) Marked nuclear pleomorphism and mitosis (arrow) are observed. (D) In permanent section, the epithelioid cell component shows glassy cytoplasm with a solid pattern. (E) Spindle cell component shows a fascicular pattern. Tumor cells express immuno-positivity for desmin (F), MyoD1 (G), cytokeratin AE1/AE3 (H), and anaplastic lymphoma kinase (I). Cytokeratin is expressed in not only epithelioid cells but also spindle cells (arrows, H).

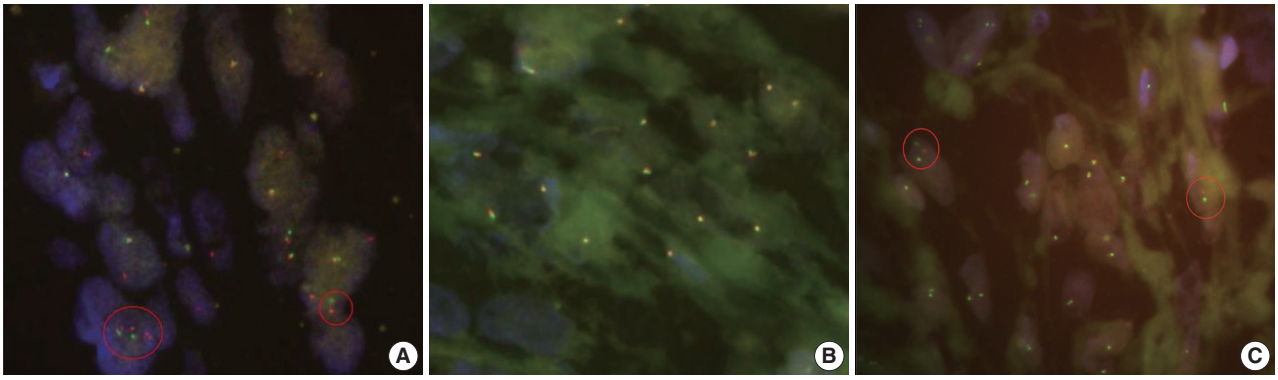

Fig. 3. Results of break-apart fluorescence in situ hybridization. (A) *EWSR1* rearrangement is identified (circles). (B) Anaplastic lymphoma kinase copy number change or translocation is not observed. (C) TFCP2 break-apart signals are detected in a few tumor cells (circles). Seven of 100 cells present a splitting signal on counts, indicating a negative result.

logic differential diagnoses include meningioma, solitary fibrous tumor, lymphoma, plasmacytoma, and metastasis [10]. As the present case was initially suspected to be Langerhans cell histiocytosis or metastasis, establishing a correct diagnosis of RMS of the skull vault was challenging given its rarity in this location.

The *EWSR1* gene, which stands for Ewing sarcoma breakpoint region 1, is ubiquitously involved in various cellular processes, and its rearrangements with diverse partner genes have been associated with the development of multiple types of tumors [11]. For example, *ESWR1* rearrangements have been frequently detected and serve as a key diagnostic finding in certain soft tissue tumors, such as Ewing sarcoma, round cell sarcomas with *EWSR1–non-ETS* fusions, desmoplastic small round cell tumor, myxoid liposarcoma, tumors with *EWSR1/FUS* fused to the *CREB*-family, sclerosing epithelioid fibrosarcoma, extraskeletal myxoid chondrosarcoma, and RMS with *EWSR1/FUS-TFCP2* fusion. Considering the presence of *EWSR1* fusion in various sarcomas, *EWSR1*-rearranged tumors necessitate further examination for the detection of the partner gene, especially in cases showing unusual clinicopathologic features. Despite having identified *EWSR1* break-apart on FISH, we failed to confirm the counterpart gene to which the *EWSR1* gene fused.

The findings of the present report raise questions about a series of differential diagnoses, due to the present case's unique and complex characteristics. *EWSR1-PATZ1* and *EWSR1-NFATC2* sarcomas are classified as round cell sarcomas with *EWSR1–non-ETS* fusions according to World Health Organization tumor classification and can show diverse histopathologic and immunophenotypic features [12]. *EWSR1-PATZ1* sarcomas usually originate from the deep soft tissue of the chest wall and abdomen; however, they can develop in the head and neck as previously reported [13]. They express myogenic and neurogenic markers (S100P, SOX10, and GFAP) but rarely exhibit epithelial markers. Furthermore, ALK overexpression has not yet been reported in this tumor. Although *EWSR1-NFATC2* sarcomas can show mixed epithelioid and spindle cell histology and dot-like positivity for cytokeratin, they are usually accompanied by abundant myxohyalinized stroma and do not express skeletal muscle differentiation [14]. A subset of tumors with *EWSR1/FUS* fused to the *CREB*-family has shown a predilection for intracranial location and exhibited both EMA and desmin [15]. These tumors consisted of ovoid or round cells in a myxoid background. Other *EWSR1-CREB* fusion neoplasms demonstrated a hybrid epithelioid and spindle morphology with cytokeratin and desmin positivity, and one expressed diffuse ALK positivity [16]. However, they commonly arise in mesothelial-lined cavities.

RMSs with *EWSR1/FUS-TFCP2* fusion are a newly emerging sub-classification characterized by a predilection for craniofacial bone, specific immunoprofiles, and molecular alterations [7,17]. This tumor comprises hybrid epithelioid and spindle cells. The latter are arranged in fascicular growth and have nuclei that are ovoid and fusiform with prominent nucleoli and mild pleomorphism, whereas the former contain an abundance of eosinophilic, often glassy cytoplasm arranged in solid sheets [18,19]. Several cases contain a portion of small round or rhabdoid cytologic features. Almost all cases have high mitotic rates and tumor necrosis. The tumor displayed positivity for myogenic markers, such as MyoD1, myogenin, and desmin. Interestingly, tumors in most cases show positivity for cytokeratin AE1/AE3 and ALK on IHC, and molecular studies often reveal ALK overexpression. One study showed that *EWSR1/FUS-TFCP2* can activate *ALK* upregulation [20]. However, *ALK* rearrangement has not been reported previously [18]. Although we could not directly confirm *TFCP2* rearrangement or fusion, we suspected that the tumor in the present case might have been RMS with *EWSR1-TFCP2* fusion based on the tumor's location in the craniofacial bone, the presence of mixed epithelioid and spindle cells, and the tumor's immunopositivity for myogenic markers, cytokeratin, ALK, and *EWSR1* rearrangement. According to a report on spindle cell RMS, aberrant keratin expression was a unique feature of RMS with *EWSR1-TFCP2* fusion, which differed from spindle cell RMS harboring other fusions [6]. Additionally, a literature review revealed that *EWSR1* rearrangement in RMS is exceedingly rare, and most of these cases involve RMS with *EWSR1-TFCP2* fusion. However, some round cell sarcomas with *EWSR1* fusion express skeletal muscle markers, which necessities differential diagnosis [21]. Meanwhile, we interpreted the results of *TFCP2* FISH in our case as negative despite the identification of a few break-apart signals. Although Bin Xu et al. counted 200 nuclei and considered split signal of over 20% to be positive [18], currently no definite criteria for interpreting *TFCP2* FISH results have been established.

The prognosis of RMS with *EWSR1/FUS-TFCP2* is incredibly poor, with a median survival time of less than 21 months (Table 1) [6,7,18,19]. Over half of patients develop local recurrence, regional lymph node metastasis, or distant metastasis to the bones and lungs [18]. Treatment options involve surgical resection, chemotherapy, and radiotherapy, all of which have limited efficacy. Although *ALK* inhibitors have been proposed to be a potential target therapy, their effectiveness remains unclear [20,22,23].

https://doi.org/10.4132/jptm.2024.08.15

Table 1. Summary of major published cases of rhabdomyosarcoma with *TFCP2* fusion

Study	No. of cases	Age (yr)	Sex (M:F)	Locations	Outcomes
Le Loarer et al. (2020) [7]	14	11–86 (mean, 31)	3:4	Craniofacial (8/14), other bone (4/14), soft tissue (2/12)	Median survival: 8 months
Chrisinger et al. (2020) [19]	23[a]	11–86	1:2.7	Craniofacial (12/23), other bone (9/23), soft tissue (2/23)	Median survival: 15 months
Xu et al. (2021) [18]	27[a]	11–74 (mean, 25)	1.25:1	Craniofacial (18/27), other bone (8/27), soft tissue (1/27)	1- and 2-year disease-specific survival rate: 74% and 35%, respectively
Dehner et al. (2023) [6]	56[a]	8–86 (mean, 34)	5:9	Craniofacial (37/56), other bone (13/56), soft tissue (6/56)	Median survival: 21 months

[a]This number includes data from previously reported cases through a literature review.

In summary, we report an unusual case of RMS of the skull with *EWSR1* fusion and ALK and cytokeratin expression, highlighting the importance of precise histopathologic examination along with comprehensive immunohistochemical and molecular evaluation for diagnosis and management.

Ethics Statement

This study was approved by the Institutional Review Board, and the need for informed consent was waived (Asan Medical Center IRB No. 2023-1548).

Availability of Data and Material

The datasets generated or analyzed during the study are available from the corresponding author on reasonable request.

Code Availability

Not applicable.

ORCID

Hyeong Rok An https://orcid.org/0009-0000-7145-2619
Kyung-Ja Cho https://orcid.org/0000-0002-4911-7774
Sang Woo Song https://orcid.org/0000-0002-5523-3798
Ji Eun Park https://orcid.org/0000-0002-4419-4682
Joon Seon Song https://orcid.org/0000-0002-7429-4254

Author Contributions

Conceptualization: JSS. Data curation: HRA. Investigation: HRA, JSS. Resources: SWS, JEP, JSS. Supervision: JSS, KJC. Visualization: HRA, JSS. Writing—original draft preparation: HRA. Writing—review & editing: KJC, SWS, JEP, JSS. Approval of final manuscript: all authors.

Conflicts of Interest

J.S.S., a contributing editor of the *Journal of Pathology and Translational Medicine*, was not involved in the editorial evaluation or decision to publish this article. All remaining authors have declared no conflicts of interest.

Funding Statement

No funding to declare.

References

1. Sultan I, Qaddoumi I, Yaser S, Rodriguez-Galindo C, Ferrari A. Comparing adult and pediatric rhabdomyosarcoma in the surveillance, epidemiology and end results program, 1973 to 2005: an analysis of 2,600 patients. J Clin Oncol 2009; 27: 3391-7.
2. Agaram NP, LaQuaglia MP, Alaggio R, et al. *MYOD1*-mutant spindle cell and sclerosing rhabdomyosarcoma: an aggressive subtype irrespective of age. A reappraisal for molecular classification and risk stratification. Mod Pathol 2019; 32: 27-36.
3. Mosquera JM, Sboner A, Zhang L, et al. Recurrent *NCOA2* gene rearrangements in congenital/infantile spindle cell rhabdomyosarcoma. Genes Chromosomes Cancer 2013; 52: 538-50.
4. Alaggio R, Zhang L, Sung YS, et al. A molecular study of pediatric spindle and sclerosing rhabdomyosarcoma: identification of novel and recurrent VGLL2-related fusions in infantile cases. Am J Surg Pathol 2016; 40: 224-35.
5. Bahrami A, Gown AM, Baird GS, Hicks MJ, Folpe AL. Aberrant expression of epithelial and neuroendocrine markers in alveolar rhabdomyosarcoma: a potentially serious diagnostic pitfall. Mod Pathol 2008; 21: 795-806.
6. Dehner CA, Broski SM, Meis JM, et al. Fusion-driven spindle cell rhabdomyosarcomas of bone and soft tissue: a clinicopathologic and molecular genetic study of 25 cases. Mod Pathol 2023; 36: 100271.
7. Le Loarer F, Cleven AH, Bouvier C, et al. A subset of epithelioid and spindle cell rhabdomyosarcomas is associated with *TFCP2* fusions and common ALK upregulation. Mod Pathol 2020; 33: 404-19.
8. Radzikowska J, Kukwa W, Kukwa A, Czarnecka A, Krzeski A. Rhabdomyosarcoma of the head and neck in children. Contemp Oncol (Pozn) 2015; 19: 98-107.
9. Kakkar A, Nambirajan A, Suri V, et al. Primary bone tumors of the skull: spectrum of 125 cases, with review of literature. J Neurol Surg B Skull Base 2016; 77: 319-25.
10. Pons Escoda A, Naval Baudin P, Mora P, et al. Imaging of skull vault tumors in adults. Insights Imaging 2020; 11: 23.
11. Flucke U, van Noesel MM, Siozopoulou V, et al. *EWSR1*: the most common rearranged gene in soft tissue lesions, which also occurs in different bone lesions: an updated review. Diagnostics (Basel) 2021; 11: 1093.
12. WHO Classification of Tumours Editorial Board. WHO classification of tumours series, 5th ed. Vol. 3. Soft tissue and bone tumours. Lyon: International Agency for Research on Cancer, 2020.
13. Bridge JA, Sumegi J, Druta M, et al. Clinical, pathological, and genomic features of *EWSR1-PATZ1* fusion sarcoma. Mod Pathol 2019; 32: 1593-604.
14. Wang GY, Thomas DG, Davis JL, et al. *EWSR1-NFATC2* translocation-associated sarcoma clinicopathologic findings in a rare aggressive primary bone or soft tissue tumor. Am J Surg Pathol 2019; 43: 1112-22.
15. Kao YC, Sung YS, Zhang L, et al. *EWSR1* fusions with CREB family

transcription factors define a novel myxoid mesenchymal tumor with predilection for intracranial location. Am J Surg Pathol 2017; 41: 482-90.
16. Argani P, Harvey I, Nielsen GP, et al. *EWSR1/FUS-CREB* fusions define a distinctive malignant epithelioid neoplasm with predilection for mesothelial-lined cavities. Mod Pathol 2020; 33: 2233-43.
17. Watson S, Perrin V, Guillemot D, et al. Transcriptomic definition of molecular subgroups of small round cell sarcomas. J Pathol 2018; 245: 29-40.
18. Xu B, Suurmeijer AJ, Agaram NP, Zhang L, Antonescu CR. Head and neck rhabdomyosarcoma with *TFCP2* fusions and ALK overexpression: a clinicopathological and molecular analysis of 11 cases. Histopathology 2021; 79: 347-57.
19. Chrisinger JSA, Wehrli B, Dickson BC, et al. Epithelioid and spindle cell rhabdomyosarcoma with *FUS-TFCP2* or *EWSR1-TFCP2* fusion: report of two cases. Virchows Arch 2020; 477: 725-32.
20. Schopf J, Uhrig S, Heilig CE, et al. Multi-omic and functional analysis for classification and treatment of sarcomas with *FUS-TFCP2* or *EWSR1-TFCP2* fusions. Nat Commun 2024; 15: 51.
21. Michal M, Rubin BP, Agaimy A, et al. *EWSR1-PATZ1*-rearranged sarcoma: a report of nine cases of spindle and round cell neoplasms with predilection for thoracoabdominal soft tissues and frequent expression of neural and skeletal muscle markers. Mod Pathol 2021; 34: 770-85.
22. Brunac AC, Laprie A, Castex MP, et al. The combination of radiotherapy and ALK inhibitors is effective in the treatment of intraosseous rhabdomyosarcoma with *FUS-TFCP2* fusion transcript. Pediatr Blood Cancer 2020; 67: e28185.
23. Valerio E, Furtado Costa JL, Perez Fraile NM, et al. Intraosseous spindle cell/epithelioid rhabdomyosarcoma with *TFCP2* rearrangement: a recent recognized subtype with partial response to alectinib. Int J Surg Pathol 2023; 31: 861-5.

https://doi.org/10.4132/jptm.2024.08.15